Universitatea *Transilvania* din Braşov

HABILITATION THESIS

Computational Methods for Personalized Cardiovascular Medicine

Domain: Systems Engineering

Author: Lecturer Dr. Eng. Lucian Mihai ITU

Transilvania University of Braşov

BRAŞOV, 2017

Acknowledgments

First of all, I would like to thank conf. dr. ing. Constantin SUCIU not only for the continuous support that he has offered me throughout the years, but especially for giving me the opportunity to embark in 2010 on the scientific journey that has lead to this work.

I would like to also thank dr. ing. Puneet SHARMA, dr. ing. Dorin COMANICIU and the entire team at the Medical Imaging Technologies department in Princeton, New Jersey, USA for the scientific support and collaboration we have had during the past 7 years, inlcuding the three research internships carried out in 2011 and 2012.

Furthermore, I would like to thank prof. dr. ing. Florin MOLDOVEANU, the supervisor of my PhD studies, for the fruitful collaboration we have had during the years, and especially during the time of the PhD research activities, which have lead to numerous results published in co-authorship. I am extremely grateful for the scientific support, as well as for the passion and patience which he has brought forward during all research activities.

A thought of gratitude for the whole Imaging and Computer Vision team at Siemens Corporate Technology, Brasov, Romania, in its wholeness, a kind-spirited team, patient and open, ready to help whenever needed.

Thanks to all the commission members for the honor that you brought upon me by accepting to offer support in my initiative. I would also like to give my special thanks to the students that motivated and inspired me in the last several years.

Last but not least I would like to thank my family for the unconceivable support that they have offered me over the years. Please let me dedicate to you this thesis!

Contents

List of Abbreviations

ABI	Ankle-Brachial Index
ACM	Area Compliance Method
AI	Artificial Intelligence
BC	Brachiocephalic artery
BSR	Baseline Stenosis Resistance
CAD	Coronary Artery Disease
CCTA	Coronary Computed Tomography Angiography
CFD	Computational Fluid Dynamics
CFL	Courant Friedrich Law
CFR	Coronary Flow Reserve
CoA	Aortic Coarctation
CPU	Central Processing Unit
CT	Computer Tomography
CUDA	Compute Univied Device Architecture
CVD	Cardiovascular Disease
DAo	Descending Aorta
DBP	Diastolic Blood Pressure
DL	Deep Learning
EDV	End-Diasolic Volume
EF	Ejection Fraction
EPP	Effective Perivascular Pressure
ESV	End-Systolic Volume
FFR	Fractional Flow Reserve
FMG	Full Multigrid

FSI	Fluid Structure Interaction
GMG	Geometric Multigrid Method
GPU	Graphics Processing Unit
HR	Heart Rate
HSR	Hyperemic Stenosis Resistance
IFR	Instantaneous Wave Free Ratio
IVUS	Intravascular Ultrasound
LA	Left atrium
LAD	Left Anterior Descending artery
LCA	Left Coronary Artery
LCC	Left Common Carotid artery
LCx	Left Circumflex artery
LV	Left Ventricle
MAP	Mean Arterial Pressure
ML	Machine Learning
MRA	Magnetic Resonance Angiography
MRI	Magnetic Resonance Imaging
OCT	Optical Coherence Tomography
PAD	Peripheral Arterial Disease
PCG	Preconditioned Conjugate Gradient
PCI	Percutaneous Coronary Intervention
PC-MRI	Phase Contrast Magnetic Resonance Imaging
PDE	Partial Differential Equation
PPM	Pulse Pressure Method
PV	Pressure volume
PWV	Pulse Wave Velocity
RAS	Renal Artery Stenosis
RBGS	Red Black Gauss Seidel
RCA	Right Coronary Artery
rFFR	Renal Fractional Flow Reserve
SBP	Systolic Blood Pressure
SIMD	Single Instruction Multiple Data
SIMT	Single Instruction Multiple Thread
SPMD	Single Program Multiple Data
US	Ultrasound
XA	X-ray Angiography
Z	Characteristic impedance

Part I

Rezumat

Obiectivul medicinii personalizate este personalizarea strategiei de tratare a pacienților pe baza unor caracteristici, condiții, necesități sau particularități individuale de-a lungul tuturor etapelor relevante pentru pacienți, începând de la prevenție și diagnoză până la tratament și monitorizare ulterioară. Bolile cardiovasculare reprezintă principala cauză de deces la nivel mondial și această lucrare se concentrează asupra medicinii cardiovasculare personalizate, și în mod special asupra metodelor computaționale care includ următoarele arii de interes: modelare multiscalară personalizată a hemodinamicii arteriale, inteligență artificială și procesare paralelă în modelarea hemodinamică multiscalară. Toate cele trei arii sunt esențiale pentru a atinge obiectivul final al aplicării modelelor în rutine clinice pentru evaluarea non-invazivă și personalizată a patologiilor cardiovasculare.

Inițial se introduce un framework ierarhic de estimare a parametrilor pentru realizarea unor simulări hemodinamice personalizate în modele arteriale, care folosesc arbori structurați ca și condiții de frontieră. Se formulează o problemă de calibrare la fiecare nivel al framework-ului ierarhic, care caută soluția de punct fix a unui sistem de ecuații neliniare. Proprietăți hemodinamice precum rezistența și complianța sunt estimate la primul nivel pentru a îndeplini o serie de obiective formulate pe baza unor măsurători clinice de presiune și/sau debit. La al doilea nivel se estimează parametri arborilor structurați astfel încât să se obțină valorile proprietăților hemodinamice determinate la primul nivel. O caracteristică cheie a metodei propuse este faptul că, pentru a asigura o gamă largă de variație a valorilor acestor proprietăți, se personalizează doi parametrii diferiți ai arborilor structurați pentru fiecare proprietate hemodinamică.

În continuare se introduce un framework de estimare a parametrilor pentru personalizarea automată și robustă a hemodinamicii aortice pornind de la date de rezonanță magnetică 4D. Framework-ul este bazat pe un model hemodinamic multiscalar de ordin redus de interacțiune fluid-solid și pe două proceduri de calibrare. Inițial, se personalizează parametrii windkessel ai condițiilor de frontieră de ieșire prin rezolvarea unui sistem de ecuații neliniare. Apoi, se personalizează proprietățile mecanice ale peretelui aortic prin formularea unei probleme de minimizare a celor mai mici pătrate. Cele două proceduri de calibrare sunt rulate secvențial și iterativ până când se obține convergență pentru ambele proceduri. Global, modelul computațional a produs rezultate apropiate de măsurătorile clinice care au fost folosite în formularea obiectivelor de personalizare.

De asemenea, se introduce o metodologie de separare a rigidității arteriale, determinate in vivo, în rigiditate a peretelui arterial și rigiditate a țesutului înconjurător. Se consideră o presiune efectivă perivasculară care introduce o constrângere radială. În continuare, pornind de la date in vivo, achiziționate la faza diastolică, se estimează ariile secțiunilor transversale la presiune arterială nulă. În final, rigiditatea peretelui arterial și a țesutului înconjurător sunt determinate pe baza unui model cu două arcuri paralele. Cu ajutorul unui model multiscalar de ordin redus, metodologia este folosită pentru studiul efectului global al țesutului înconjurător asupra hemodinamicii arteriale. Principalele influențe sunt: viteză de undă mai mare, unde inverse de presiune și debit care ajung mai repede înapoi la inimă, complianță totală mai mică, presiune de puls mai mare și arii reduse ale secțiunilor transversale.

În continuare, se introduce un model pentru estimarea non-invazivă a buclelor de presiune-volum personalizate pentru ventriculul stâng. Se folosește un model cu parametrii distribuiți al circulației, bazat pe circulația pulmonară venoasă, atriul stâng, ventriculul stâng și circulația sistemică. Un framework complet automatizat de estimare a parametrilor este prezentat pentru personalizarea modelului, care este format din două etape secvențiale: inițial, se calculează direct o serie de parametri și, în continuare, se aplică o metodă de calibrare bazată pe optimizare pentru a estima iterativ valorile celorlalți parametri ai modelului cu parametrii distribuiți.

Una din cele mai interesante metodologii prezentate în această lucrare este bazată pe un model de inteligență artificială pentru estimarea rezervei fracționare de debit (FFR) ca alternativă la abordările bazate pe modele de dinamica fluidelor. Modelul este antrenat cu ajutorul unei baze de date mari formată din anatomii coronariene sintetice, pentru care valorile de referință de FFR sunt calculate cu modelul de dinamica fluidelor. Modelul antrenat prezice FFR la fiecare locație a arborelui arterial și performanța lui a fost evaluată prin compararea predicțiilor cu valorile obținute cu ajutorul modelului bazat pe dinamica fluidelor și cu valorile de FFR măsurate invaziv pentru 87 de pacienți / 125 de leziuni. S-a obținut o corelație excelentă între predicții, neputând fi observat nici un bias în analiza Bland-Altman. În comparație cu modelul bazat pe dinamica fluidelor, timpul de execuție a fost redus de mai mult de 80 de ori, conducând la o evaluare în timp real a FFR.

Metoda multigrid geometric (GMG) reprezintă unul din cei mai eficienți algoritmi de rezolvare a sistemelor mari de ecuații liniare și poate fi paralelizată eficient. S-a realizat o analiză detaliată a unei implementări GMG bazate pe procesor grafic și rezultatele au fost comparate cu o metodă optimizată a gradienților conjugați. Testele au indicat faptul că etapa de smoothing ocupă cea mai mare parte a timpului de execuție, iar varianta GMG cu cea mai bună performanță este schema V cu o configurație de smoothing 312. Stencil-ul de discretizare are o influență majoră asupra timpului de execuție și alegerea sa reprezintă un compromis între timpul de execuție și acuratețea numerică.

Part II

Scientific and Professional Achievements

1. Introduction

Multiscale Modeling of Arterial Hemodynamics
Patient-Specific Multiscale Modeling of Arterial Hemodynamics
Machine Learning in Hemodynamic Modelling
Parallel Processing in Multiscale Hemodynamic Modeling

The concept of personalized medicine has been introduced several hundred years ago, but scientists have started to understand factors causing disease only through developments made in the 19th century in chemistry and microscopy. As science and technology have evolved healthcare decisions have started to become more patient-specific. Importantly, with the developments in medical imaging, genetics and artificial intelligence the diagnosis and treatment of pathologies have become more granular. Ongoing developments in computational biology, medical imaging and regenerative medicine are setting the stage for truly personalized decision making and treatment. Nevertheless, there is still a long way before fully understanding why various pathologies initiate and evolve, and why there are considerable differences in how patients react to certain treatment plans. This means that nowadays clinicians still chose a sub-optimal treatment plans or take sub-optimal decisions on a daily basis, sometimes even relying on trial-and-error strategies. In turn this can have negative effects ranging from patient dissatisfaction, adverse responses to drugs to a different final patient outcome. The ultimate goal of personalized medicine is to identify apriori the subjects responding well to certain treatments and distinguish them from those who will not have any benefit and instead have to support costs and endure unpleasant side effects. We often refer to personalized medicine as *the right patient with the right treatment at the right time* [Sadee et al., 2005]. Overall, the objective is to personalize the treatment strategy to individual features, conditions, needs and particularities of a subject during all stages of care, ranging from prevention, diagnosis, treatment and follow-up. Personalized medicine is sometime also referred to as *precision medicine* (National Academy of Sciences - NAS) defines it as “the use of genomic, epigenomic, exposure and other data to define

individual patterns of disease, potentially leading to better individual treatment" [***NRC, 2011]) or *targeted medicine* [***FDA, 2013]. Other generally accepted definitions are:

- "The use of new methods of molecular analysis to better manage a patient's disease or predisposition to disease."– Personalized Medicine Coalition;
- "Providing the right treatment to the right patient, at the right dose at the right time." – European Union;
- "The tailoring of medical treatment to the individual characteristics of each patient." – President's Council of Advisors on Science and Technology;
- "Health care that is informed by each person's unique clinical, genetic, and environmental information." – American Medical Association;
- "A form of medicine that uses information about a person's genes, proteins, and environment to prevent, diagnose, and treat disease." – National Cancer Institute, NIH.

Personalized medicine typically refers to two different types of medical products:

- A diagnostic device: in vitro tests (used typically in genetic analysis), in vivo tests (e.g. EKG, medical imaging);
- A therapeutic device.

Nowadays, with the rapid evolution of mobile devices, wearable sensors and the Internet, patients can be monitored more effectively and more closely than ever outside of hospitals. Thus, ambulatory treatments have become feasible, which in turn increases the life quality of patients. The success of personalized medicine depends on the introduction of precise and reliable decision making tools, which typically refers to the identification of reliable biomarkers. If the decision making tool is not accurate, the treatment decision will be suboptimal. As such, personalized medicine leads in the long term to disease prevention, and to a paradigm shift from illness to wellness – from disease to maintaining health. Finally, it will also lead to reduced costs, by reducing disease burden and by providing efficient treatment plans.

Cardiovascular disease is the leading cause of death, globally. Hence, this work focuses personalized cardiovascular medicine, and specifically on computational methods related to this topic. The vast majority of cardiovascular pathologies are related to the systemic arterial hemodynamics. Typically, the modeling of arterial hemodynamics is based on the theory of fluid mechanics. Computational Fluid Dynamics (CFD) is one of the major topic areas in the field of fluid mechanics, which employs numerical methods and algorithms for solving and analyzing applications related to fluid movements. The fundamental equations which govern fluid flow are the Navier-Stokes system of equations (conservation of mass, conservation of momentum and conservation of energy). This system of equations can be solved analytically only under specific simplified and idealized conditions. Hence, typically, the Navier-Stokes equations are solved numerically.

During the last decades several numerical methods for solving these equations have been developed: finite element method, finite volume method, finite difference method, Lattice-Boltzmann method, etc. [Wendt, 2009].

In hemodynamics applications, which simulate the flow of blood in the cardiovascular system, the Navier-Stokes equations are solved inside of a closed domain, delimited by the walls of the arteries / heart chambers, etc. The incompressibility of blood leads to a simplification of the Navier-Stokes equations, which, typically, are solved without considering the energy conservation equation (the temperature is considered to be constant).

Hemodynamic simulations generally focus on a particular segment / region of interest in the cardiovascular system, which is modeled in a three-dimensional pace given by an anatomical

model reconstructed from medical imaging data acquired through Computer Tomography (CT), Magnetic Resonance Imaging (MRI), X-ray Angiography (XA), Ultrasound (US), etc. Due to the large execution times, only limited sections of the cardiovascular system can be considered for three-dimensional simulations. Since the cardiovascular system is a closed-loop system, however, the simulations performed for particular segment, without taking into account the influence of the other cardiovascular components, leads to erroneous results, especially in terms of pressure results [Quarteroni et al., 2001].

To mitigate this aspect, multiscale models have been proposed, which combine the detailed three-dimensional modeling in the region of interest with one- or zero-dimensional modeling for the remaining components of the cardiovascular system.

A crucial role in any fluid dynamics simulation is played by the boundary conditions. In hemodynamics simulations, the inlet boundary condition is typically given by patient-specific measurements (e.g. phase contrast MRI measurements) or by lumped parameter models representing the upstream cardiovascular components (e.g. the heart). The boundary condition at the arterial walls is given by the blood viscosity (the no-slip condition) [Perktold et al., 1995]. The outlet boundary condition typically poses the largest difficulties, whereas several types of such conditions can be imposed [Vignon-Clementel et al., 2010]: constant pressure, resistance, windkessel model with varying number of parameters, structured tree, etc.

Since the numerical simulation of arterial hemodynamics requires large execution times, there is a continuous need for faster computations. Parallel processors lead to an improvement of the execution time, since the majority of fluid dynamics algorithms can be parallelized efficiently. With the technological advancements of Graphics Processing Units (GPU), which contain a very large number of cores (more than 1000), and especially with the introduction of the CUDA (Compute Univied Device Architecture) language cost-efficient parallelization can be performed [Jesperson, 2009]. Similar to other applications where execution time is crucial, hemodynamic computations can profit from the porting of computationally intensive parts of the algorithms to the GPU in three ways: solve the same problem in a shorter amount of time, solve more complex problems in the same amount of time, and obtain better solutions for problems which need to be solved in a given amount of time [Kirk et al., 2010].

1.1 MULTISCALE MODELING OF ARTERIAL HEMODYNAMICS

During the last years, the progress achieved in the field of computational fluid dynamics, together with the technological advancements in medical imaging, has enabled the quantitative analysis of blood flow [Vignon-Clementel et al., 2010].

As mentioned above, one of the main difficulties for the correct modeling of the cardiovascular system is its closed-loop nature, with significant inter-dependencies between the individual components. The local blood flow characteristics are closely correlated with global system dynamics [Vignon-Clementel et al., 2006]. The distribution of blood in various vascular segments is a property of the entire system, but it influences the dynamics of each individual segment. The study of local hemodynamics is of paramount importance since several pathologies like the thickening of the arterial wall or the development of stenoses are influenced by local hemodynamics. On the other hand, certain local changes, like those of the vascular lumen, can lead to a change in the global blood flow distribution, triggering a compensatory mechanism which in turn affects the blood flow distribution. For example, it has been shown, that a significant reduction of the carotid artery lumen does not lead to a significant decrease of blood

flow to the brain, due to the presence of these compensatory mechanisms [Formaggia et al., 1999].

This reciprocal influence between global or systemic hemodynamics and local hemodynamics has lead to the development of the geometrical multiscale modeling of the cardiovascular system.

The multiscale perspective is important even when the focus lies on local hemodynamics. Artificial boundary conditions (at the inlet and outlet of the region of interest) delimit the segment of interest: they are defined based on the global hemodynamics and modeled using one- or zero-dimensional models.

One-dimensional models are derived using a series of simplifying assumptions from the three-dimensional Navier-Stokes equations. A fundamental aspect of this type of model is that it takes into account the compliance of the vessels, i.e. it represents a reduced-order fluid-structure interaction model, and thus allows for a proper modeling of the wave phenomena. Whereas one-dimensional models are represented through partial differential equations, zero-dimensional models are represented through ordinary differential equations. They model the time-varying spatially averaged pressures and flow rates in a compartment of the cardiovascular system.

Both models are of great importance for the multiscale modeling since they allow for a proper modeling of the fundamental aspects in the cardiovascular circulation in a reasonable amount of time.

Another aspect of interest is the coupling of the simplified models with the three-dimensional model [Formaggia et al., 2001], [Quarteroni et al., 2001], as displayed in Figure 1.1. The coupling is a challenging task due to the different nature of the coupled models. The Navier-Stokes equations are a system of partial differential equations of parabolic type from the velocities' point of view; while the one-dimensional models are hyperbolic, and the zero-dimensional models have no spatial dependence (only time derivatives are present in these equations).

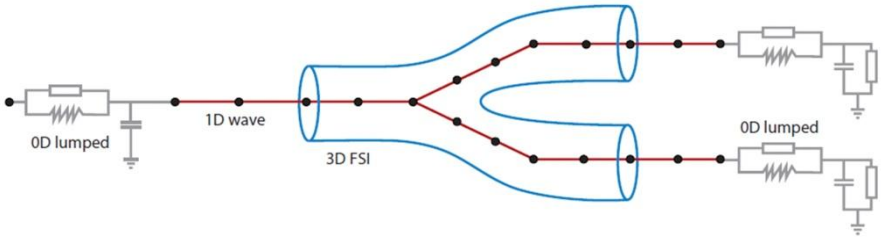

Figure 1.1: Coupling of three-, one- and zero-dimensional models for a multiscale fluid-structure interaction simulation [van de Vosse et al., 2011].

Similar to regular CFD based applications, in case of multiscale models of the arterial circulation the following workflow is employed [Chung, 2002]:

- Pre-processing: the geometry of the application is defined, the volume occupied by the fluid is divided into finite cells (the grid may be uniform or non-uniform) and the physical model is defined. Next, the boundary conditions are defined (the behavior of the fluid at the boundaries of the region of interest is defined);
- The simulation is started and the equations are solved iteratively in space and / or time to determine the steady-state of transient solution;
- Post-processing: the numerical results are analyzed and visualized.

1.2 PATIENT-SPECIFIC MULTISCALE MODELING OF ARTERIAL HEMODYNAMICS

The prerequisite for generating a patient-specific multiscale model is the generation of the anatomical model. During the last decades tremendous progresses have been made in the field of medical imaging, and, hence, nowadays various technologies are available for acquiring the input data required for the reconstruction of anatomical models.

Steinman et al. underlined the fact that the opportunities generated by the state-of-the-art medical imaging techniques come with both advantages and disadvantages. If these techniques are employed correctly, they can help clinicians in understanding the cardiovascular pathologies and boost the development and evaluation of medical devices and therapeutic interventions. The disadvantage is that these tools may lead to large quantities of data, without leading to a similar increase in the understanding of the phenomena that cause the observed results [Steinman et al., 2005].

The first image-based CFD simulations were performed for understanding the role of hemodynamic forces in the development of carotid artery atherosclerosis [Milner et al., 1998] and coronary artery atherosclerosis [Krams et al., 1997]. Furthermore, hemodynamics in abdominal aortic aneurysms [Taylor et al., 1996] and the planning of surgical interventions have been of interest [Taylor et al., 2004]. The above mentioned compartments of the cardiovascular system have been chosen on one hand because of their clinical significance, and on the other hand due to the possibility of properly visualizing the arterial lumen and wall. Thus, the carotid bifurcation is ideal for ultrasound and MRI. The abdominal aorta can be visualized through MRI or CT, while coronary arteries are typically investigated through X-ray angiography.

Significant progress was made in the understanding of the role of hemodynamics forces in the development of coronary plaque [Slager et al., 2005]. An MRI-based study has shown that the locations with large wall shear stress have a higher risk of rupture in case of coronary arteries [Groen et al., 2007]. On the other hand, a hemodynamic study of carotid arteries has indicated that the locations with low wall shear stress tend to have the largest plaque growth [Tang et al., 2008].

Several studies have focused on cerebral aneurysms. Hence, it was concluded that low wall shear stress leads to progressions and rupture of cerebral aneurysms [Shojima et al., 2004]. A subsequent study, performed on 62 patients [Cebral et al., 2005] has shown that the dimension of the aneurysms and the inlet flow rate are correlated. Due to the risks associated with surgical interventions for aneurysms, intact aneurysms are often only monitored clinically, providing thus an ideal setting for studying their evolution. Thus, the roles of low wall shear stress and stagnant blood flow for the evolution of aneurysms have been studies [Boussel et al., 2008].

Remarkable advancements have also been reported in the modeling of the abdominal aorta for diagnosing atherosclerosis and analyzing the evolution of aneurysms [Tang et al., 2006]. Patient-specific hemodynamics have been analyzed in anatomical models reconstructred from MRA (Magnetic Resonance Angiography) medical images. Furthermore phase contrast MRI was employed to determine blood flow velocities at rest. Hemodynamic computations were then performed for the rest state and a state of moderate physical exercise. The latter ones proved that physical exercise is beneficial for the appearance of mechanical stimuli, which in turn trigger long lasting biological processes and protect the arteries from the onset and the evolution of atherosclerosis.

Hemodynamic simulations are not only useful for understanding the arterial circulation but also for planning a patient-specific treatment course. Wilson et al. have described the

development of a software system for planning surgical interventions, proving the utility of a hemodynamic model in the planning of aorto-femoral bypasses for patients with total occlusions in peripheral arteries [Wilson et al., 2005]. This technique was also employed to simulate and compare the effects of total occlusions in vertebral arteries [Hassan et al., 2004].

MRA imaging data was also employed to generate an anatomical model of an inoperable aneurysm in the basilar artery. PC-MRI was used to determine the inlet boundary condition, and CFD techniques were employed to determine blood flow velocities and the wall shear stress distribution in case one of the supplying arteries was blocked [Acevedo-Bolton et al., 2006]. The authors concluded that by modifying the cerebral blood flow, the sections with low wall shear stress can be modified, and the sections with stagnant flow can be diminished (stopping thus the further evolution of the aneurysm).

The first step in the process of image-based patient-specific hemodynamic modeling is the segmentation of the arterial walls. Initially, the segmentation was performed manually on 2D images, whereas the 3D anatomical model was subsequently generated by combining the 2D images [Steinman, 2002]. During the last years a tremendous progress has been made in terms of spatial resolution and image quality. Coupled with stronger graphics processors, this has enabled a real-time reconstruction of 3D anatomical models. A preferred approach is the level-set method, which is typically employed in immersed boundary methods [Antiga et al., 2008]. In case of volumetric images with well-defined arterial walls (as acquired through CT and MR with contrast agent) 3D segmentation is preferred due to the speed and robustness of the methodology. On the other hand, the modification of 3D surfaces is cumbersome, and, hence, in case of low contrast images, 2D segmentation is preferred [Wang et al., 1999]. This technique is employed for example for IVUS (Intravascular Ultrasound) images, which are acquired at non-parallel planes [Slager et al., 2000]. To generate a three-dimensional model of the vessel, a technique called *lofting* is employed, which connects the 2D rings. This technique does not pose any major difficulties in case of single vessels, but is cumbersome to apply in case of bifurcations [Gijsen et al., 2007]. Finally, open-source platforms can be nowadays readily used to generate the three-dimensional models (vmtk, simtk, etc.).

Once the surface of the arterial segments of interest has been determined, a grid with a finite number of elements has to be generated for which the multiscale model will be solved. Commercial or open-source platforms may be employed at this stage. In hemodynamic simulations the quantities of interest may be global hemodynamic properties (like pressure or flow-rate) or local hemodynamic properties (like the wall shear stress). For the former, a relatively coarse grid may be generated (leading thus to a short execution time), while for the latter a denser grid is required (leading to a large execution time). For a reasonable compromise between accuracy and execution speed, adaptive grid refinement techniques are employed, so as to generate a fine grid in the regions of interest and a relatively coarse grid for the rest of the domain.

As described above, to run multiscale simulations in a reasonable amount of time, artificial boundaries are required. At the inlet boundary typically a velocity profile with a pre-defined shape is applied (e.g. flat profile for the ascending aorta, Womersley profile for the carotid artery, etc.). In case measurements are not available for the outlet boundary conditions, these are typically determined based on the dimensions of the vessels and scaling laws [Kassab et al., 2006]. If patient-specific measurements are available (PC-MRI, US) these may be applied directly at the inlet / outlet boundary conditions, but if rigid wall simulations are performed, a correction of phase differences and attenuations, which occur naturally in the cardiovascular

system, need to be performed. Remarkable advancements have been made in the development of multiscale modeling, whereas the artificial boundary conditions of the three-dimensional models are given by one- or zero-dimensional models [Blanco et al., 2007], [Lagana et al., 2005], [Migliavacca et al., 2006]. The usage of reduced-order models comes with the requirement of defining the parameters of these models. Thus, in case of lumped parameter models the resistances, compliances and inertances need to be determined. Subsequently, numerical optimization methods may be applied to adapt the values of the parameters in the reduced order models so to match patient-specific measurements (of pressure and / or flow rate).

An important aspect in the hemodynamic modeling is the extraction of relevant information from large quantities of data generated by the simulation. Most of the studies have focused on the quantities defined at the arterial walls, which are considered to be the most important ones for cardiovascular pathologies. The average wall shear stress and the oscillatory shear index still represent the most often investigated quantities in hemodynamic studies. Besides these, volumetric quantities are also of great interest. Thus, arterial sections with increased blood flow velocities, with recirculation zones or with reversed flow can be determined. To be able to trust the results of hemodynamic simulations, the numerical methods need to be verified and the mathematical models need to be validated (are the equations solved right, and are the right equations being solved?). Very few studies compare the numerical results with well-known analytical solutions (like the Womersley solution in case of oscillating flow in rigid or elastic tubes [Womersley, 1955]. A comparison between numerical and experimental results with very good results was described in [Ku et al., 2005]. The *in vivo* validation of hemodynamic models is much more challenging, since the experimental setup is difficult to control and data acquisition is more cumbersome. A comparison of CFD results with *in vivo* acquired MRI data was performed in [Boussel et al., 2009] for cerebral aneurysms.

Significant advancements have also been made in the multiscale modeling of the coronary circulation. A patient-specific detailed model has been introduced in [Kim et al., 2010], whereas a time-varying elastance model is applied for determining the boundary condition at the inlet of the aorta. For the terminal branches of the coronary circulation specialized lumped parameter models are employed, which take into account the influence of the heart contractions on the coronary blood flow. These contractions lead to a low flow during systole and large flow during diastole. The flow rates, pressures and the wall shear stress in the coronary circulation have been analyzed in this study.

Another multiscale model of the coronary circulation has been introduced in [Sankaran et al., 2012]. The proposed model has been employed for studying coronary artery bypasses in case of severely stenosed arteries.

1.3 MACHINE LEARNING IN HEMODYNAMIC MODELLING

The CFD-based models combine geometrical information extracted from medical imaging with background knowledge on the physiology of the system, encoded in a complex mathematical fluid flow model consisting of partial differential equations which can be solved only numerically. This approach leads to a large number of algebraic equations, making it computationally very demanding [Taylor et al., 2013]. Typically the solution of these models requires a few hours on powerful clusters for high-fidelity models representing the complete three dimensional velocity field to minutes on a workstation for reduced-order models which solve for time-varying pressure and flow rate in each branch [Itu et al., 2012], [Deng et al., 2015].

The computationally demanding aspect of these CFD models and associated image segmentation process prevents adoption of this technology for real-time applications such as intra-operative guidance of interventions. An alternative approach with high predictive power is based on machine learning (ML) algorithms. In this case, the relationship between input data, e.g. the anatomy of a vascular tree, and quantities of interest, is represented by a model built from a database of samples with known characteristics and outcome [Bishop, 2006]. Once the model is trained, its application to unseen data provides results almost instantaneously. Such machine learning models have been used successfully in many medical imaging applications, including automatic heart isolation [Zheng et al., 2008], and segmentation of different organs [Zheng et al., 2011]. This approach has also been used to reproduce the predictive capability of complex, non-linear computational models [Mansi et al., 2013], [Tondel et al., 2011], resulting in a significant reduction in computational requirements compared to the original model.

1.4 PARALLEL PROCESSING IN MULTISCALE HEMODYNAMIC MODELING

The main goal of parallel processing is to reduce the execution time. An application is a good candidate for parallel processing if it processes large quantities of data, if it performs a large number of iterations, or both. The process of parallel programming is typically based on the following steps:

- Problem decomposition;
- Selecting the algorithm;
- Implementation;
- Optimization of execution speed.

Conceptually, the identification of parallelizable components in complex applications is simple, but in practice this may become a challenging task. One key aspect is to define the activities to be performed by each work unit (typically each thread), so that the inherent parallelism is properly exploited. The theoretical speed-up that can be achieved through parallelization is determined by the portion of the application which can be safely parallelized. The speed-up is given by Amdahl's law:

$$S = \frac{1}{(1 - P) + \frac{P}{N}}, \tag{1.1}$$

where S is the execution time speed-up, P is the fraction of the program which can be parallelized, and N is the number of processors or threads which perform the parallel operations. The higher the value of N the lower is the fraction P/N, and the higher will S be. Nevertheless, the most important factor for the parallelization is P, the value of which should as close as possible to one.

To perform a successful parallelization, the following aspects need to be clarified:

- The architecture of the hardware: memory organization, data locality, caching, memory bandwidth, and the execution architecture:
    - SIMT (Single Instruction Multiple Thread): a group of threads execute the same instruction, but different groups of threads can execute different instructions – architecture employed in case of graphics processors [Rodrigues et al., 2008];

- SPMD (Single Program Multiple Data): the same program is executed in multiple instances on multiple processors – architecture used in case of classical multi-core processors;
- SIMD (Single Instruction Multiple Data): all threads execute the same instructions at each time point – architecture used in case of vectorial processors;

· Programming models and compilers: parallel execution models, types of available memory, data arrangement in memory, etc.
· Implementation technqiues: the transformation / replacement of sequential algorithms with parallel algorithms, understanding the scalability and the implications of the bandwidth for each algorithm, etc.;
· Extensive domain know-how: numerical methods, models, accuracy requirements, etc.

The currently most used parallel processor is the Graphics Processing Unit (GPU). Its popularity is given on one hand by the relatively low cost and, on the other hand, by the ease of programming [Kirk et al., 2010].

1.5 OVERVIEW OF PART II

Chapter 2 introduces a hierarchical parameter estimation framework for performing patient-specific hemodynamic computations in arterial models which use structured tree boundary conditions. A calibration problem is formulated at each stage of the hierarchical framework, which seeks the fixed point solution of a nonlinear system of equations. Common hemodynamic properties, like resistance and compliance, are estimated at the first stage in order to match the objectives given by clinical measurements of pressure and/or flow rate. The second stage estimates the parameters of the structured trees so as to match the values of the hemodynamic properties determined at the first stage. A key feature of the proposed method is that, to ensure a large range of variation, two different structured tree parameters are personalized for each hemodynamic property. First, the second stage of the parameter estimation framework is evaluated based on the properties of the outlet boundary conditions in a full body arterial model: the calibration method converges for all structured trees in less than ten iterations. Next, the proposed framework is successfully evaluated on a patient-specific aortic model with coarctation: only six iterations are required for the computational model to be in close agreement with the clinical measurements used as objectives, and, overall, there is a good agreement between the measured and computed quantities.

Chapter 3 introduces a parameter estimation framework for automatically and robustly personalizing aortic hemodynamic computations from 4D Magnetic Resonance Imaging data. The framework is based on a reduced-order multiscale fluid-structure interaction blood flow model, and on two calibration procedures. First, Windkessel parameters of the outlet boundary conditions are personalized by solving a system of nonlinear equations. Second, the regional mechanical wall properties of the aorta are personalized by employing a non-linear least squares minimization method. The two calibration procedures are run sequentially and iteratively until both procedures have converged. The parameter estimation framework was successfully evaluated on 15 datasets from patients with aortic valve disease. On average, only 1.27 ± 0.96 and 7.07 ± 1.44 iterations were required to personalize the outlet boundary conditions and the regional mechanical wall properties respectively. Overall, the computational model was in close agreement with the clinical measurements used as objectives (pressures, flow rates, cross-sectional areas), with a maximum error of less than 1%. Given its level of automation,

robustness, and the short execution time (6.2 ± 1.2 minutes on a standard hardware configuration), the framework is potentially well suited for a clinical setting.

Chapter 4 introduces a methodology for separating the total stiffness of arteries, determined in vivo, into stiffness of the arterial wall and stiffness of the surrounding tissue. An effective perivascular pressure is considered which introduces a radial constraint. Next, based on vivo data, acquired at diastolic pressure, the cross-sectional area at zero pressure is estimated. Finally, the stiffness of the arterial wall and of the surrounding tissue are determined based on a model with two parallel springs. By employing a reduced-order multiscale model, the methodology is used for studying the global effects of surrounding tissue support on arterial hemodynamics. The main effects are: higher wave speed, earlier arriving backward travelling pressure and flow rate waves, lower total compliance, higher pressure pulse, and reduced arterial cross-sectional areas.

Chapter 5 introduces a model-based approach for the non-invasive estimation of patient specific, left ventricular PV loops. A lumped parameter circulation model is used, composed of the pulmonary venous circulation, left atrium, left ventricle and the systemic circulation. A fully automated parameter estimation framework is introduced for model personalization, composed of two sequential steps: first, a series of parameters are computed directly, and, next, a fully automatic optimization-based calibration method is employed to iteratively estimate the values of the remaining parameters. The proposed methodology is first evaluated for three healthy volunteers: a perfect agreement is obtained between the computed quantities and the clinical measurements. Additionally, for an initial validation of the methodology, the PV loop for a patient with mild aortic valve regurgitation was computed and the results were compared against the invasively determined quantities: there is a close agreement between the time-varying LV and aortic pressures, time-varying LV volumes, and PV loops.

Chapter 6 introduces a machine learning-based model for predicting FFR as an alternative to physics-based approaches is presented. The model is trained on a large database of synthetically generated coronary anatomies, where the target values are computed using the physics-based model. The trained model predicts FFR at each point along the centerline of the coronary tree, and its performance was assessed by comparing the predictions against physics-based computations, and against invasively measured FFR for 87 patients and 125 lesions in total. Correlation between machine learning and physics-based predictions was excellent (0.9994, $p < 0.001$) and no systematic bias was found in Bland-Altman analysis: mean difference was -0.00081 ± 0.0039. Invasive FFR $\leq$ 0.80 was found in 38 lesions out of 125, and was predicted by the machine learning algorithm with a sensitivity of 81.6%, a specificity of 83.9%, and an accuracy of 83.2%. The correlation was 0.729 ($p < 0.001$). Compared to the physics based computation, average execution time was reduced by more than 80 times, leading to near real-time assessment of FFR. Average execution time went down from 196.3 ± 78.5 seconds for the CFD model to around 2.4 ± 0.44 seconds for the machine learning model on a workstation with 3.4 GHz Intel i7 8-core processor.

The geometric multigrid method (GMG) is one of the most efficient algorithms for solving these systems and is well suited for parallelization. In *chapter 7* an in-depth analysis of a GPU-based GMG implementation is performed and the results are compared against an optimized preconditioned conjugate gradient method. The tests indicate that the smoothing step is the most time consuming operation, and the best performing GMG variant is the V-cycle scheme with 312 smoothing step configuration (3 iterations during restriction, 1 at the coarsest level, and 2 iterations during prolongation). The discretization stencil has a major effect on the runtime and

its choice requires a trade-off between execution time performance and numerical accuracy. Overall, the GMG method offers a speed-up of 7.1x-9.2x over the PCG method on the same hardware configuration, while also leading to a smaller average residual.

Stencil based algorithms are used intensively in scientific computations. Graphics Processing Units (GPU) based implementations of stencil computations speed-up the execution significantly compared to conventional CPU only systems. In *chapter 8* double precision stencil computations are considered, which are required for meeting the high accuracy requirements, inherent for scientific computations. Starting from two baseline implementations (using two dimensional and three dimensional thread block structures respectively), different optimization techniques are employed which lead to seven kernel versions. Both Fermi and Kepler GPUs are used, to evaluate the impact of different optimization techniques for the two architectures. Overall, the GTX680 GPU card performs best for a kernel with 2D thread block structure and optimized register and shared memory usage. The results indicate that, whereas shared memory is not essential for Fermi GPUs, it is a highly efficient optimization technique for Kepler GPUs (mainly due to the different L1 cache usage). Furthermore, the performance of Kepler GPU cards designed for desktop PCs and notebook PCs, is evaluated: the ratio of execution time is roughly equal to the inverse of the ratio of power consumption.

2. Personalized Blood Flow Computations: A Hierarchical Parameter Estimation Framework for Tuning Boundary Conditions

2.1 INTRODUCTION

The vascular system is composed of around ten billion vessels, whose size range over several orders of magnitude. Hence, the full-scale spatial (3D) or even reduced-scale spatial modeling (1D) of the entire system is computationally not feasible. As a result, only a certain region of the vascular system, which is of main interest, is modeled spatially, whereas the remainder of the system is lumped into non-spatial models, which provide the artificial boundary conditions (inlet and outlet) for the region of interest. Depending on the availability of in-vivo measurements and the underlying assumptions of the model, researches typically use one of the following inlet boundary condition: (i) Time-varying velocity (or flow rate) profile [Olufsen et al., 2000], [LaDisa et al., 2011], or (ii) A lumped model of the heart coupled at the inlet [Formaggia et al., 2006], [Coogan et al., 2011]. The design of outlet boundary conditions is more challenging, since:

- the distal vasculature (microvasculature) generates the bulk part of the total resistance, and is thus responsible for flow distribution and the overall pressure level in the region of interest;
- flow and pressure waves propagat**e** beyond the outlet locations. As the vessels change their geometry and structure, and bifurcate, the waveforms change. Furthermore, waves

are reflected and propagated backwards into the region of interest.

Different approaches have been proposed for specifying the outlet boundary conditions, ranging from pressure or flow rate profiles to lumped parameter models (0D models). For an accurate patient-specific computation, the role of physiologically sound boundary conditions is well appreciated in the literature. Typically, the effect of distal vasculature is modeled by outlet boundary conditions coupled with the computational domain (region of interest), resulting in a geometrical multiscale model. Thus, the boundary conditions are represented by lumped parameter models, which are designed to capture one (or more) of the i) total resistance, ii) total compliance, and iii) the wave propagation and reflection effects in the distal vasculature. The most widely used lumped parameter model is the three-element windkessel model [Westerhof et al., 2009], which is characterized by its simplicity (only three parameters), and ability to capture two important characteristics of the distal circulation (compliance and resistance). The small number of parameters simplifies the parameter estimation procedures applied for personalizing blood flow computations. The drawback of the windkessel model is that it is not able to capture the wave propagation and reflection phenomena in the distal vasculature, and, thus, their effect on the region of interest,

A different boundary condition, specifically designed to capture the wave propagation phenomena, is the structured tree model. It is based on the work in [Taylor, 1966] and was subsequently developed by Olufsen et al. [Olufsen et al., 1999]. The distal vasculature is modeled as a simple geometric structure and, following a set of simplifying assumptions, an analytical expression, which relates flow rate and pressure, is obtained. Due to its characteristics, the structured tree models all three aspects which are of interest for an outlet boundary condition. However, since the resistance and the compliance are not explicitly parameterized in the mathematical representation of the structured tree, it is more difficult to design parameter estimation procedures for personalizing blood flow computations which use this type of boundary condition. Furthermore, the original formulation in [Olufsen, 1998] can only be used for periodic blood flow computations. Due to these aspects, the structured tree has not been widely used for blood flow computations.

However, the structured tree boundary condition has received an increased attention during the last couple of years. Cousins et al. introduced a new, simpler derivation of the structured tree impedance and performed a sensitivity analysis with respect to its parameters [Cousins et al., 2012]. In a subsequent study, a modified formulation was derived, which can be used to model transient flows [Cousins et al., 2013]. Recently, the structured tree formulation has been successfully used in hemodynamic computations of retinal arteries and veins [Malek et al., 2015], and in the pulmonary arterial and venous circulation [Qureshi et al., 2014].

In a clinical scenario, the values of model parameters are not available on a per-patient basis. Instead, multiple pressure or flow measurements are usually available for each patient. A clinically feasible and accurate flow computation should not only be in agreement with these measurements, but should also have means to model other hemodynamic states for the same patient. To achieve this, one should estimate a set of personalized model parameters, while ensuring that the computations match the measured data. Since the outlet boundary conditions are mainly responsible for the overall pressure level and the flow distribution, the personalization procedures typically focus on the parameters of the outlet boundary conditions.

Different calibration procedures for outlet boundary conditions have been proposed. Olufsen et al. described a calibration method for determining the dynamic cerebral blood flow response to sudden hypotension during posture change [Olufsen et al., 2002].

An optimization-based iterative calibration method for the windkessel models was suggested [Spilker et al., 2010], where the input was specified by non-invasively acquired systolic/diastolic pressures and, in some cases, additional flow data. The windkessel parameters were obtained by solving a system of nonlinear equations, formulated based on a set of objectives for the pressure and flow rate waveforms at various locations. A more efficient optimization method was proposed in [Itu et al., 2015], which resulted in faster convergence and was shown to be robust against the choice of initial guess.

An adjoint based method for calibrating the windkessel parameters was also proposed , where the Jacobian was computed without the use of finite-differences [Ismail et al., 2015]. Furthermore, a reduced-order model with resistance outlet boundary conditions was introduced [Blanco et al., 2012], under which the terminal resistance values of the arterial model of the arm were adapted to obtain desired flow rate distributions between vascular territories. A competitive alternative to the above mentioned optimization based methods is represented by filtering based approaches [Bertoglio et al., 2012].

Recently, a more rigorous calibration of structured tree parameters was presented [Cousins et al., 2014], where a trust region method was applied to adapt the length-to-radius ratio to achieve a computational result that agreed with the measured flow distribution.

In this chapter an iterative hierarchical parameter estimation framework is introduced for personalizing hemodynamic computations which use structured trees as outlet boundary conditions [Itu et al., 2017]. The structured tree parameters are estimated in a manner that minimizes the error between the computed and measured pressure and flow data. A hierarchical personalization approach is employed since common vessel properties, like resistance and compliance, are not explicitly parameterized in the mathematical representation of the structured tree. The first stage estimates the resistances and the compliances to match the patient-specific quantities, while the second stage estimates the parameters of the structured trees to match the resistances and compliances determined at the first stage. The second stage of the framework is first separately evaluated using the parameter values of the windkessel models applied as outlet boundary conditions in a full body arterial model [Stergiopulos et al., 1992]. Next, a patient-specific aortic coarctation (CoA) case is used to test and validate the entire framework. Results are compared against a configuration which uses windkessel models for imposing the outlet boundary conditions.

2.2 METHODS

2.2.1 Structured tree boundary condition

The structured tree is an asymmetric binary tree, with axisymmetric vessels of constant radius. At the bifurcations, the radius of each daughter vessel is specified by a power law relationship:

$$r_p^{\chi} = r_{d1}^{\chi} + r_{d2}^{\chi}, \tag{2.1}$$

where the subscripts p, $d1$ and $d2$ refer to the parent vessel, and the two daughter vessels respectively. The power law is based on the assumption that the energy required for blood flow

is minimal (an optimal value of ξ = 3.0 was determined) [Murray, 1926(a)]. Subsequently, several values have been proposed for the power coefficient ξ, ranging from 2.1 to 3 [Kamiya et al., 1980], [Zains et al., 1987], [Kassab et al., 1995], [Zhou et al., 1999].

The bifurcations of the structured tree are asymmetrical. Hence, the radii of the daughter vessels are computed based on the radius of the parent vessel, using:

$$r_{d1} = \alpha r_p, \quad r_{d2} = \beta r_p, \tag{2.2}$$

where are α and β are scaling parameters. To compute α and β the asymmetry ratio γ is introduced:

$$\gamma = \left(\frac{r_{d2}}{r_{d1}} \right)^{\xi}. \tag{2.3}$$

The two scaling parameters are then given by:

$$\alpha = \left(1 + \gamma^{x/2}\right)^{-1/x}, \quad \beta = \alpha \sqrt{\gamma}. \tag{2.4}$$

Starting from a vessel with a root radius, the structured tree bifurcates until the radius of the vessels becomes smaller than a certain minimum radius. Previous studies [Iberall, 1967] have shown that, statistically, the length of a vessel can be expressed in terms of its radius. Hence, a length-to-radius ratio, l_{rr}, is used to determine the lengths of the vessels in the structured tree.

Finally, the material properties of the vessel walls are specified. Since the small arteries are composed of the same type of tissue as the large arteries, the relationship employed for the large arteries, based on a best fit to experimental data, can also be used for the wall properties of the structured tree [Olufsen et al., 2000]:

$$\frac{Eh}{r_0}(x) = k_1 \times \exp(k_2 \times r_0(x)) + k_3, \tag{2.5}$$

where E is the Young's modulus, h is the wall thickness, r_0 is the initial radius, and k_1, k_2, k_3 are empirically determined parameters. Table 2.1 displays the reference parameter values for the structured tree adopted below.

Table 2.1: Reference parameter values defining the structure and properties of the structured tree.

Parameter	Value
γ	0.4048
ξ	2.7
α	0.9087
β	0.5782
l_{rr}	25.0
k_1	$2 \times 10^7 \; g/(s^2 \times cm)$
k_2	$-25.53 \; cm^{-1}$
k_3	$4.65 \times 10^5 \; g/(s^2 \times cm)$

The governing equations for the blood flow in the structured tree are derived from the axisymmetric Navier-Stokes equations [Olufsen, 1998]. Since the viscous effects are dominant in

the small arteries, the nonlinear inertial terms can be neglected. Under periodic flow and pressure conditions, an analytical solution is determined in the frequency domain:

$$Q(x,w) = a \times \cos(wx/c) + b \times \sin(wx/c), \tag{2.6}$$

$$P(x,w) = i\sqrt{\frac{r}{C_A A_0 (1 - F_J)}}(- a \times \sin(wx/c) + b \times \sin(wx/c)), \tag{2.7}$$

where ρ is the density, c is the wave propagation speed and F_J depends on the Bessel functions, and is computed using the Womersley number. C_A is the area compliance and is given by:

$$C_A = \frac{1}{k_1 \times exp(k_2 \times r_0(x)) + k_3} \frac{3 \times A}{2}, \tag{2.8}$$

where A is the cross-sectional area.

The root impedance of the structured tree is computed recursively using the formula:

$$Z(0,w) = \frac{ig^{-1} b \sin(wL/c) + Z(L,w)\cos(wL/c)}{\cos(wL/c) + igZ(L,w)\sin(wL/c)}, \tag{2.9}$$

where $g = cC = \sqrt{CA_0(1 - F_J)/r}$, $Z(0,w)$ is the impedance at the inlet of the vessel segment, and $Z(L,w)$ is the impedance at the outlet of the vessel segment. The root impedance is then applied as structured tree outlet boundary condition:

$$P(x,w) = Z(x,w) \times Q(x,w). \tag{2.10}$$

By applying an inverse Fourier transformation, $Z(x,w)$ is converted into $z(x,t)$ and (2.10) is rewritten using the convolution theorem:

$$p(x,t) = \int_{t-T}^{t} q(x,t) z(x,t-t)\,dt, \tag{2.11}$$

where T is the period.

2.2.2 Parameter estimation framework

A hierarchical parameter estimation framework is introduced for multiscale blood flow computations which use structured tree boundary conditions (Figure 2.1).

Herein, for the flow computations a reduced-order geometrical multiscale model combining a one-dimensional model and the structured tree model is used as proof-of-concept. One-dimensional models have been used in the past to compute time-varying flow rate and pressure waveforms in full body arterial models [Reymond et al., 2011]. Since the predictions have been shown to be accurate, this model has more recently also been employed for computations under pathologic conditions in specific parts of the circulation: coronary atherosclerosis [Itu et al., 2012], aortic coarctation [Itu et al., 2013a], abdominal aorta aneurysm [Low et al., 2012], and femoral bypass [Willemet et al., 2013]. The details of the one-dimensional model used herein are described in [Itu et al., 2012], [Itu et al., 2013(a)]. The inlet boundary condition is provided by time-varying flow rate profiles, while a structured tree is coupled at each outlet of the anatomical model.

Both stages of the parameter estimation framework use automated iterative calibration methods for estimating the parameter values. These are described below.

2.2.2.1 Calibration method for estimating resistance and compliance values

The calibration method at the first stage (Figure 2.1) automatically estimates the total resistances and the compliance of the structured trees to ensure that the computed pressure and flow rate values match the measurements. The parameter estimation procedure used at the first stage is a modified version of a previously introduced framework [Itu et al., 2015].

The parameter estimation problem is formulated as a numerical optimization problem, the goal of which is to find a set of parameter values for which a set of objectives are met. Since the number of parameters $\mathbf{x}_i$ to be estimated is set equal to the number of objectives, the parameter estimation problem becomes a problem of finding the root for a system of nonlinear equations. Each equation of the system is formulated as the difference between the computed value of an objective – $(\cdot)_{comp}$ (determined using the multiscale model) and its target value – $(\cdot)_{target}$. These differences are called residuals ($\mathbf{r}(\mathbf{x}_i)$):

$$\mathbf{r}(\mathbf{x}_i) = \left\{(\cdot)_{comp} - (\cdot)_{target}\right\} = \{\mathbf{0}\}. \tag{2.12}$$

To evaluate the objectives $(\cdot)_{comp}$ at each iteration, the multiscale model is run exactly once. Moreover, parameter and objective values are normalized based on characteristic values. To find a good initial solution, the optimization problem is first solved for a distal vasculature model composed from the structured trees employed in the multiscale model (step 1 in Figure 2.1a): a grid of physiological parameter value sets is considered, and the initial solution, $\mathbf{x}_0$, is chosen as the parameter value set leading to the smallest L_2 norm for the objective function $\mathbf{r}(\mathbf{x})$. This initial solution is then further refined by employing a dogleg trust-region method, determining thus $\mathbf{x}_0$ to be used in the following steps.

Next, the Jacobian of the system of equations is computed using finite differences (steps 2, 3 and 4). The finite differences of the parameters, to be used for the computation of the Jacobian, are called in the following characteristic step sizes, s_j^{char}. To determine the characteristic step sizes, a set of characteristic values for the objective function are chosen, r_i^{char}, and a fixed point iteration method is applied. The fixed point iteration method consists of two sequential steps. First, the characteristic step size values are computed:

$$s_j^{char} = 1 \Big/ \sqrt{\sum_{i=1}^{n_{eq}} \left(J_{ij} / r_i^{char}\right)}. \tag{2.13}$$

Next, the Jacobian matrix is computed:

$$J_{ij} = \frac{1}{s_j^{char}} \left[\mathbf{r}\left(\mathbf{x}_0 + \frac{1}{2} s_j^{char} \mathbf{d}_j\right) - \mathbf{r}\left(\mathbf{x}_0 - \frac{1}{2} s_j^{char} \mathbf{d}_j\right) \right] \times \mathbf{d}_i, \tag{2.14}$$

where $\mathbf{d}_i$ and $\mathbf{d}_j$ represent the unit vectors in the ith and jth direction. These two steps are iterated until the characteristic step size is consistent with the chosen characteristic objective function.

Next, the multiscale blood flow model is set up (step 5) and run, and the objective residuals are evaluated (step 6). The parameter values for the first run with the multiscale model are based on the solution obtained for the distal vasculature model ($\mathbf{x}_0$).

The optimization problem is terminated if all residuals are smaller than the tolerance limit, set equal to $r_i^{char}/10$. If this condition is not met, the parameter values are updated using a quasi-Newton method. First the previously computed Jacobian is updated (step 7 – since computations with the multiscale model are expensive the Jacobian is only updated and not recomputed):

$$\boldsymbol{J}_{i+1} = \boldsymbol{J}_i + \frac{\left[\boldsymbol{r}(\boldsymbol{x}_{i+1}) - \boldsymbol{r}(\boldsymbol{x}_i) - \boldsymbol{J}_i \boldsymbol{s}_i\right]\left(\boldsymbol{D}_s^2 \boldsymbol{s}_i\right)^T}{\boldsymbol{s}_i^T \boldsymbol{D}_s^2 \boldsymbol{s}_i}, \tag{2.15}$$

where $\boldsymbol{s}_i = \boldsymbol{x}_{i+1} - \boldsymbol{x}_i$ is the current step and $\boldsymbol{D}_s$ is a diagonal scaling matrix:

$$\left(D_s\right)_{ij} = \begin{cases} 1/s_j^{typ}, & i = j \\ 0, & i \neq j \end{cases} \tag{2.16}$$

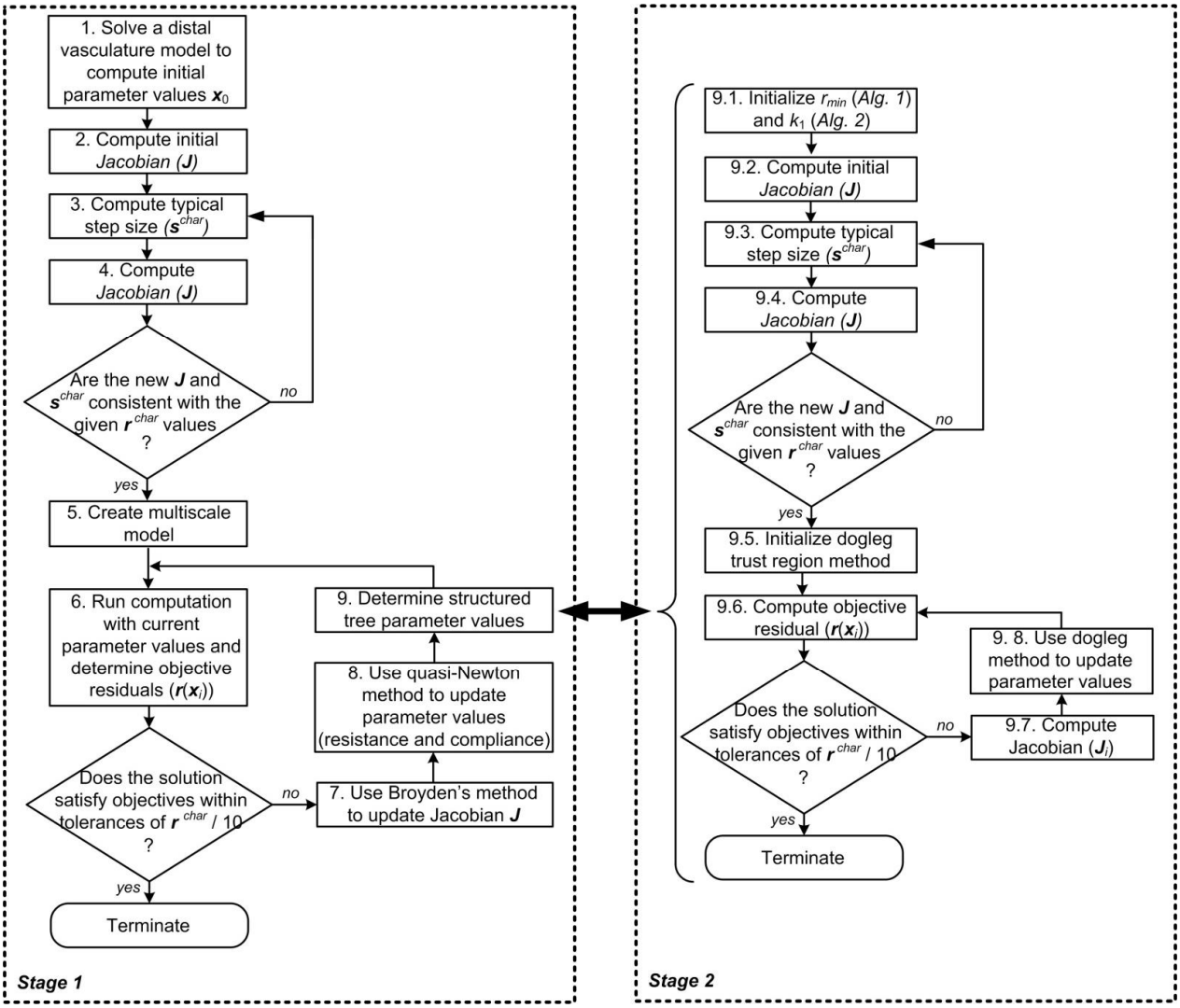

Figure 2.1: Hierarchical parameter estimation framework for multiscale blood flow computations which use structured tree boundary conditions: *Stage 1* (left) - Calibration method which estimates the total resistances and the compliance of the structured trees; *Stage 2* (right) - Calibration method which estimates the structured tree parameters so as to match the total resistance and the compliance computed at stage 1.

Next, the new parameter values (the total resistance and compliance) are estimated (step 8):

$$\boldsymbol{x}_{i+1} = \boldsymbol{x}_i - \boldsymbol{J}_i^{-1}\boldsymbol{r}(\boldsymbol{x}_i). \tag{2.17}$$

Finally, the parameters of the structured trees are determined (step 9) as described below.

2.2.2.2 Calibration method for estimating structured tree parameter values

The second stage of the parameter estimation framework (Figure 2.1) estimates the parameters of the structured trees so as to match the resistances and compliances determined at the first stage (at step 8 in Figure 2.1). Three approaches have been proposed previously for adapting the total resistance represented by the structured tree:

- impose a resistance at each terminal vessel of the structured tree [Olufsen, 1998];
- adapt the minimum radius, r_{min}, at which the structured tree is terminated [Cousins et al., 2012];
- adapt the length-to-radius, l_{rr}, which determines the length of each vessel in the structured tree [Cousins et al., 2014].

To model a large variety of hemodynamic states for the same patient (for example: rest, light exercise, intense exercise, etc.) the resistance has to be adapted over a wide range of values. Hence, for the present work a combination of minimum radius and resistance imposed at the terminal vessels of the structured tree was used to set the total resistance. Since the terminal vessels have approximately the same radius, equal terminal resistances are assumed. The minimum radius is used for coarse calibration, and the terminal vessel resistance for fine calibration.

No methods were previously reported in literature for matching a given compliance value. To match a given target compliance, which can vary over a wide range for different patient states, the parameters k_1 and k_3 in (2.5) are adapted: k_1 is used for the coarse calibration, whereas k_3 is used for fine calibration.

To find a good initial solution, the coarse calibration algorithms adapt r_{min} and k_1 at the first step in Figure 2.1 (step 9.1). Algorithm 1 is used to initialize r_{min}. An initial value of 50μm is used, which corresponds approximately to the start of the arteriolar level. If the computed total resistance, R_{comp}, obtained with a zero terminal resistance, is lower than the target value, the algorithm terminates. Otherwise it progressively increases the minimum radius until the computed total resistance becomes lower than the target value. Algorithm 1 ensures that a positive terminal resistance is required for obtaining the target resistance.

Algorithm 1. Initialization of structured tree minimum radius.

```
Set r_min = 0.005 cm
while (true)
        Compute total resistance (R_comp) using r_min and R_term = 0.0
        if R_comp < R_target
                break
        else
                r_min = r_min + 0.001
        end (if)
end (while)
```

Algorithm 2 initializes parameter k_1. Initially the value displayed in Table 2.1 is used and k_3 is set to 0. A similar approach as in algorithm 1 is used, and the value of k_1 is progressively decreased until the computed compliance becomes larger than the target compliance.

Algorithm 2. Initialize wall properties.

Set $k_1 = 2 \cdot 10^7$, $k_3 = 0$
while (true)
    Compute total compliance (C_{comp})
    if $C_{comp} > C_{target}$
        break
    else
        $k_1 = k_1 - 0.1 \cdot 10^6$
    end (if)
end (while)

The methodology used for fine calibration is similar to the one employed at the first stage of the parameter estimation framework. The structured tree parameters are determined as the solution of a system of nonlinear equations with a root where the computed properties of the structured tree and the target values match:

$$\mathbf{r}\begin{pmatrix} R_{term} \\ k_3 \end{pmatrix} = \begin{pmatrix} R_{comp} - R_{target} \\ C_{comp} - C_{target} \end{pmatrix} = \begin{pmatrix} 0 \\ 0 \end{pmatrix}, \tag{2.18}$$

where R_{term} is the terminal resistance imposed at each outlet of the structured tree, R_{comp} is the computed resistance of the structured tree, R_{target} is the target resistance, C_{comp} is the computed compliance and C_{target} is the target compliance.

Since determining the actual resistance and compliance of the structured tree is computationally fast, the Jacobian is recomputed at each iteration. Hence, instead of a quasi-Newton method, the dogleg trust region method was directly used.

R_{comp} is determined directly from $z(x,t)$ since the total resistance of the structured tree is equal to the impedance computed for a zero frequency in (2.9). The compliance C_{comp} is computed analytically by summing up the volume compliances of all vessels in the structured tree. The volume compliance of a vessel is determined from the area compliance:

$$C_{an} = C_A \times l_{rr} \times r, \tag{2.19}$$

where r is the radius of the corresponding vessel.

2.3 RESULTS

To evaluate the performance of the proposed parameter estimation framework, a patient-specific coarctation anatomical model reconstructed from MRI images was used as test case. The calibration framework ensures that the computation is personalized, and, consequently, computed pressure and flow values are in close agreement with the clinical measurements. However, first results are reported for a test which was designed to separately evaluate the second stage of the parameter estimation framework, based on the parameters of the outlet boundary conditions in a full body arterial model.

Blood is modeled as an incompressible Newtonian fluid with a density of 1.050 g/cm3 and a dynamic viscosity of 0.040 dynes/(cm^2·s). The grid size is 0.05cm, while the time-step (limited by the CFL-condition) is set equal to 2.5e-5s.

2.3.1 Full body arterial model

To evaluate the second stage of the parameter estimation framework, the distal vasculature models (outlet boundary conditions) of a full body arterial tree introduced in [Stergiopulos et al., 1992] were used. Specifically, the total resistance and total compliance values of the outlet boundary conditions were used as target values, and the calibration method in Figure 2.1 was run separately for each terminal vessel.

The calibration method successfully converged for each structured tree (only 2-10 iterations were required) and the results are displayed in Table 2.2. The minimum radius at which the structured tree terminates was larger than 0.005 cm for some arteries: in these cases the total initial resistance was larger than the target value, even if the terminal resistance was set to zero. Generally, the terminal resistances imposed at the terminal sites of the structured tree were three to five orders of magnitude larger than the total resistance of the structured tree.

For calibrating the compliance, algorithm 2 modified the value of k_1, indicating that for obtaining the target compliance with a positive value for k_3, regularly a smaller value was required than the initial value displayed in Table 2.1.

Table 2.2: Calibration results obtained by applying the second stage of the parameter estimation framework for adapting the structured tree parameters of the outlet boundary conditions in a full body arterial model [24].

Artery	r_{root} [cm]	R_{target} / R_{comp} [10^3 g/)cm^4·s)]	C_{target} / C_{comp} [10^{-6} cm^4·s^2/g]	r_{min} [cm]	R_{term} [10^6 g/(cm^4·s)]	k_1 [g/(s^2·cm)]	k_3 [g/(s^2·cm)]	Nr. iter.
Carotid	0.083	139.0	3.27	0.010	1.85	$1.3\cdot10^6$	$11.83\cdot10^3$	4
Interosseus	0.091	84.3	0.69	0.015	$91.3\cdot10^{-3}$	$9.0\cdot10^6$	$81.64\cdot10^3$	4
Tibal anterior	0.13	55.9	2.90	0.007	4.746	$4.0\cdot10^6$	$33.7\cdot10^3$	3
Tibal posterior	0.141	47.7	3.43	0.007	12.13	$6.0\cdot10^6$	$28.34\cdot10^3$	4
Radial	0.142	52.8	3.12	0.005	11.26	$8.0\cdot10^6$	$3.31\cdot10^3$	2
Intercostals	0.150	13.9	36.4	0.038	$12.6\cdot10^{-3}$	$2.0\cdot10^6$	$19.37\cdot10^3$	4
Inf. Mesenteric	0.160	68.8	2.36	0.005	578.0	$2.0\cdot10^7$	$72.4\cdot10^3$	7
Gastric	0.180	54.1	2.91	0.005	651.6	$2.0\cdot10^7$	$269.9\cdot10^3$	8
Ulner	0.183	60.1	2.57	0.005	867.8	$2.0\cdot10^7$	$375.0\cdot10^3$	8
Vertebral	0.183	52.8	2.96	0.005	659.9	$2.0\cdot10^7$	$300.5\cdot10^3$	7
Femoral	0.186	47.7	3.29	0.005	597.2	$2.0\cdot10^7$	$287.7\cdot10^3$	7
Iliac	0.200	79.4	1.78	0.005	2073	$2.0\cdot10^7$	$940.5\cdot10^3$	10
Hepatic	0.220	36.3	4.05	0.005	846.6	$2.0\cdot10^7$	$546.5\cdot10^3$	9
Renal	0.260	11.3	13.35	0.005	2245	$2.0\cdot10^7$	$284.0\cdot10^3$	8
Splenic	0.275	23.2	29.74	0.005	1141.3	$2.0\cdot10^7$	$826.5\cdot10^3$	9
Sup. Mesenteric	0.435	9.3	91.07	0.005	2018	$2.0\cdot10^7$	$1605\cdot10^3$	10

These results demonstrate that the structure tree parameters can be adapted so as to match physiological resistance and compliance values of distal vasculature models. Eq. (2.18) may not have a solution if either of the two hemodynamic properties has unphysiological target values.

Furthermore the calibration method is computationally efficient: since the number of iterations is reduced and both the total resistance and the compliance of the structured trees are computed analytically at each iteration, the total execution time required for calibrating one structured tree is less than 3 seconds on an Intel i7 CPU core with 3.4 GHz.

2.3.2 Reduced-order patient-specific flow computation for aortic coarctation

Computational fluid dynamics (CFD) based methods have been proposed in the past for non-invasive evaluation of trans-stenotic pressure drop [Itu et al., 2013(a)], [Keshavarz-Motamed et al., 2011], [LaDisa et al., 2011], [Ismail et al., 2013]. To accurately estimate the pressure drop, the solution of the hemodynamic model should match the measured pressure and flow-data.

The patient-specific anatomical model used herein [***CFD Challenge, 2013], [Pant et al., 2014] contains the ascending aorta, three supra-aortic branches, the aortic arch, and the descending aorta with coarctation (Figure 2.2a). Figure 2.2b displays the reduced-order multiscale model corresponding to the CoA patient-specific geometry.

The measured ascending aorta flow rate profile is directly used as inlet boundary condition while time-averaged flow splits are provided for each outlet. The final goal is to accurately compute the trans-coarctation pressure drop.

The objectives at the first stage of the parameter estimation problem are formulated based on the requirement of matching the flow splits at the outlets, the maximum flow rate in the descending aorta, and the systolic and diastolic pressures in the ascending aorta. The maximum descending aorta flow rate has been introduced as objective since it represents one of the main determinants for the peak-to-peak trans-coarctation pressure drop, a measure which is typically used to assess the functional significance of the coarctation [LaDisa et al., 2011]. The distal vasculature model used in the first step of the calibration for finding a good initial solution is displayed in Figure 2.2c.

To create the multiscale model (step 5 in Figure 2.1) the vascular modeling toolkit (vmtk [***vmtk, 2014]) was used: the centerline and the cross-sectional areas along the centerline were extracted. Next, for each branch of the anatomical model several one-dimensional segments with longitudinally varying cross-sectional areas were used so as to match as closely as possible the three-dimensional model.

To enable accurate pressure computation in the coarcation region, a locally defined pressure-drop model is embedded into the reduced-order blood flow model, leading to a hybrid formulation. This is done to account for the complex shape of the coarctation and its impact on the pressure drop across the respective vessel segment.

The parameters to be estimated at the first stage of the parameter estimation framework are properties of the distal vasculature models: the total resistances of the three supra-aortic vessels and of the descending aorta, the total compliance of the supra-aortic branches, and the compliance of the descending aorta.

The following system of nonlinear equations is solved at the first stage of the parameter estimation framework to determine the parameter values:

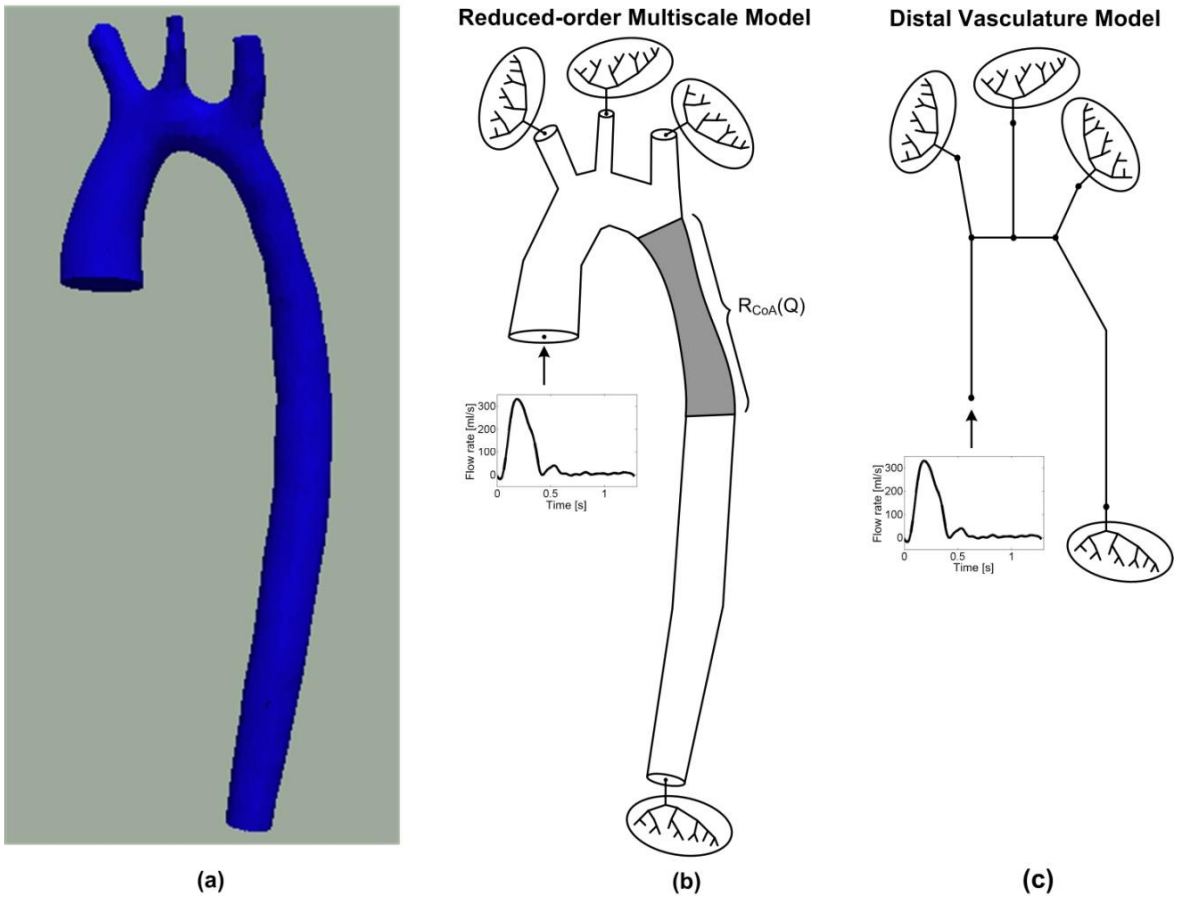

Figure 2.2: (a) Proximal aorta geometry with coarctation; (b) Reduced-order multiscale model used for determining the structured tree parameter values of the patient-specific model; (c) 0D model used during the first step of the model personalization algorithm for finding an initial solution of calibration problem.

$$\begin{pmatrix} R_{t\text{-}BC} \\ R_{t\text{-}LCC} \\ R_{t\text{-}LS} \\ R_{t\text{-}DAo} \\ C_{SupraAo} \\ C_{DAo} \end{pmatrix} = \begin{pmatrix} (P_{\max})_{comp} - (P_{\max})_{target} \\ (P_{\min})_{comp} - (P_{\min})_{target} \\ (F_{LCC})_{comp} - (F_{LCC})_{target} \\ (F_{LS})_{comp} - (F_{LS})_{target} \\ (F_{DAo})_{comp} - (F_{DAo})_{target} \\ (Q_{DAo\text{-}\max})_{comp} - (Q_{DAo\text{-}\max})_{target} \end{pmatrix} = \begin{pmatrix} 0 \\ 0 \\ 0 \\ 0 \\ 0 \\ 0 \end{pmatrix}, \tag{2.20}$$

where P_{max} is the maximum (systolic) pressure at the root of the ascending aorta, P_{min} is the minimum (diastolic) pressure at the root of the ascending aorta, (F) represents a flow rate split, (*BC* - brachiocephalic artery, *LCC* - left common carotid artery, *DAo* - descending aorta), and $Q_{DAo\text{-}max}$ is the descending aorta maximum flow rate. The target systolic and diastolic pressures (83.92 mmHg and 49.68 mmHg respectively – determined from the measured time-varying pressure in the ascending aorta), the target flow rate splits and the target descending aorta maximum flow rate are taken from literature data [***CFD Challenge, 2013] (CFD challenge "Predicting Patient-Specific Hemodynamics at Rest and Stress through an Aortic Coarctation"). The flow rate splits of only three outlets are used as objectives, since the fourth one is obtained as difference. The characteristic values of the residuals for pressure, flow rate split and flow rate

objectives were set to 1.0 mmHg, 0.005 and 3 ml respectively, and the tolerance limits for evaluating convergence to 0.1 mmHg, 0.0005, and 0.3 ml respectively.

The nonlinear system in equation (2.20) was solved in two different configurations:

- the configuration in Figure 2.2, whereas structured trees are used as outlet boundary conditions and the hierarchical parameter estimation framework in Figure 2.1 is applied;
- a configuration wherein three-element windkessel models are used as outlet boundary conditions and only the first stage of the parameter estimation framework in Figure 2.1 is applied (step 9 is removed). The proximal resistance of each windkessel model is set equal to the characteristic resistance of the vessel and is maintained constant throughout the parameter estimation procedure:

$$R_c = \frac{1}{\rho \times r_0^2}\sqrt{\frac{2 \times r \times E \times h}{3 \times r_0}}, \tag{2.21}$$

where $E \cdot h/r_0$ is computed as described below.

Since for the supra-aortic branches only the total compliance $C_{SupraAo}$ is used as parameter in (2.20), in both configurations it is distributed to the outlet boundary condition models of the three branches, based on a power law relationship:

$$C_j = \left(C \times r_j^2\right) \Big/ \sum_{j=1}^{n} r_j^2, \tag{2.22}$$

where C_j represents the compliance at each outlet of the multiscale model.

An important aspect of a blood flow computation with compliant walls is the estimation of the mechanical properties of the aortic wall. To compute the wall properties of the aortic segments, i.e. $E \cdot h/r_0$, a method based on wave-speed computation was used [Olufsen et al., 2000], where the wave-speed is related to the properties of the aortic wall by the following expression:

$$c = \sqrt{\frac{2}{3 \times r} \times \frac{E \times h}{r_0}}, \tag{2.23}$$

where c is the wave speed. To estimate the wave speed, the transit-time method [Ibrahim et al., 2020] was used, whereby $c = \Delta x/\Delta t$. Here Δx is the distance (measured along the centerline) between the inlet at the aortic root and the outlet at the descending aorta, and Δt is the time taken by the flow waveform to travel from the inlet to the outlet location. To estimate the wall properties of the supra-aortic vessels, a slightly modified approach was used, under which the wall properties of each supra-aortic segment are computed separately [Itu et al., 2013(a)]. This is done to minimize the wave reflections at the bifurcations. Under this approach, first the reflection coefficient Γ at a bifurcation is computed:

$$\Gamma = \frac{Y_p - \sum_i (Y_d)_i}{Y_p + \sum_i (Y_d)_i}, \tag{2.24}$$

where Y_p (Y_d) is the characteristic admittance of the parent (daughter) vessel. The characteristic admittance is the inverse of the characteristic resistance of a vessel (computed as in (2.21)).

There are three bifurcations, one for each supra-aortic vessel, and the characteristic resistance of each supra-aortic vessel is computed by setting Γ equal to 0:

$$R_{\text{supra-aortic}} = R_{aorta-p} \times R_{aorta-d} / \left(R_{aorta-d} - R_{aorta-p}\right). \tag{2.25}$$

Once the characteristic resistance is known, $E \cdot h / r_0$, is determined as follows:

$$\frac{E \times h}{r_0} = \frac{3 \times R_{supra-aortic} \times \rho^2 \times r_0^4}{2 \times r}. \tag{2.26}$$

Next, the calibration results obtained by applying the hierarchical parameter estimation framework for the configuration which uses structured tree boundary conditions are presented. The objective and parameter values obtained by running steps 6-9 of the parameter estimation framework for the nonlinear system of equations in (2.20) are displayed in Figure 2.3. The iteration at which the value of each objective enters the tolerance window around the target value is marked with a red dotted line (and does not leave it at subsequent iterations). Convergence is reached after 6 iterations for the pressure based objectives and for the flow rate based objective, and after 2-3 iterations for the flow-split based objectives.

Iteration 0 refers to the results obtained by running the computation with the parameter values determined by solving the nonlinear system of equations for the distal vasculature model in Figure 2.2c. The distal vasculature model represents a good approximation for the multiscale model, since all objectives values are within a limit of ±5% of their corresponding target values. Thus, the initial parameter values estimated at step 1 of the algorithm lead to a good initial match between target and actual values of the objectives, which in turn means that the distal vasculature model represents a good approximation for the reduced-order multiscale model. In particular, the computed values of Φ_{LCC}, Φ_{LS}, Φ_{DAo} are within 1% of the target values after solving the nonlinear system of equations for the distal vasculature model. Φ_{LCC}, Φ_{LS}, Φ_{DAo} are less affected when the algorithm switches from the distal vasculature model to the multiscale model than the maximum and minimum pressures and flow rates. This is given by the fact that the former are mainly determined by the resistances whereas the maximum and minimum pressures and the maximum descending aorta flow rate are influenced by both resistances and compliances. In turn, the total resistance of the model is mainly determined by the distal vasculature, whereas the compliance is significantly influenced (increased) by the proximal aorta model.

Finally I note that in order to exactly match the target values, all parameter values need to be adapted considerably. This is determined by two aspects: as noted above, the proximal aorta geometry increases the total compliance of the multiscale model, and the coarctation segment increases the total resistance of the multiscale model.

Further, the computed and the measured time-varying quantities in the ascending and the descending aorta are compared. Figure 2.4 displays a comparison of inlet pressure, and descending aorta outlet pressure and flow rate, as obtained from measurements and with the computational model when using structured trees or three-element windkessel models as outlet boundary conditions. The dicrotic notch in the ascending aorta pressure profile is well preserved in the computational results and, overall, there is a good agreement between the measured and computed quantities, for both types of outlet boundary conditions. The measured minimum and maximum pressure values in the ascending aorta, and the measured maximum flow rate in the descending aorta are exactly matched by the computational results of both configurations since these have been used as objectives in the parameter estimation framework.

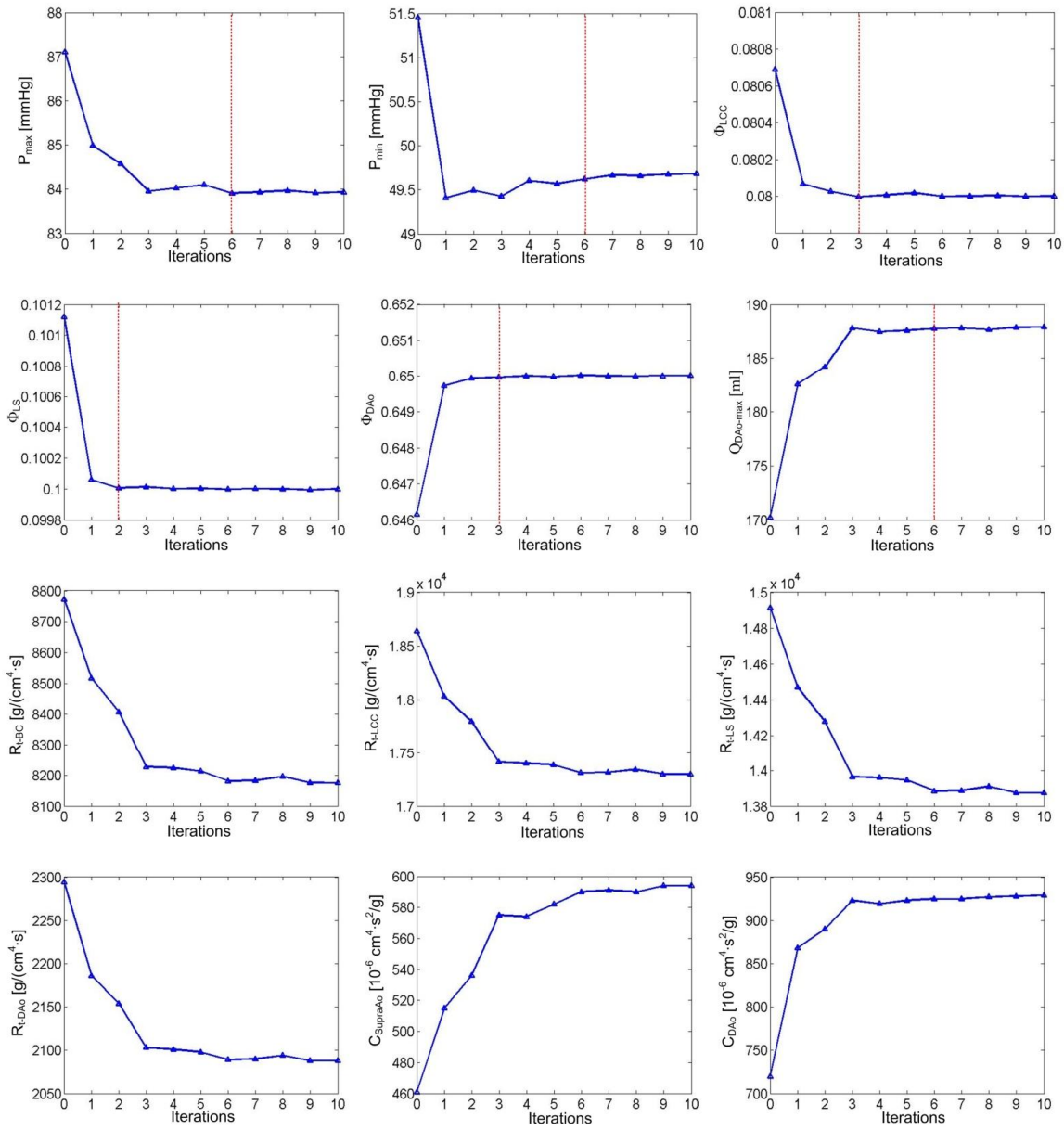

Figure 2.3: Parameter estimation progression for the patient-specific proximal aorta model. The total resistance of each of the three supra-aortic branches, the total resistance of the descending aorta, the sum of the supra-aortic compliances, and the descending aorta compliance were the adapted parameters. The systolic and diastolic pressures in the ascending aorta, the desired mean fractions of flow through the supra-aortic branches and through the descending aorta, and the maximum flow rate through the descending aorta were used as objectives. The dotted red line represents the iteration at which the value of an objective enters the tolerance window around the target value (and does not leave it at any of the subsequent iterations).

To quantitatively compare measured and computed quantities, the average and maximum differences between time-varying measured and computed quantities were determined. These are displayed in Table 2.3 and confirm the visual observations from Figure 2.4: average and maximum differences are relatively small for both computational configurations.

Finally, Table 2.4 displays the average and the peak-to-peak measured and computed trans-coarctation pressure drop values. The results confirm the visual evaluation of the anatomy,

namely that the coarctation is mild: the measured peak-to-peak pressure drop is of only 6.5 mmHg (the clinically employed threshold for identifying functionally significant coarctations is 20 mmHg [Itu et al., 2013(a)]). Both computed pressure drop values match the measured values well, and classify it correctly as being functionally non-significant.

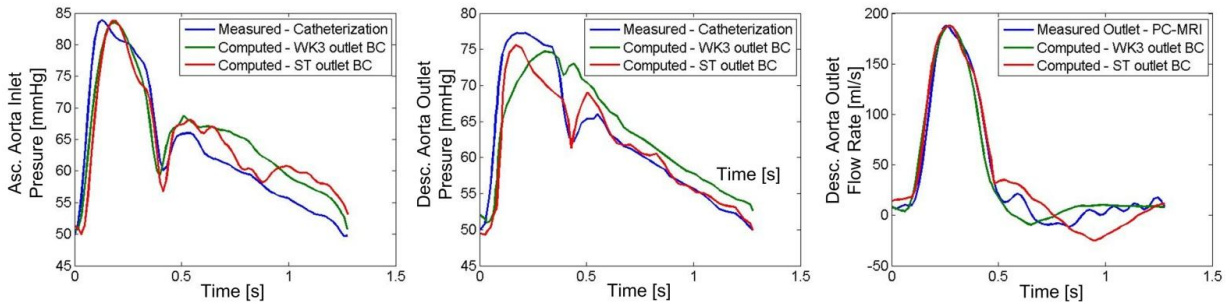

Figure 2.4: Comparison of computed and measured time-varying pressure and flow rate values at the ascending and descending aorta, when using structured trees or three-element windkessel models as outlet boundary conditions of the computational model.

Table 2.3: Average and maximum differences between time-varying measured and computed quantities, obtained for the configurations with structured and three-element windkessel outlet boundary conditions.

Difference	Outlet boundary condition	Asc. Aorta Pressure [mmHg]	Desc. Aorta Pressure [mmHg]	Desc. Aorta Flow Rate [ml/s]
Average	Structured Tree	3.62	2.88	11.45
	Windkessel	3.65	4.39	9.25
Maximum	Structured Tree	9.61	9.35	29.67
	Windkessel	8.38	10.85	30.72

Table 2.4: Comparison of computed and measured average and peak-to-peak trans-coarctation pressure drop.

Configuration	Average ΔP [mmHg]	Peak-to-Peak ΔP [mmHg]
Computed - Windkessel outlet BC	2.01	8.81
Computed - Structured tree outlet BC	1.83	8.17
Measured	1.23	6.50

2.4 DISCUSSION AND CONCLUSIONS

This chapter addresses the important topic of automatically adapting the parameters of structured tree boundary conditions for patient-specific blood flow computations. This is the first time structured tree parameters are adapted so as to simultaneously match pressure and flow measurements. A hierarchical iterative parameter estimation framework has been developed and tested for this purpose: the first stage adapts the overall hemodynamic properties of the structured trees, whereas the second stage adapts the parameters of the structured trees so as to match the hemodynamic properties determined at the first stage.

Calibration of the structured tree parameters is required since the tree is generated from a set of constant scaling parameters (see Table 2.1). A tiered structure could be used alternatively

[Olufsen et al., 2007], but since the use of a non-generic tree (with no fractal structure) would be computationally too demanding and its structure impossible to obtain under patient-specific conditions, parameter calibration is the most suitable approach for matching patient-specific properties of the microvasculature. It is hypothesized that, even if organ specific tree properties were used within a constrained constructive optimization procedure applied for growing optimal trees within patient-specific organ geometries [Karch et al.], parameter calibration would still be required to exactly match desired hemodynamic quantities.

The two most important hemodynamic properties of a vascular tree are the resistance and the compliance. To be able to vary the two quantities over a large range of values, two parameters are adapted for each quantity. A large range of variation is desired to be able to simulate different patient states, e.g. rest, exercise, etc. [Olufsen et al., 2007]. The total resistance values given in Table 2.2 correspond to the rest state. Hence, if an exercise state were to be simulated, the total resistances would be smaller and a higher minimum radius may be required.

The minimum radius at which the structured tree generation is stopped, and the resistance, imposed at all outlets of the structured, are adapted for matching the total resistance of the tree. The constants k_1 and k_3, describing the wall stiffness, are adapted for matching the total compliance of the tree. For both hemodynamic properties, the former of the two parameters is used for coarse adaptation (algorithms 1 and 2). Compared to the recently published work of Cousins et al. [Cousins et al., 2014], a fixed value was used for the length-to-radius ratio, which matches previously reported values [van Bavel et al., 1992], [Zamir et al., 1999], [Nordsletten et al., 2005]. The values of other parameters used for the generation of the structured trees are in agreement with literature data: asymmetry ratio [van Bavel et al., 1992], [Kalsho et al., 2004], and vessel size at bifurcations [van Bavel et al., 1992], [Huo et al., 2012], [Rossitti et al., 1992].

Herein, the original structured tree formulation was employed, introduced by Olufsen [Olufsen, 1998]. However, the parameter estimation framework can be applied in an unchanged form for the recently introduced variations: alternative derivation under periodicity assumption [Cousins et al., 2012], and generalized transient formulation [Cousins et al., 2013].

The geometrical multiscale framework of the aortic model is useful for modeling multiple pathologies. Since this study focuses on the calibration of the structured tree boundary condition, the maximum and minimum pressure in the ascending aorta were used as objectives, as measured during catheterization, thus enhancing the level of personalization in the computational model. No additional pressure-based objectives were formulated for the ascending aorta and for the descending aorta, since the final goal of this methodology is for it to be applied in a non-invasive clinical workflow, during which pressure measurements are not be available for both the ascending and descending aorta. Arm cuff-based pressure measurements can be used, and translated into ascending aorta pressure values [Saouti et al., 2012].

The methodology introduced herein provides the means for automatically calibrating structured tree parameters. This is a prerequisite for future activities which will focus on a rigorous comparison of computational results obtained with multiscale models which use structured tree or windkessel based distal vasculature models.

The study has a series of limitations. The performance of the hierarchical parameter estimation method has been evaluated with a reduced-order multiscale model and not with a full-order multiscale model. However, the framework proposed for the parameterization of structured tree boundary conditions can also be applied, in an unchanged form, for the calibration of full-order multiscale models. Secondly, the inertance, a third important hemodynamic property,

alongside resistance and compliance, has not been considered when adapting the parameters of the structured trees. The inertance effects are particularly important in the large arteries, but can be neglected in the small arteries of the structured trees.

3. Non-invasive Assessment of Patient-specific Aortic Hemodynamics from 4D MRI Data

3.1 INTRODUCTION

For accurate patient-specific computations, the role of physiologically sound boundary conditions (inlet and outlet boundary conditions, and vascular wall properties) is well appreciated in the literature.

Various approaches have been proposed for personalizing the inlet and outlet boundary conditions. The outlet boundary conditions model the effect of the distal vasculature and are typically represented by lumped parameter models. The most widely used lumped parameter model is the three-element Windkessel model [Westerhof et al., 1971].

Various calibration procedures for the outlet boundary conditions have been proposed based on multiple pressure and / or flow measurements, which are typically available in a clinical scenario. A fully automatic optimization-based calibration method for the Windkessel models was suggested [Spilker et al., 2010]. This method was then further refined to both increase its robustness as well as to reduce the number of iterations required for reaching convergence [Itu et al., 2015]. Furthermore, an adjoint-based method for calibrating the Windkessel parameters was proposed [Ismail et al., 2013]. A competitive alternative to the above mentioned optimization based methods is represented by filtering based methods [Bertoglio et al., 2012].

The vascular wall properties determine the arterial distensibility, which is an important factor for the development and assessment of cardiovascular diseases [Mitchell et al., 2010].

Typically, the arterial distensibility is described by the arterial compliance (or the arterial elastance – the inverse of the compliance), which is responsible for important functional aspects of the systemic circulation: larger blood flow rate in the coronary arteries during diastole, reduction of left ventricular afterload (during systole), continuous flow at the level of the capillaries, etc.

Previous studies indicate that arterial compliance changes with age [Avolio et al., 1983] and hypertension [McVeigh et al., 1991].

The arterial wall properties at a certain location in the systemic circulation can be described by the local compliance, typically defined as area compliance, C_A, or by the local pulse wave velocity c. The pulse wave velocity (PWV) is also used as a robust prognostic parameter in preventive cardiovascular therapy [Liberson et al., 2016]. Alternatively, the arterial wall properties can be described globally, for a certain region or for the entire systemic circulation, by the volumetric compliance C_V.

Several approaches have been proposed in the past for non-invasive estimation of arterial wall properties [Stergiopulos et al., 1995]. Many of them rely on the transit time of the flow / pressure wave, i.e. the time that a flow / pressure wave needs to travel the distance between two locations. These methods may have a low accuracy if the distance used for the estimation of the transit time is relatively short, and can only provide an average value of the regional mechanical wall properties for the region of interest. Other methods estimate local vascular wall properties:

- the ACM method [Saouti et al., 2012] estimates the local area compliance as $C_A = \Delta A / \Delta P$, where ΔA is the difference between minimum and maximum cross-sectional area during a heart cycle and ΔP is the pulse pressure;
- the Pulse Pressure Method (PPM) [Stergiopulos et al., 1999] estimates the downstream volumetric compliance from the flow rate waveform and from the pulse pressure;
- the PU-loop method [Khir et al., 2001] estimates the local PWV as $c = \mathrm{d}P / \rho \mathrm{d}U$ during early systole, where $\mathrm{d}P$ is the derivative of the pressure and $\mathrm{d}U$ is the derivative of the blood flow velocity;
- the DU-loop method [Feng et al., 2010] estimates the local PWV as $c = 0.5\ \mathrm{d}U / \mathrm{d}(\ln D)$ during early systole, where $\mathrm{d}U$ is defined as above and D is the diameter;

All these approaches require accurate measurements / estimation of the pressure / velocity / area waveforms, which are not readily available or are susceptible to estimation errors when determined non-invasively.

Furthermore, previously reported patient-specific blood flow computation frameworks typically set the vascular wall properties either based on a best fit to experimental data [Olufsen et al., 2000], or determine a single pulse wave velocity value for the entire anatomical model [Itu et al., 2013(a)], [Florkow et al., 2016].

Herein a parameter estimation framework is proposed for automatically and robustly personalizing aortic hemodynamic computations from 4D Magnetic Resonance Imaging (MRI) data.

The framework is based on a reduced-order multiscale fluid-structure interaction (FSI) blood flow model and personalization procedures. The latter calibrate inlet and outlet boundary conditions, as well as the regional mechanical wall properties, to ensure that the computational results match the patient-specific measurements.

3.2 METHODS

3.2.1 Extraction of 4D anatomical and flow information from medical imaging data

The parameter estimation and computational framework introduced herein is based on anatomical and flow information extracted from 4D flow MRI medical imaging data. A proprietery tool (research prototype, not for diagnostic use) is used to reconstruct and pre-processes the data by applying a series of image correction algorithms such as phase anti-aliasing and motion tracking [Gulsun et al., 2015].

Once the 4D flow data is prepared, the steps displayed in Figure 3.1 are performed sequentially. First, the user initiates a semi-automatic segmentation procedure by selecting a set of seed points, starting at the inlet of the ascending aorta and ending at the outlet of the descending aorta. Typically two to four seed points are required for a reliable initialization, and a preliminary, rough segmentation is performed based on a clustering approach that groups voxels in the 4D flow data into static tissue, air/lung and blood. Next, the centerline of the aorta is automatically extracted from it. Once the user verified the proposed centerline, the segmentation is automatically refined, and the refined geometry may be manually corrected if deemed appropriate. As a result, the vessel lumen anatomical model and its centerline are obtained. Subsequently, a large number (typically 50) of cross-sectional planes (analysis planes) along the aorta are automatically generated. For each analysis plane, the flow data is systematically analysed to determine the time-varying cross-sectional areas and the time-varying flow rates along the aorta. Anatomical and flow information is thus extracted only for the aorta (ascending aorta, aortic arch and descending aorta), and not for the supra-aortic branches.

In addition to flow and geometrical data, non-invasive, cuff-based pressure measurements obtained from the left arm are also used.

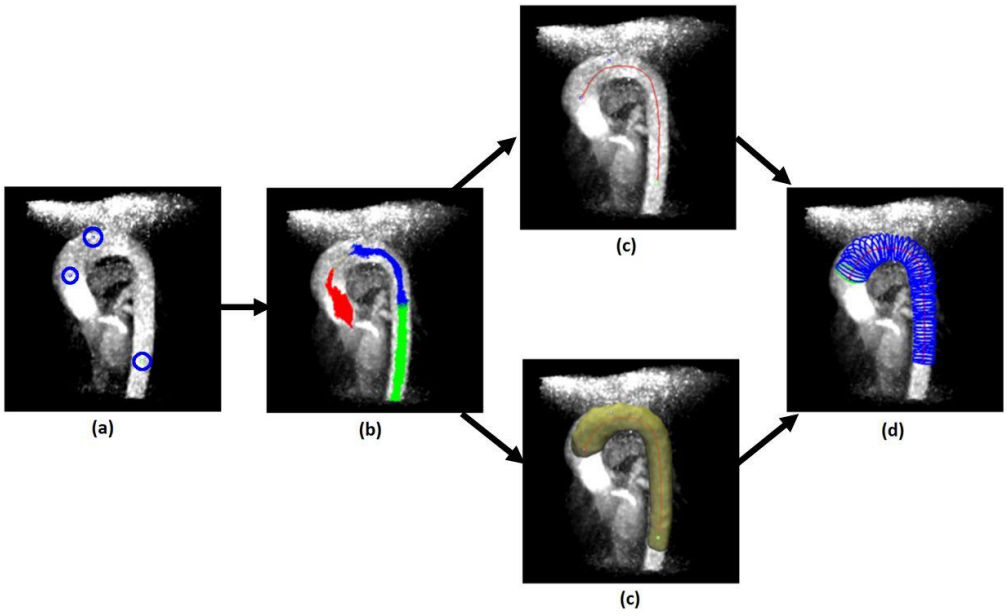

Figure 3.1: Extraction of 4D anatomical and flow information from 4D MRI data: (a) Manual selection of seed points; (b) Automatic segmentation; (c) Vessel lumen centerline and anatomical model; (d) Automatic definition of analysis planes at which the time-varying flow rates and cross-sectional areas are determined. Analysis planes are displaced appropriately as the aortic geometry deforms over the course of the cardiac cycle.

3.2.2 Reduced-order multiscale fluid-structure interaction blood flow model

The parameter estimation framework for personalizing aortic hemodynamic computations employs a reduced-order multiscale fluid-structure interaction blood flow model, which is based on a quasi one-dimensional and a lumped parameter model (zero-dimensional model) [Itu et al., 2013(a)].

The one-dimensional blood flow model is derived from the three-dimensional Navier-Stokes equations based on a series of simplifying assumptions. The resulting governing equations ensure mass and momentum conservation [Reymond et al., 2011]. A state equation, which relates the pressure inside the vessel to the cross-sectional area, is used to close the system of equations. The vessel wall is modelled as an elastic material:

$$p(x,t) = \Upsilon_{el}(A) + p_0 = \frac{4}{3}\frac{Eh}{r_0}(x)\left(1 - \sqrt{\frac{A_0(x)}{A(x,t)}}\right) + p_0, \tag{3.1}$$

where x denotes the axial location, t denotes the time, $A(x,t)$ is the cross-sectional area, $p(x,t)$ the pressure, E is the Young modulus, h is the wall thickness, r_0 is the initial radius corresponding to the initial pressure p_0, and A_0 is the initial cross-sectional area. At each bifurcation, the continuity of flow and total pressure is imposed.

Time-varying flow rate profiles are used as inlet boundary condition, while three-element Windkessel models are coupled at the outlets of the one-dimensional model.

3.2.3 Parameter estimation framework

Figure 3.2 displays an overview of the proposed parameter estimation framework for personalizing the aortic hemodynamic computations. The reduced-order multiscale FSI blood flow model is first initialized and two independent calibration procedures are sequentially and iteratively employed for automatically and robustly personalizing the aortic hemodynamic computations:

- Personalization of the Windkessel parameters in the outlet boundary conditions of the multiscale circulation model;
- Personalization of the regional mechanical wall properties of the aorta.

The two calibration procedures are run until the convergence criteria are met for both of them simultaneously. Finally, the results of the hemodynamic computations are post-processed to determine clinically relevant characteristics.

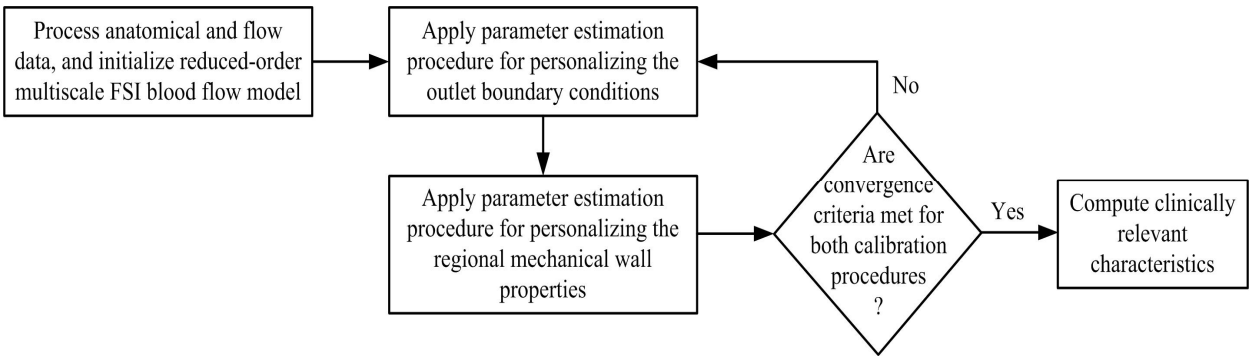

Figure 3.2: Flowchart of the proposed parameter estimation framework.

3.2.3.1 Initialization of the reduced-order multiscale fluid-structure interaction blood flow model

Figure 3.3a displays the multiscale fluid-structure interaction blood flow model for the aorta and the supra-aortic branches. The aorta is divided into multiple segments for which the regional mechanical properties are estimated (these are numbered from 1 to 7 in Figure 3.3a, but the actual number of segments can vary and depends on the length of the ascending and descending aorta).

The initialization of the blood flow model consists in the following five steps, which are described in detail below:

- Defining the bifurcation locations of the supra-aortic branches;
- Defining the average flow rate values for the ascending and descending aorta;
- Defining the one-dimensional segments and their geometry;
- Defining the inlet boundary condition and the initial parameter values at the outlet boundary condition;
- Defining the initial regional mechanical wall properties.

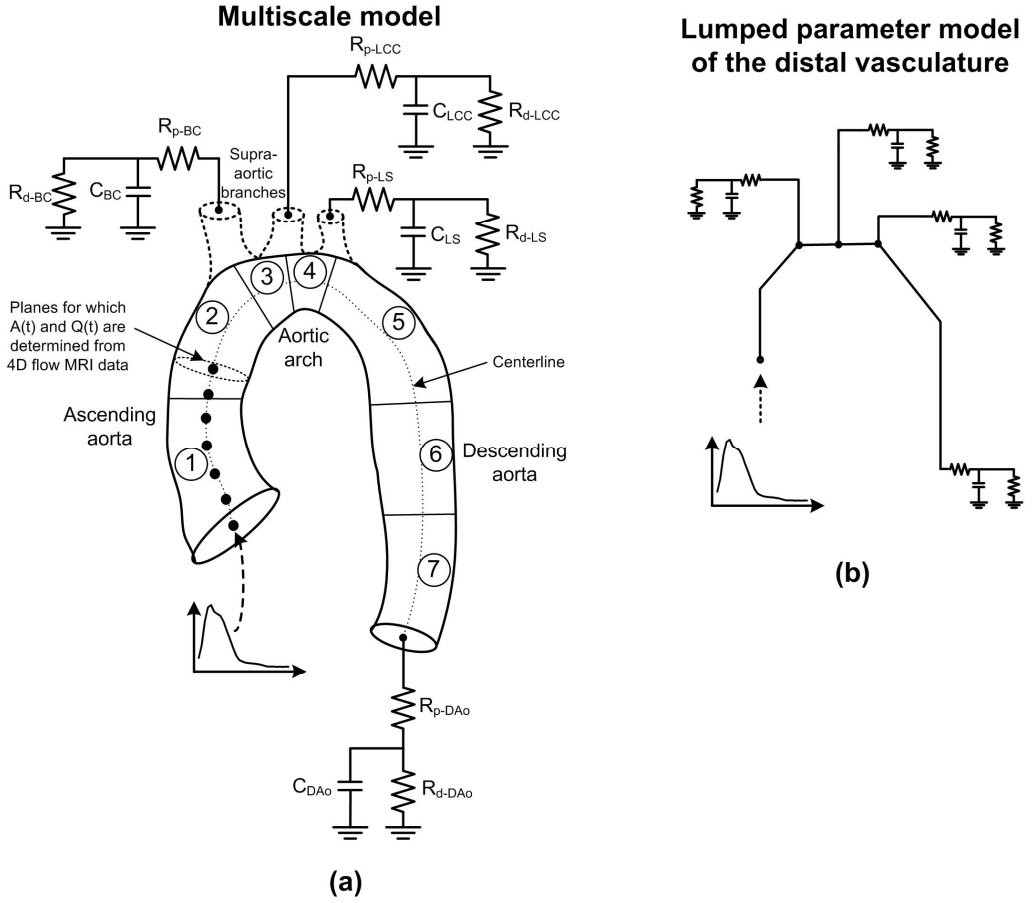

Figure 3.3: (a) Multiscale fluid-structure interaction blood flow model; (b) Lumped parameter model of the distal vasculature used for finding an initial solution for the personalization of the outlet boundary conditions.

As was mentioned in section 2.1, anatomical and flow rate information is only available for the aorta. However, since the supra-aortic branches draw away from the aorta a significant volume of blood (30-50%), to run accurate hemodynamic computations the anatomical model is

augnmented with supra-aortic branches. To this end, the bifurcation point of the first supra-aortic branch (the brachiocephalic artery) is determined by navigating downstream, starting from the ascending aorta inlet, through the centerline locations until a cross-sectional plane is found, for which the average flow rate decreases below 90% of the average flow rate at the upstream centerline locations, and no downstream cross-sectional plane with a larger flow rate exists. Similarly, the bifurcation point of the third supra-aortic branch (the left subclavian artery) is determined by navigating upstream, starting from the descending aorta outlet, through the centerline locations until a cross-sectional plane is found for which the average flow rate is larger than 110% of the average flow rate at the downstream centerline locations, and no upstream cross-sectional plane with a lower flow rate exists. Finally, the bifurcation point of the second supra-aortic branch (the left common carotid artery) is set midway between the other two supra-aortic branches.

Next, average flow rate values are estimated for the ascending and the descending aorta. Due to measurement noise, the average flow rate varies slightly between consecutive cross-sectional locations. A linear least squares fit based algorithm is employed, which is used to filter out locations with very large or very low average flow rate values. Based on the remaining locations, a final average flow rate value is determined for the ascending and the descending aorta.

In the following, the one-dimensional segments and their geometry are defined. First the number of segments is set for each branch: two segments for the aortic arch, and multiple segments for the ascending (at least two) and descending aorta (at least three). Spatially varying cross-sectional area values are defined for each segment to obtain a geometry which is reliably reflecting the actual three-dimensional geometry. The initial cross-sectional area values are based on the end-diastolic phase.

Population-average geometric properties [Reymond et al., 2011], which are scaled based on the patient-specific aorta size, are applied to define the one-dimensional segments corresponding to the supra-aortic branches (a fixed length of 2 cm is used for each supra-aortic branch).

Subsequently, the inlet boundary condition is defined: the flow rate profile measured at the first analysis plane is scaled so as to match the average ascending aorta flow rate value estimated as described above. Next, three initial parameter values need to be specified at each outlet. First, the average pressure at the inlet of the left subclavian artery is computed, following an approach validated in [Saouti et al., 2012]. The brachial systolic pressure $P_{b\text{-}s}$ and the brachial diastolic pressure $P_{b\text{-}d}$ are used as input data. The diastolic pressure at the inlet of the left subclavian artery is set equal to $P_{b\text{-}d}$, while the systolic pressure is computed from:

$$P_{LSA\text{-}s} = 0.83P_{b\text{-}s} + 0.15P_{b\text{-}d}\,. \tag{3.2}$$

Next, the mean arterial pressure at the inlet of the left subclavian artery is computed using a form factor of 0.4:

$$\overline{P}_{LSA} = 0.4P_{LSA\text{-}s} + 0.6P_{LSA\text{-}d}\,. \tag{3.3}$$

Since the variation of the average arterial pressure in the aorta is typically small, $\overline{P}_{LSA}$ is used for determining the initial total resistance at each outlet as ratio between average pressure and average flow rate:

$$R_t = \overline{P}/\overline{Q}\,. \tag{3.4}$$

To determine the average flow rate for each supra-aortic branch the total supra-aortic average flow rate, $Q_{supra\text{-}aortic}$, is computed as difference between the average flow rates in the ascending and the descending aorta. This flow is then distributed to the branching vessels proportionally to the square of the radius. To minimize reflections, the proximal resistance of each Windkessel model is set equal to the characteristic resistance of the corresponding outlet segment, while the distal resistance is computed as difference between total and proximal resistance.

For the estimation of compliance values, first a population average compliance value (C_{tot}) is considered [Low et al., 2012], which is then distributed to the four outlets proportionally to the square of the radius.

To initialize the regional mechanical wall properties first the arterial wall properties at the bifurcation of the left subclavian artery are determined. Eq. (3.1) is rewritten, based on $P_{LSA\text{-}s}$ and $P_{LSA\text{-}d}$ as:

$$P_{LSA\text{-}s} = b\left(1 - \sqrt{\frac{A_{LSA\text{-}d}}{A_{LSA\text{-}s}}}\right) + P_{LSA\text{-}d}\,, \tag{3.5}$$

where $A_{LSA\text{-}s}$ and $A_{LSA\text{-}d}$ are the maximum (systolic) and minimum (diastolic) cross-sectional area values, and β represents the wall stiffness. Hence:

$$b = \frac{4}{3}\frac{Eh}{r_0} = \left(P_{LSA\text{-}s} - P_{LSA\text{-}d}\right) \Big/ \left(1 - \sqrt{\frac{A_{LSA\text{-}d}}{A_{LSA\text{-}s}}}\right). \tag{3.6}$$

This value is used to initialize the stiffness for the entire aorta. To estimate the wall properties of the supra-aortic vessels, a slightly modified approach is used, under which the wall properties of each supra-aortic segment are computed separately. This is done to minimize the wave reflections at the bifurcations [Itu et al., 2013(a)]. The initial pressure in the entire domain is set equal to $P_{b\text{-}d}$.

3.2.3.2 Parameter estimation procedure for personalizing outlet boundary conditions

The objective of the parameter estimation procedure described in this section is to adapt the parameters of the Windkessel models coupled to the outlets of the one-dimensional model, under the constraint that the blood flow solutions should: i) maintain the same average flow-split at each outlet as determined with the procedure described in section 3.2.3.1, and ii) replicate the measured systolic and diastolic pressure at the inlet of the left subclavian artery. Out of the four flow-split values (three supra-aortic branches and the descending aorta) only three are used as objectives, since the fourth one is obtained automatically as difference.

The parameter estimation problem is formulated as a solution to a system of nonlinear equations, with each equation representing the residual error between the computed and measured quantity of interest.

To determine the values of all the residuals ($\boldsymbol{f}(\boldsymbol{x}_i)$), a computation with the parameter values $\boldsymbol{x}_i$ is required. Since the absolute values of the adapted parameters and of the residuals generally differ by orders of magnitude, for the calibration method both the parameter and the objective residuals have been scaled using typical values.

The parameters to be estimated are the total resistances of the three supra-aortic vessels and of the descending aorta, and the total compliance. The following system of nonlinear equations is numerically solved to obtain the optimum value of each parameter:

$$\mathbf{f}\begin{pmatrix} R_{t-BC} \\ R_{t-LCC} \\ R_{t-LS} \\ R_{t-DAo} \\ C \end{pmatrix} = \begin{pmatrix} (P_{\max-LSA})_{comp} - (P_{\max-LSA})_{ref} \\ (P_{\min-LSA})_{comp} - (P_{\min-LSA})_{ref} \\ (F_{LCC})_{comp} - (F_{LCC})_{ref} \\ (F_{LS})_{comp} - (F_{LS})_{ref} \\ (F_{DAo})_{comp} - (F_{DAo})_{ref} \end{pmatrix} = \begin{pmatrix} 0 \\ 0 \\ 0 \\ 0 \\ 0 \end{pmatrix}, \tag{3.7}$$

where $P_{max-LSA}$ is the maximum (systolic) pressure, $P_{min-LSA}$ is the minimum (diastolic) pressure, both at the inlet of the left subclavian artery, (F). represents a flow rate split, while $(\cdot)_{comp}$ refers to a value computed using the lumped parameter/multiscale model, and $(\cdot)_{ref}$ refers to the reference value. Index *LCC* refers to the left common carotid artery, *LS* to the left subclavian artery, and *DAo* to the descending aorta.

The typical values of the objectives f_i^{typ} are set equal to 1mmHg for the pressure based objectives and to Φ/100 for the flow rate split based objectives.

The nonlinear system of equations is first solved for a lumped parameter model, composed of the Windkessel models used in the multiscale model (Figure3.3b). The initial solution $\boldsymbol{x}_0$ is determined using the steps described in the previous section and a dogleg trust region algorithm is applied to iteratively determine the solution of the nonlinear system of equations. The solution determined for the lumped parameter model is then adapted as described in [Ismail et al., 2013], to compensate for the hemodynamic properties (resistance and compliance) of the multiscale model that are not taken into account in the lumped parameter model. As a result, the risk of a failure in finding a solution to the nonlinear system of equations is reduced, and, importantly, the number of calibration iterations required to reach the final solution is decreased.

Next, eq. (3.7) is solved for the multiscale reduced-order blood flow model. Each computation, with a given set of parameter values, is run until the L_2 norms of the normalized differences between the pressure and flow rate profiles at the current and the previous cardiac cycle are smaller than 10^{-5}. A quasi-Newton method is employed at this stage, where at each iteration the Jacobian is only updated and not recomputed, to ensure short computation times. If all objective residuals are smaller than the tolerance limit (taken here equal to f_i^{typ}), the calibration method is terminated.

3.2.3.3 Parameter estimation procedure for personalizing the regional mechanical wall properties

The objective of the parameter estimation procedure described in this section is to adapt the local wall stiffness along the aorta so as to obtain a good match between the measured and the computed cross-sectional area variation at the analysis planes. The parameter estimation procedure is based on a non-linear least squares method, which minimizes the following cost function:

$$f(\mathbf{x}) = \frac{1}{2}\sum_{j=1}^{m} r_j^2(\mathbf{x}), \tag{3.8}$$

where *m* is the total number of measurements, *j* refers to a specific measurement location along the aorta, and $r_j(\mathbf{x})$ are the residuals computed as difference between the measured and the computed quantities:

$$r_j(\mathbf{x}) = DA_j^{ref} - DA_j^{comp}, \tag{3.9}$$

where ΔA_j^{ref} is the measured maximum variation in the cross-sectional area during a heart cycle at location *j*, and ΔA_j^{comp} is the computed maximum variation in the cross-sectional area during a heart cycle at location *j*.

The parameter vector **x** contains the wall stiffness at the start and end of each one-dimensional segment in the computational model (a linearly varying stiffness is imposed between the inlet and outlet of each one-dimensional segment):

$$\mathbf{x} = [b_{1\text{- start}} \;\; b_{1\text{- end}} \;\; b_{2\text{- start}} \;\; b_{2\text{- end}} \;\; ...]^{\mathrm{T}}, \tag{3.10}$$

The cost function is minimized using a quasi Gauss-Newton method (a modified Newton's method with line search). Thus, first a search direction p_k^{GN} is determined, and a step length α_k to satisfy the Armijo and Wolfe conditions is chosen [Nocedal et al., 2006]. At each iteration, once the wall properties of the aorta have been updated, the wall properties of the supra-aortic branches are modified to minimize the wave reflections at the bifurcations (see section 3.2.3.1). Similar to the setup described in the previous section, the Jacobian is only computed once, and then updated at each further iteration. Once the cost function converges (its variation from one iteration to the next becomes smaller than 1%), the calibration procedure is terminated.

As depicted in Figure 3.2, once the calibration procedure for determining the regional mechanical wall properties has converged, the convergence criteria of the calibration procedure for determining the outlet boundary conditions are verified. If these are not satisfied, the two parameter estimation procedures are rerun. The convergence criteria of the first calibration procedure may no longer be satisfied once the second parameter estimation procedure has been applied, since a change in the wall properties generally induces a change in the pressure and flow rate values.

3.2.3.4 Computation of clinically relevant characteristics

Once the calibration procedures of the parameter estimation framework have converged, the computational results are post-processed to determine a series of clinically relevant characteristics:

1. The local pulse wave velocity:

$$c(x) = \sqrt{\frac{b(x)}{2r}}, \tag{3.11}$$

2. The local area compliance:
   a. Using the wall stiffness:

$$C_A(x) = \frac{2A(x)}{b(x)}, \tag{3.12}$$

   where A(x) is the average value of the cross-sectional area at location *x*.
   b. Using the ACM method:

$$C_{A\text{- ACM}}(x) = \frac{\Delta A(x)}{PP(x)}, \tag{3.13}$$

   where $\Delta A(x)$ is the maximum variation of the cross-sectional at location *x*, and PP(x) is the pulse pressure at location *x*, determined from the hemodynamic computations.
3. The downstream volumetric compliance:

$$C_V(x) = PPM\left(q(x,t), PP(x)\right), \tag{3.14}$$

where *PPM* refers to the pulse pressure method [Stergiopulos et al., 1994] which uses as input the time-varying flow rate at location *x* and the pulse pressure at location *x*, as determined from the hemodynamic computations.

3.3 RESULTS

To evaluate the performance of the proposed parameter estimation framework, results are presented for 15 datasets acquired from patients with aortic valve disease (60% male) enrolled in the "Cardioproof" project [***CardioProof, 2017]. The patients' age ranged from 9 to 69 years (mean: 30.9 ± 21.8 years). The study complied with the Declaration of Helsinki for investigation in human beings. The study protocol was approved by the local ethics committee and each patient signed an informed consent form before the enrolment in the study.

Blood was modelled as an incompressible Newtonian fluid with a density of 1.050 g/cm3 and a dynamic viscosity of 0.040 dynes/(cm^2·s). The grid size for the numerical solution of the one-dimensional model was 0.05cm, while the time-step (limited by the CFL-condition) was set equal to 2.5e-5s.

3.3.1 Personalization of the hemodynamics computations

The calibration procedures converged successfully for all 15 datasets, with an average execution time of 6.2 ± 1.2 minutes on an off-the-shelf computer (Intel i7 processor). Table 3.1 displays the calibration results: the objective and parameter values of the outlet boundary conditions calibration procedure (reference objective values are displayed in parenthesis), and, for the regional mechanical wall properties calibration procedure the initial and final value of the cost function (eq. (3.8)) are displayed alongside the estimated wall stiffness. The number of calibration iterations is displayed both at global level (iterations of the loop in Figure 3.2), and separately for each calibration procedure (as a sum of all calibration iterations during the different global iterations). Only one or two global iterations were required to reach convergence.

The five objectives defined in (3.7) are matched closely for each dataset and the total number of calibration iterations for personalizing the outlet boundary conditions was at most three (1.27 ± 0.96). A very good match between the reference and the computed values of the objectives was observed (mean relative difference < 0.5%).

The total number of calibration iterations for personalizing the regional mechanical wall properties was 7.07 ± 1.44; the value of the cost function was decreased from 2.95 ± 1.90 to 0.23 ± 0.37. The mean wall stiffness for the entire cohort was $0.93 \cdot 10^3 \pm 0.37 \cdot 10^3$ mmHg. This value is similar to the mean wall stiffness of large arteries described previously in literature, obtained by performing a best fit to experimental data ($0.85 \cdot 10^3$ mmHg) [Olufsen et al., 2000].

Next, Figure 3.4 presents as an example the calibration results obtained by personalizing the boundary conditions of patient dataset 15: both objective and parameter values, obtained by running the parameter estimation procedure described in section 3.2.3.2, are displayed (the dotted red lines represent the reference values of the objectives).

Two global iterations were required to reach final convergence, and during each global iteration, one local iteration was required to match the objectives related to the outlet boundary conditions (3.7).

Table 3.1: Calibration results obtained by applying the parameter estimation framework for personalizing the hemodynamic computations of the 15 datasets included in the study (SSD = Sum of Squared Difference; SD = Standard deviation)

Pat. Set	Calibration procedure for personalizing the outlet boundary conditions											Calibration procedure for personalizing the regional mechanical wall properties					#iter. global
	$P_{max\text{-}LSA}$ [mmHg]	$P_{min\text{-}LSA}$ [mmHg]	Φ_{LCC}	Φ_{LS}	Φ_{DAo}	$R_{t\text{-}BC}$ [10^3 g/(cm^{4}s)]	$R_{t\text{-}LCC}$ [10^3 g/(cm^{4}s)]	$R_{t\text{-}LS}$ [10^3 g/(cm^{4}s)]	$R_{t\text{-}DAo}$ [10^3 g/(cm^{4}s)]	C [10^{-6} cm^{4}s^2/g]	#iter. outlet BC	Init. val. SSD	Final val. SSD	Mean (β) [10^3 mmHg]	SD (β) [10^3 mmHg]	#iter. wall prop.	
1	103.54 (103.24)	62.76 (63.00)	0.1151 (0.1158)	0.0941 (0.0938)	0.5641 (0.5635)	5.914	11.591	14.31	2.382	1.583	0	2.2	0.14	1.55	0.84	7	1
2	117.21 (117.28)	57.00 (57.00)	0.0858 (0.0858)	0.0695 (0.0695)	0.6767 (0.6767)	6.637	13.009	16.061	1.59	1.346	2	7.67	1.53	1.02	0.44	5	2
3	104.18 (104.37)	65.13 (65.00)	0.1080 (0.1081)	0.0874 (0.0876)	0.5930 (0.5924)	4.706	9.225	11.387	1.68	1.144	2	3.26	0.14	0.6	0.26	8	2
4	115.38 (115.08)	70.37 (70.00)	0.0559 (0.0561)	0.0453 (0.0454)	0.7892 (0.7886)	19.638	38.491	47.519	2.721	0.434	1	0.21	0.02	0.94	0.28	6	1
5	78.81 (78.50)	53.16 (53.00)	0.1178 (0.1179)	0.0954 (0.0955)	0.5559 (0.5556)	6.598	12.896	15.9	2.701	1.213	2	1.55	0.04	0.43	0.18	10	2
6	85.31 (85.21)	59.17 (59.00)	0.1197 (0.1195)	0.0969 (0.0968)	0.5487 (0.5493)	5.911	11.537	14.245	2.528	0.868	2	3.72	0.2	0.4	0.28	8	2
7	115.81 (115.31)	66.82 (66.00)	0.0686 (0.0684)	0.0553 (0.0554)	0.7429 (0.7421)	8.67	16.974	20.91	1.56	1.293	1	3.01	0.16	0.98	0.3	6	1
8	131.79 (131.28)	95.37 (95.00)	0.0729 (0.0730)	0.0591 (0.0591)	0.7250 (0.7248)	14.489	28.397	35.061	2.846	1.217	1	1.11	0.08	1.32	0.42	7	2
9	113.43 (114.01)	84.87 (85.00)	0.0826 (0.0826)	0.0669 (0.0669)	0.6886 (0.6885)	8.627	16.91	20.876	2.029	1.543	0	0.67	0.1	1.68	0.81	7	1
10	81.91 (82.35)	50.40 (51.00)	0.1103 (0.1097)	0.0888 (0.0889)	0.5843 (0.5863)	4.628	9.071	11.199	1.698	1.543	0	3.52	0.07	0.61	0.22	6	1
11	102.70 (102.94)	61.12 (61.00)	0.0650 (0.0651)	0.0526 (0.0527)	0.7550 (0.7548)	10.551	20.679	25.53	1.79	1.369	2	4.46	0.24	0.78	0.3	6	2
12	117.31 (117.14)	45.11 (45.00)	0.0252 (0.0251)	0.0204 (0.0203)	0.9050 (0.9055)	29.085	56.993	70.371	1.555	1.093	3	4.12	0.4	0.92	0.35	7	2
13	113.69 (114.10)	68.45 (69.00)	0.0825 (0.0817)	0.0668 (0.0662)	0.6890 (0.6919)	6.055	11.868	14.652	1.402	1.353	0	0.9	0.06	0.96	0.23	7	1
14	101.06 (100.45)	60.56 (61.00)	0.0670 (0.0670)	0.0542 (0.0543)	0.7475 (0.7473)	7.971	15.621	19.285	1.381	1.252	1	3.85	0.17	0.88	0.37	10	2
15	107.32 (107.18)	44.78 (45.00)	0.1112 (0.1112)	0.0901 (0.0901)	0.5808 (0.5808)	3.619	7.015	8.699	1.345	1.25	2	2.53	0.11	0.85	0.21	6	2

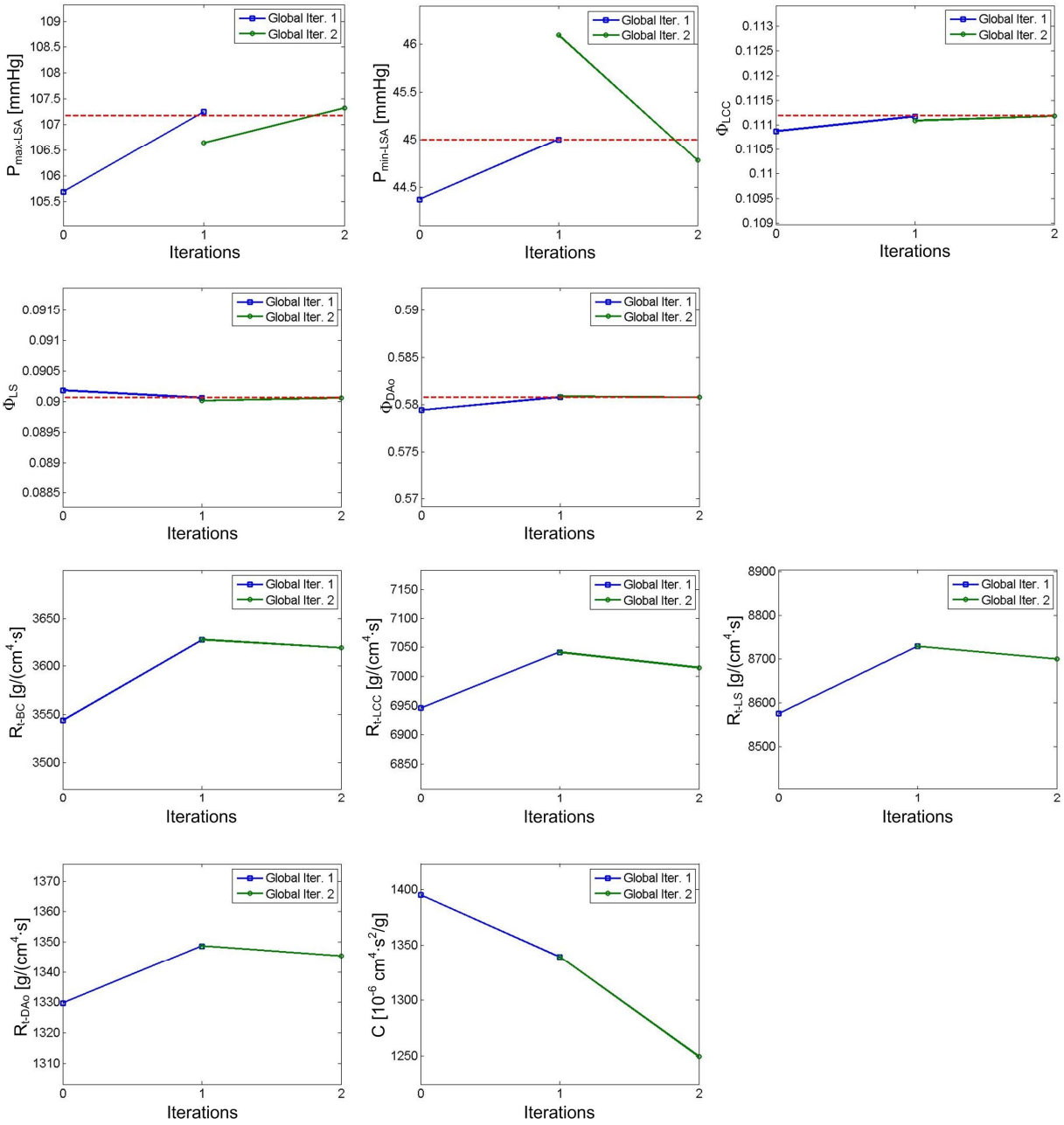

Figure 3.4: Parameter estimation progression for the calibration of the outlet boundary conditions for patient dataset 15. The dashed red lines represent the reference values of the objectives.

Iteration 0 refers to the results obtained by running the computation with the parameter values determined by solving the nonlinear system of equations for the lumped parameter model, and by applying the algorithms for compensating for the hemodynamic properties (resistance and compliance) of the multiscale model. These initial parameter values lead to a good initial match between target and actual values of the objective. In particular, the computed values of Φ_{LCC}, Φ_{LS}, and Φ_{DAo} are within 1% of their target values. Φ_{LCC}, Φ_{LS}, and Φ_{DAo} are less affected when the algorithm switches from the lumped parameter model to the multiscale model than the maximum and minimum pressures. This is due to the fact that the former are mainly determined by the resistances whereas the maximum and minimum pressures are influenced by both resistances and compliances. In turn, the total resistance of the model is mainly determined by

the distal vasculature, whereas the compliance is significantly influenced (increased) by the proximal aorta model.

The objective values at the end of the first global iterations are different from the objective values at the start of the second global iteration. This is due to the fact that the regional mechanical wall properties are calibrated in between, thus also affecting the objectives related to the outlet boundary conditions, and leading to the requirement of running a second global iteration. The parameter values on the other hand are the same at the end of the first global iteration and at the start of the second global iteration.

Next, Figure 3.5 presents the calibration results obtained by personalizing the regional mechanical wall properties of patient dataset 15: both objective and parameter values, obtained by running the parameter estimation procedure described in section 3.2.3.3, are displayed. Four and two local iterations were required during the first and second global iteration respectively.

The cost function value at the end of the first global iterations is slightly different from the value at the start of the second global iteration, because the parameters of the outlet boundary conditions are calibrated in between. Initially the wall stiffness is identical at all locations (as determined during the initialization of the multiscale model (3.6)), but, as the calibration procedure progresses, the wall stiffness of each segment is personalized so as to match the measured cross-sectional area variation.

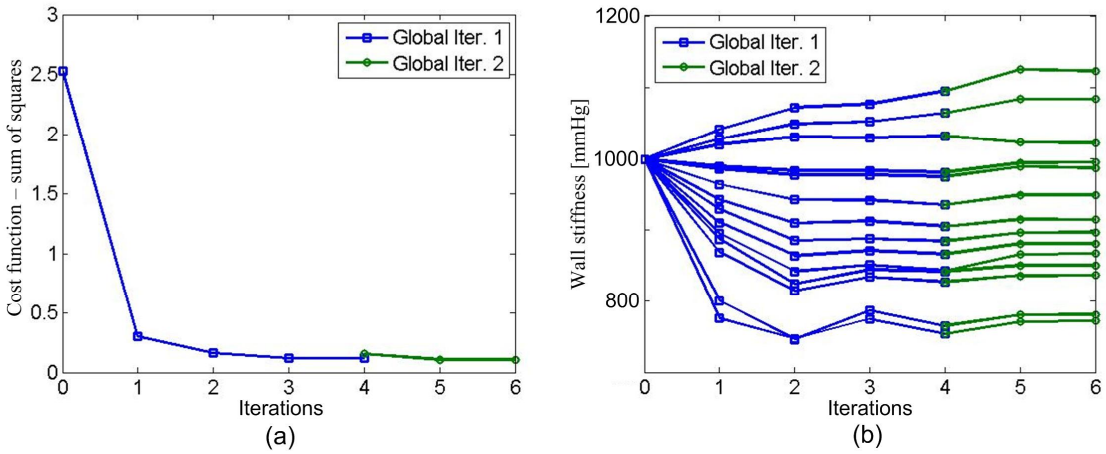

Figure 3.5: Parameter estimation progression for the calibration of the regional mechanical wall properties for patient dataset 15: (a) cost function; (b) wall stiffness, one curve per each regional parameter.

Figure 3.6a displays a comparison of measured (4D MRI) and computed minimum and maximum cross-sectional areas along the centerline of the aorta for patient dataset 15: the values match closely, indicating that the parameter estimation procedure calibrating the wall properties is able to provide a reliable personalization of the arterial wall stiffness. The small differences that can be observed are partially due to the approximation of the three-dimensional geometry through the one-dimensional model. Furthermore, Figure 3.6b and Figure 3.6c display a comparison of the computed and measured time-varying cross-sectional areas at one ascending and one descending aorta location. Importantly, not only the absolute values, but also the timing of the time-varying profiles match closely, confirming that the wave propagation phenomena are captured correctly by the personalized hemodynamic model.

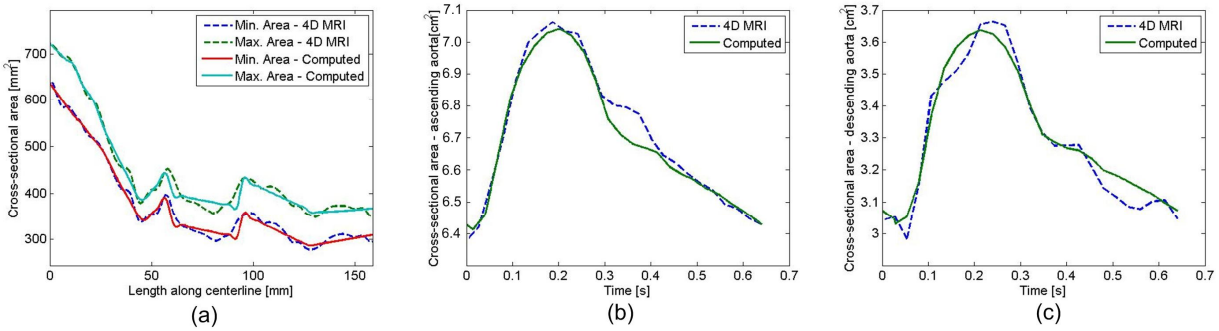

Figure 3.6: (a) Comparison of computed and measured (4D MRI) minimum and maximum cross-sectional area along the centerline of the aorta; (b) Comparison of computed and measured (4D MRI) time-varying cross-sectional area at an ascending aorta location; (c) Comparison of computed and measured (4D MRI) time-varying cross-sectional area at a descending aorta location (all for patient dataset 15).

3.3.2 Regional mechanical wall properties

Table 3.2 displays the quantities of interest related to the regional mechanical wall properties of the 15 patient datasets included in the study, computed as described in section 3.2.3.4. Alongside the PWV determined from (3.11) PWV estimates determined with the transit time method [Ibrahim et al., 2010]: $c = \Delta x / \Delta t$ are included, where Δx is the length along the centerline of the aorta and Δt is the time required for the flow rate wave to travel along this distance. Since Δt is typically very small the aorta was divided into only two regions and the transit time based PWV was estimated separately for these two regions. The first region contains the ascending aorta and the aortic arch, while the second region contains the descending aorta. The time Δt is computed as the interval between the onset (foot) of the flow curves at the start and end of a region. The location of the onset (foot) is determined by the intersection point of the upslope curve and the minimum flow rate. The upslope curve is approximated by the line connecting the points at 30% and 70% of the maximum flow rate at the particular location.

As can be observed in Table 3.2 the mean PWV estimated using (3.11) lies typically in between the two values estimated with the transit time method. Due to the small values of Δt, the transit time method is very sensitive to measurement errors and noise. As an example, Figure 3.7 displays a comparison of the local PWV and the transit time based PWV for patient dataset 15. The local PWV is indeed a bit larger in region 1 than in region 2, but the transit time method overestimates its value in the first region, and underestimates it in the second region.

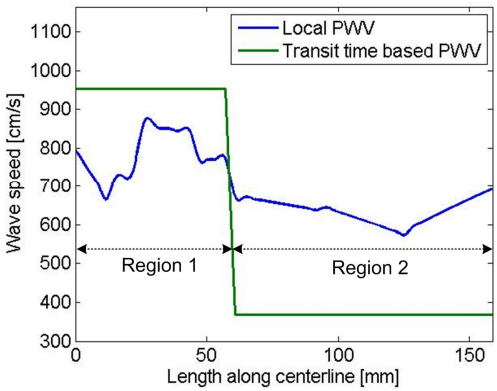

Figure 3.7: Comparison of local pulse wave velocity determined using the herein proposed framework and pulse wave velocity determined using the transit time method for patient dataset 15.

Table 3.2: Quantities of interest related to the regional mechanical wall properties of the 15 patient datasets included in the study: PWV (as determined from (11) and with the transit time method for two distinct aortic regions), local area compliance (as determined from (12) and (13)) and the ascending and descending aorta downstream volumetric compliance (as determined from (14)).

Patient dataset	Mean PWV [cm/s]	St. dev. PWV [cm/s]	Min. PWV [cm/s]	Max. PWV [cm/s]	PWV TT – region 1 [cm/s]	PWV TT – region 2 [cm/s]	Mean C_A [10^{-3} cm^2/ mmHg]	St. dev. C_A [10^{-3} cm^2/ mmHg]	Mean $C_{A\text{-}ACM}$ [10^{-3} cm^2/ mmHg]	St. dev. $C_{A\ ACM}$ [10^{-3} cm^2/ mmHg]	$C_{V\text{-}AAo}$ [10^{-6} cm^4s^2/g]	$C_{V\text{-}DAo}$ [10^{-6} cm^4s^2/g]
1	965.92	224.05	584.56	1339.71	591.86	1321.51	8.359	4.852	8.562	5.221	1078.76	807.33
2	742.63	134.12	546.82	1084.31	368.4	891.4	12.663	4.074	12.979	5.591	1218.18	890.98
3	559.35	91.94	456.41	815.15	399.82	701.02	10.614	2.416	11.079	2.859	878.99	699.87
4	761.63	82.59	627.55	995.39	902.17	453.78	6.053	1.413	6.205	1.54	397.89	269.03
5	485.65	78.61	331.72	693.8	530.67	364.36	13.352	3.509	13.848	3.897	793.76	484.85
6	461.02	89.99	372.77	800.86	422.59	456.93	14.299	3.958	14.928	4.841	887.46	558.81
7	781.83	93.6	584.65	912.81	1521.46	492.43	13.392	6.231	13.76	6.635	1056.88	576.12
8	932.1	120.13	703.98	1121.1	1102.22	506.78	10.404	6.777	10.574	7.017	774.68	582.72
9	1039.3	196.26	745.54	1441.4	1279.07	726.85	9.243	3.669	9.309	4.032	1187.92	854.94
10	573.21	91.71	459.34	757.75	1234.86	353.78	20.273	6.206	20.89	6.414	1574.7	1042.79
11	694.94	93.97	583.57	920.2	940.79	413.04	14.681	4.223	15.091	4.749	1443.26	1106.33
12	733.28	101.19	616.78	1056.01	765.65	537.99	11.699	3.758	12.161	4.162	798.52	569.41
13	738.21	92.74	532.76	939	785.57	404.87	10.595	1.829	10.886	1.987	749.26	629.11
14	669.65	130.54	454.74	913.88	844.56	468.77	11.551	3.62	11.864	4.197	1129.22	846.72
15	684.23	78.43	573.72	862.85	953.73	367.45	10.495	2.229	10.925	2.465	855.97	655.67

Furthermore, Table 3.2 displays the local area compliance, as determined from the wall stiffness and using the ACM method. The two methods lead to similar area compliance results, with a mean difference of only $-0.359 \cdot 10^{-3} \pm 0.166 \cdot 10^{-3}$ $cm^2/mmHg$.

Finally, Table 3.2 also displays the downstream volumetric compliances as determined at the inlet of the ascending aorta and the inlet of the descending aorta. The average total volumetric compliance is of $988.4 \cdot 10^{-6} \pm 297.7 \cdot 10^{-6}$ cm^4s^2/g, which is in the range of previously reported values in the literature. On average, the descending aorta volumetric compliance is 29% smaller than the ascending aorta volumetric compliance.

Figure 3.8 displays for patient dataset 15 a comparison of the local area compliance, as determined from the wall stiffness and using the ACM method, and the downstream volumetric compliance along the centerline of the aorta. The regions with large local area compliance are the regions with low local PWV (see Figure 3.7) and vice-versa (the area compliance and the PWV are inversely proportional). The downstream volumetric compliance decreases significantly towards the descending aorta. A marked decrease can be observed once the bifurcation points of the supra-aortic branches have been passed. This is due to the fact that the downstream compliance at an ascending aorta location contains the volumetric compliance of all arteries supplying the arms and the cerebral circulation.

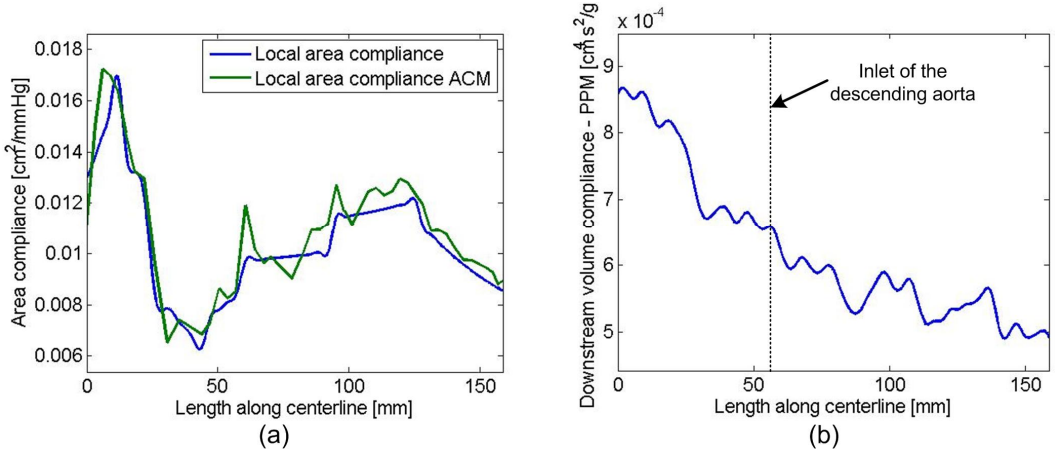

Figure 3.8: (a) Local area compliance as determined from the wall stiffness and using the ACM method along the centerline of the aorta; (b) Downstream volumetric compliance determined with the pressure-pulse method along the centerline of the aorta (both for patient dataset 15).

3.4 DISCUSSION AND CONCLUSIONS

This chapter introduced a parameter estimation framework for automatically and robustly personalizing aortic hemodynamic computations from 4D MRI medical image data. The hemodynamic computations are based on a reduced-order multiscale fluid-structure interaction (FSI) blood flow model, which is fully personalized: the patient-specific anatomical model and the time-varying flow rate inlet boundary condition are derived directly from the medical imaging data, and the proposed parameter estimation framework calibrates the parameters of the outlet boundary conditions and the regional mechanical wall properties along the centerline of the aorta so as to match the clinical measurements. The former are personalized by solving a nonlinear system of equations, while the latter are personalized by minimizing a cost-function. Due to the different nature of the calibration procedures, these are run sequentially and iteratively until both of them are converged.

The methodology was evaluated by investigating 15 patient datasets. Since all of them converged successfully within only two global iterations, three iterations for the calibration of the outlet boundary conditions, and ten iterations for the calibration of the regional mechanical wall properties, the proposed method is deemed robust. The estimated aortic pressures and flow-rate distributions between supra-aortic branches and descending aorta were matched with an error of less than 1%. Three-element Windkessel models were used as outlet boundary conditions, but other types of physiologically sound boundary conditions, like the structured tree boundary condition, may be employed instead [Itu et al., 2017]. The cost function related to the estimation of regional mechanical wall properties, computed based on the differences between the cross-sectional area variations in the 4D MRI data and the blood flow model, was minimized to an average value of 0.23 cm^2 for the entire cohort. Moreover, as can be observed in Figure 3.6, not only the cross-sectional area variation (difference between minimum and maximum value) is matched well, but also the time-varying cross-sectional area profiles typically match the measured profiles.

In addition to its robustness and excellent capability of matching the clinical measurements, the proposed method is computationally also very efficient: the average execution time was of only 6.2 ± 1.2 minutes on a standard hardware configuration. There are several aspects contributing to this achievement. First of all, a computationally efficient reduced-order fluid-structure interaction model was used. Secondly, the parameters in the outlet boundary conditions are initialized by solving the system of nonlinear equations for a lumped parameter model composed of the Windkessel models used in the multiscale model (Figure 3.3b). Thirdly, the solution determined for the lumped parameter model is adapted to compensate for the hemodynamic properties (resistance and compliance) of the multiscale model. As a result, the calibration procedures required a reduced number of calibration iterations. Hence, one can conclude that the proposed framework is well suited for a clinical decision setting, where short runtimes are crucial. If required, the computational time can be further reduced by employing modern Graphics Processing Units (GPUs) for massively parallelized computations with a potential speed-up of approximately a factor of four [Itu et al., 2013(b)].

As mentioned above, a major contribution of the framework is that spatially varying personalized regional mechanical wall properties are derived. This is in contrast with previous approaches, where a single PWV value was estimated for the entire domain. As can be observed in Figure 3.5b, the spatial variation of the vascular wall properties can be quite pronounced. There are several factors which may contribute to this finding. First of all, all 15 patient datasets of this cohort had aortic valve disease, which leads to a modification of the flow jet through the aortic valve and potentially to an adaptation of the wall properties (especially in the ascending aorta and in the aortic arch). Secondly, previous research has shown that the surrounding tissue of the aorta has a considerable effect on the hemodynamics, leading to higher wave speed, lower total compliance, etc. [Itu et al., 2014(a)]. Since the various structures surrounding the aorta have different elastic properties, they provide spatially varying external tissue support along the centerline of the aorta.

The main difference to previously introduced methods estimating local vascular wall properties, is that herein these wall properties are personalized in the context of a blood flow model, which enforces the physics of fluid flow in elastic domains. Consequently, the results are less affected by measurement noise.

Arterial distensibility is an important factor for the development and assessment of cardiovascular diseases, as elevated systemic vascular stiffness is associated with an increased

risk of cardiovascular disease. There are several pathological conditions where the knowledge of regional instead of global mechanical wall properties is of interest. For example, in case of aortic valve stenosis, a more focused flow jet may affect the aortic wall and cause dilatation of the ascending aorta. Other potential applications are related to the understanding of the development of aortic dissections or aortic aneurysms. Furthermore, previous studies have shown that in case of aortic coarctation the local compliance plays a crucial role in the estimation of the peak-to-peak pressure drop, a measure that is routinely used for clinical decision making [Keshavarz-Motamed et al., 2015]. Furthermore, for stented aortic coarctations, the interplay between the different mechanical properties of the stent and of the surrounding aortic segments is of interest.

The study has a series of limitations. Firstly, it has been evaluated only on 15 patient datasets thus far, and hence the results are preliminary and warrant an evaluation study on a larger number of datasets to be clinically relevant. Secondly, the proposed method has not been tested for anatomical models representative of pathologies which induce severe modifications of the aortic geometry, e.g. aortic coarctation. To account for the effect of the aortic coarctation on the hemodynamics a modified reduced-order model would be required [Itu et al., 2013(a)]. Thirdly, the reduced-order model introduces an approximation of the geometry, since an axisymmetric, tapering geometry is being considered. However, it has been shown that the one-dimensional model is able to predict time-varying pressure and flow rate waveforms if the tapering is moderate [Reymond et al., 2011]. Finally, although information on the variation of the cross-sectional areas at many locations of the aorta was used in the framework, the global and other movements of the aorta during a heart cycle were not fully taken into account.

4. A Method for Modeling Surrounding Tissue Support and its Global Effects on Arterial Hemodynamics

4.1 INTRODUCTION

While three-dimensional models have been used to analyze pathologic behavior of blood vessels in local geometries [Cebral et al., 2011], one-dimensional blood flow models have been used extensively for modeling the entire arterial circulation [van de Vosse et al., 2011]. When the focus lies on flow rate and pressure wave forms, one-dimensional models are an ideal approach since they have been shown to be able to accurately predict these quantities for patient-specific models [Itu et al., 2013(a)].

One-dimensional models have been previously used to assess the effect of arterial stiffness [Mathhys et al., 2007], whose changes represent an early risk factor for cardiovascular diseases (hypertension, diabetes, hyperlipidemia, atherosclerosis, heart failure, etc. [Laurent et al., 2006]).

Previous studies have suggested that, for a correct, model based assessment of arterial stiffness effects, the influence of the surrounding tissue has to be considered [Liu et al., 2007]. The surrounding tissue constrains the vessels radially, it reduces the wall strain and stress, and takes up a significant part of the intravascular pressure (wall stretch ratio was reduced by 15 – 20% for the carotid and femoral arteries).

The effect of surrounding tissue on the proximal aorta hemodynamics has been analyzed using two different fluid structure interaction (FSI) modeling techniques and results have shown

that the motion of the arterial wall, otherwise left free, is constrained, whereas the constraints for inlet and outlet regions are relaxed [Moireau et al., 2012].

Recently, two idealized computational models have been proposed for studying the effects of surrounding tissue, the uniform thickness model and the histology image-based model [Kim et al., 2013]. Results have indicated that modeling of the surrounding tissue improves the understanding of regional adaptation of the aortic wall at normal and pathological conditions. For the coronary arteries it has been shown that large epicardial coronary vessels have a greater tendency to become thicker in the absence of myocardial constraint [Liu et al., 2008].

In this chapter a methodology for separating the total stiffness of arteries, determined in vivo, into stiffness of the arterial wall and stiffness of the surrounding tissue is introduced [Itu et al., 2014(a)]. The above described studies focused on local effects of surrounding tissue support through detailed in vivo, in vitro and in silico experiments. The methodology introduced herein is used for studying the global effects of surrounding tissue support on arterial hemodynamics by employing a one-dimensional blood flow model for a full body arterial model composed of 51 arteries.

4.2 METHODS

The one-dimensional blood flow model is derived from the three-dimensional Navier-Stokes equations:

$$\frac{\partial A(x,t)}{\partial t} + \frac{\partial q(x,t)}{\partial x} = 0\,, \tag{4.1}$$

$$\frac{\partial q(x,t)}{\partial t} + \frac{\partial}{\partial x}\left(\alpha \frac{q^2(x,t)}{A(x,t)}\right) + \frac{A(x,t)}{\rho} \frac{\partial p(x,t)}{\partial x} = K_R \frac{q(x,t)}{A(x,t)}\,, \tag{4.2}$$

where x denotes the axial location and t denotes the time. $A(x,t)$ is the cross-sectional area, $p(x,t)$ the pressure, $q(x,t)$ the flow rate, and ρ is the density. Coefficients α and K_R account for the momentum-flux correction and viscous losses due to friction respectively. A third equation is required to close the system: the state equation, which relates the pressure inside the vessels to the cross-sectional area. The vessel wall is modeled as a viscoelastic material:

$$P(x,t) = \frac{4}{3}\frac{Eh}{r_0}(x)\left(1 - \sqrt{\frac{A_0(x)}{A(x,t)}}\right) + \frac{\gamma_S}{A\sqrt{A}}\frac{\partial A}{\partial t} + P_0\,, \tag{4.3}$$

where E is the Young modulus, h is the wall thickness, r_0 is the initial radius corresponding to the initial pressure P_0, and γ_S is the viscoelastic coefficient. The elastic wall properties are estimated using a best fit to in vivo data [Olufsen et al., 2000]:

$$\frac{Eh}{r_0}(x) = k_1 \cdot \exp(k_2 \cdot r_0(x)) + k_3\,, \tag{4.4}$$

where $k_1 = 2\cdot10^7$ g/(s^2·cm), $k_2 = -22.53$ cm^{-1}, $k_3 = 6.65\cdot10^7$ g/(s^2·cm). The wall properties determined with (4.4) contain the influence of the external tissue. To study the global effects of surrounding tissue, the material properties in (4.3) need to be adapted in order to exclude the influence of the surrounding tissue. Liu et al. [Liu et al., 2007] have shown that, at a reference pressure of 100 mmHg, the radiuses increase by ~15-20% when the external tissue is not present. To model the effect of the surrounding tissue, they considered an external pressure, called

effective perivascular pressure (*EPP*), which introduces a radial constraint. As the tests with different arterial pressure values have shown, *EPP* represents a fraction of the arterial pressure, and can be expressed as:

$$P_{ext} = (1 - k)P_a , \tag{4.5}$$

where P_a is the arterial pressure and k is a constant which is equal to 0.5 at physiological pressures (60 – 120 mmHg).

When acquiring image data (magnetic resonance, computer tomography, etc.), arterial geometries are regularly reconstructed based on diastolic time frames, where motion artifacts are smallest. Hence, the measured radiuses and cross-sectional areas correspond to a non-zero pressure (the diastolic pressure). Generally, the pressure inside an artery can be expressed as:

$$P = P_{tm} + P_{ext} , \tag{4.6}$$

where P_{tm} is the transmural pressure and P_{ext} is the pressure exerted by the surrounding tissue on the arterial wall (EPP). Hence, for the initial state, one can write $P_{Dia} = P_0 = (P_{tm})_0 + (P_{ext})_0$. Figure 4.1 displays the different pressures inside the artery, in the surrounding tissue, and the transmural pressure for (a), the initial state, and for (b), a generic case with a higher pressure.

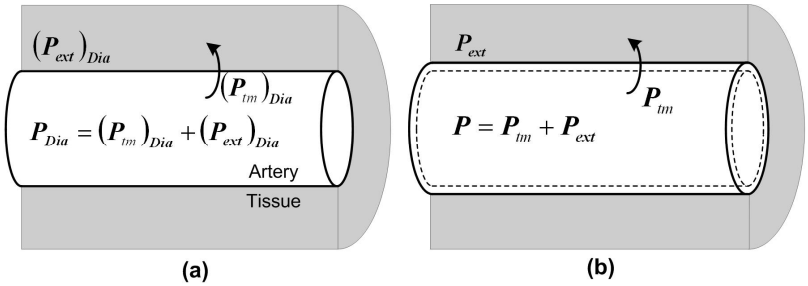

Figure 4.1: Absolute pressures in the arteries and in the surrounding tissue: (a) in the initial state (at diastolic pressure), and (b) at a certain moment during the cardiac cycle when the pressure is higher than the diastolic pressure.

It is not possible to introduce the external pressure in (4.3), since the material properties of the elastic component already contain its influence. Hence, the initial state corresponding to pressure P_{Dia} and cross-sectional area A_{Dia} can not be used as a starting point for the separation of the arterial wall model from the external tissue model. The only state in which the external tissue has no influence on the arterial properties is the hypothetical case obtained with zero pressure. To determine the cross-sectional area value corresponding to zero pressure the method proposed in [Alstruey et al., 2009] is used. Thus, (4.3) is considered without the viscoelastic term, and P_0 is set to 0 mmHg, while A_0 is the cross-sectional area zero pressure.

$$A_0(x) = A_{Dia}(x)\left(1 - \frac{P_{Dia}(x)}{(Eh/r_0)(x)}\right). \tag{4.7}$$

The viscoelastic term can be excluded if the diastolic and the hypothetical zero pressure states are considered to be steady-states. In reality, the diastolic state is not a steady state, since the geometry is usually acquired in vivo, but at the end of diastole the variation of the cross-sectional area is small and hence the viscoelastic term can be neglected.

To model the effect of the external tissue the method introduced recently in [Formaggia et al., 2013] is considered, whereby the stiffness of the arterial wall and of the surrounding tissue are modeled separately as two springs in parallel, as is displayed in Figure 4.2: K_{1D} is the stiffness of the arterial wall and K_{ST} is the stiffness of the surrounding tissue. As a result, the total stiffness is computed as:

$$K_{eq} = K_{1D} + K_{ST}. \tag{4.8}$$

From (4.3), the equivalent stiffness is expressed as:

$$K_{eq} = \frac{4}{3}\frac{Eh}{r_0}\frac{1}{r_0}. \tag{4.9}$$

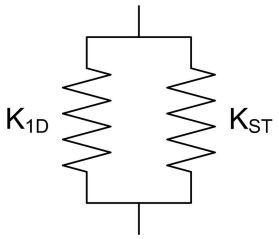

Figure 4.2: Equivalent model of the total stiffness in the wall encountered by the one-dimensional blood flow model: K1D is the stiffness of the arterial wall and KST is the stiffness of the surrounding tissue.

To determine K_{1D}, the quantity $\left(Eh/r_0\right)_w(x)$ is introduced, whereas subscript *w* indicates the fact that it only refers to the properties of the wall (excluding the surrounding tissue properties). Considering only the steady-state equation, one can write for a non-zero pressure $P(x)$:

$$P(x) = \frac{4}{3}\frac{Eh}{r_0}(x)\left(1 - \sqrt{\frac{A_0(x)}{A(x,t)}}\right), \tag{4.10}$$

$$P(x) = \frac{4}{3}\left(\frac{Eh}{r_0}\right)_w(x)\left(1 - \sqrt{\frac{A_0(x)}{A(x,t)}}\right) + P_{ext}(x) = \frac{4}{3}\left(\frac{Eh}{r_0}\right)_w(x)\left(1 - \sqrt{\frac{A_0(x)}{A(x,t)}}\right) + (1-k)P(x), \tag{4.11}$$

where A_0 is the cross-sectional area corresponding to zero pressure, determined in (4.7). Next, (4.10) is introduced in (4.11), and, as a result:

$$\left(\frac{Eh}{r_0}\right)_w(x) = k\frac{Eh}{r_0}(x). \tag{4.12}$$

Hence, the stiffness of the arterial wall and of the surrounding tissue can be expressed separately as:

$$K_{1D} = k\frac{4}{3}\frac{Eh}{r_0}\frac{1}{r_0}, \tag{4.13}$$

$$K_{ST} = (1-k)\frac{4}{3}\frac{Eh}{r_0}\frac{1}{r_0}. \tag{4.14}$$

4.3 RESULTS

Blood was modeled as an incompressible Newtonian fluid with a density of ρ = 1.055 g/cm3 and a dynamic viscosity of μ = 0.045 dynes/cm2.s for all the computations.

To evaluate the global effects of surrounding tissue on the arterial circulation, the arterial tree detailed in [Bessems, 2008], and displayed in Figure 4.3a was used. It is composed of 51 arteries. A time-varying flow rate profile was imposed at the inlet [Olufsen et al., 2000] and three-element Windkessel lumped models were applied at the outlets.

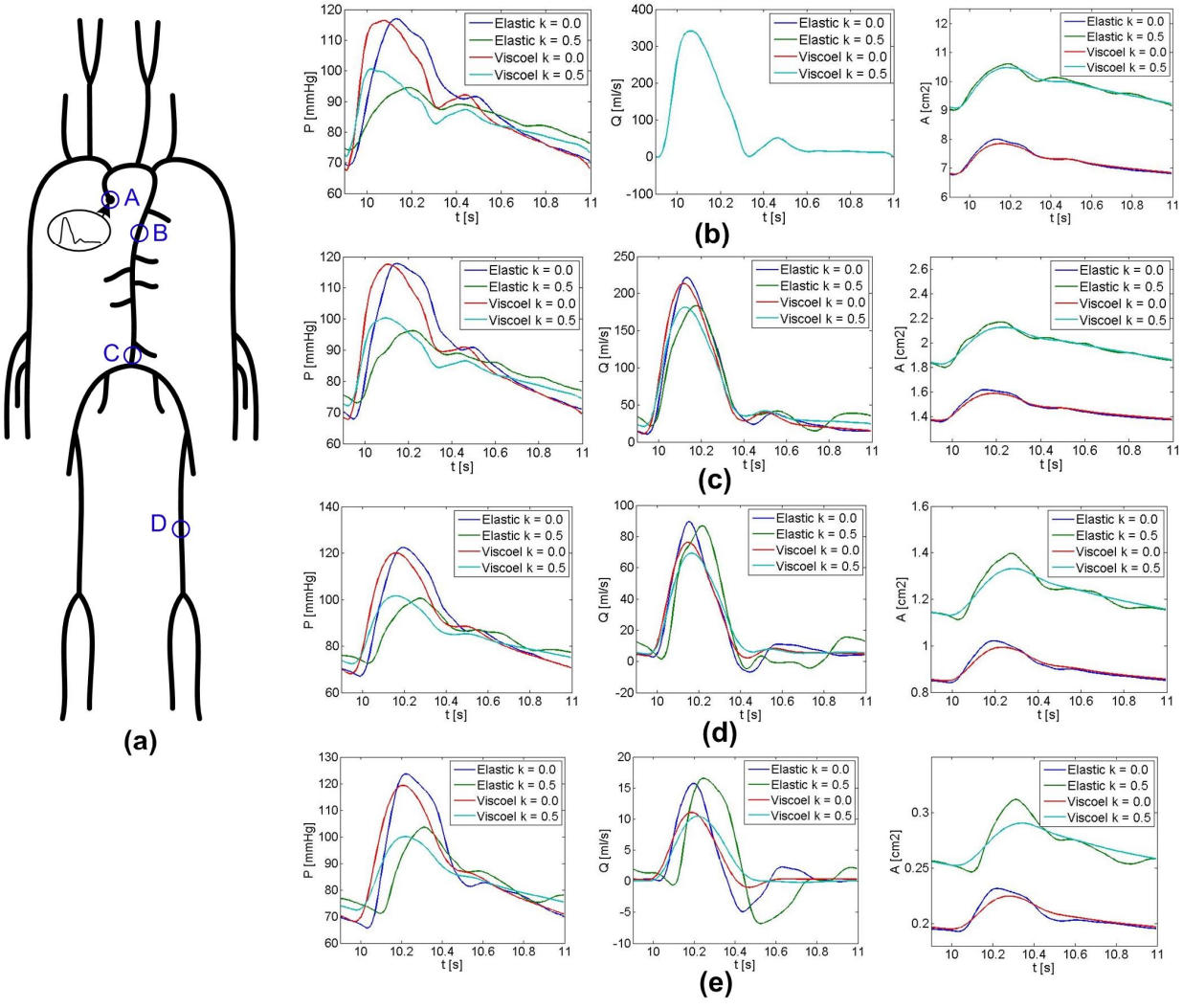

Figure 4.3: (a) Representation of the 51 main arteries in the human arterial system; time-varying pressure, flow rate and cross-sectional area with an elastic/viscoelastic wall model and with/without the effect of surrounding tissue at (b) aortic root, (c) descending aorta, (d) abdominal aorta, and (e) femoral artery.

Results are displayed in the following for both an elastic and viscoelastic arterial wall model. The constant *k* in (4.15) was set equal to 0 (includes the effects of the surrounding tissue) or 0.5 (a value determined experimentally by Liu et al., which excludes the influence of the surrounding tissue).

Hence, four computational setups were obtained, and, to analyze the effect only for the large arteries, Windkessel boundary condition values were the same in all four cases.

The results are displayed in Figure 4.3b-e at the locations marked with a blue circle in Figure 4.3a. For the aortic root the pressure pulse is much smaller when the effect of the surrounding tissue is excluded, the difference being caused mainly by the change in systolic pressure. The decreased pressure pulse is given by the increased compliance of the system, and by the fact that the lower total stiffness of the wall leads to a lower wave speed and hence to reflections which arrive back later in the proximal part of the circulation (these reflections are no longer arriving at late systole, but during diastole). In terms of the cross-sectional area an increase of up to 30% is obtained for the aortic root, confirming the finding of Liu et al., which indicated that the surrounding tissue prevents the arteries from overstretching. Further downstream, the decrease in pressure pulse is not as pronounced as before, mainly because the reflections arrive earlier at the corresponding locations (the compliance is still increased). In terms of the flow rate, especially for distal locations, the oscillations increase, being very pronounced in the femoral artery. The decrease in wave speed, can be observed through the difference of the onset (the foot) of the flow rate wave for the distal locations.

Finally, when setting k to 0.5, the total systemic resistance decreases from 1.42e3 to 1.36e3 dynes·s/cm^5 and is accompanied by a corresponding decrease of the arterial average pressure. This change is given by the fact that the radiuses are larger when the surrounding tissue is absent and the resistance of a vessel is proportional to the inverse of the radius at power 4. Although the radiuses increase by a considerable amount, the decrease in total resistance is only marginal because the large arteries contribute very little to the total arterial resistance, which is mainly located in the small arteries lumped in the Windkessel elements.

4.4 CONCLUSIONS

In this chapter arterial wall and surrounding tissue properties have been determined from in vivo data and have studied the global effects of surrounding tissue on arterial hemodynamics. A one-dimensional blood flow model has been employed, which enables the assessment of the effects on pressure, flow rate and cross-sectional area profiles.

The main effects of the surrounding tissue have been determined: higher wave speed and lower total compliance. Consequently, backward travelling pressure and flow rate waves arrive earlier in the proximal part of the circulation and a higher pressure pulse is obtained. Secondly, cross-sectional area values decrease by over 30%.

To study local hemodynamic quantities of interest (wall shear stress, circumferential strain) in greater detail, the one-dimensional model can be coupled to a three-dimensional model employed for the region of interest [Formaggia et al., 2013].

The herein provided methodology is useful for predicting and studying the effect of local changes to the external tissue support on global hemodynamics. Moreover, the computed hemodynamic and mechanical quantities of interest can be used together with a growth model [Figueroa et al., 2013] to predict arterial wall growth and remodeling. In a *Big Data* perspective, by comparing simulation results and patient evolution over different time ranges, such an approach is useful for predicting patient-specific disease evolution and outcome.

The study has a series of limitations. First of all, due to lack of experimental data, a uniform effect of the surrounding tissue along the large arteries was considered. Secondly, the influence of the surrounding tissue was considered to be purely elastic and the viscoelastic properties were attributed solely to the arterial wall.

5. Model Based Non-invasive Estimation of PV Loop from Echocardiography

5.1 INTRODUCTION

The left ventricular pressure-volume (PV) loop represents an efficient tool for understanding and characterizing cardiac function. It contains information regarding stroke volume, cardiac output, ejection fraction, myocardial contractility, cardiac oxygen consumption, and other important measures of the heart and the systemic circulation. For example, the extent of ventricular remodeling, the degree of ventricular-arterial mismatching [Burkhoff, 2013], and the left ventricular end-diastolic pressure-volume relationship [Spevack et al., 2013] represent strong predictors of congestive heart failure. Pathologies such as left ventricular hypertrophy, dilated cardiomyopathy, aortic and mitral valve stenosis, and regurgitation [Hall, 2011] are manifested in the PV-loop. Hence, a method for an efficient estimation of the PV loop would represent a powerful diagnostic tool for clinicians. Medical imaging modalities such as MRI, CT, and echocardiography can be used to estimate the time-varying LV volume through the heart cycle in a non-invasive manner, which can then be combined with an invasive measurement of LV pressure to obtain the PV loop [van Slochteren et al., 2012].

In this chapter, a model-based approach is introduced for the non-invasive estimation of left ventricular, patient-specific PV loops: a lumped parameter circulation model is personalized using a two step parameter estimation framework [Itu et al., 2014(b)]. The input data required for the model personalization are acquired through routine non-invasive clinical measurements and echocardiography.

In a clinical scenario, the values of the cardiovascular model parameters are not available on a per-patient basis, and different optimization-based approaches were proposed to estimate these parameters, focused mainly on the arterial systemic circulation. A fully automatic calibration method for Windkessel models was suggested [Itu et al., 2015], where the input was specified by non-invasively acquired systolic/diastolic pressures and, in some cases, additional flow data. In a different approach, Windkessel parameters were estimated using a state-space approach and a least squares method from time-varying pressure and flow rate profiles [Kind et al., 2010].

5.2 METHODS

5.2.1 Lumped Parameter Model

The lumped parameter circulation model employed for the current study is displayed in Figure 5.1. It comprises three main components: venous pulmonary circulation, the left heart and the systemic circulation. For the venous part of the pulmonary circulation, a model composed of a resistance (R_{pulVen}) and compliance (C_{pulVen}) is used:

$$C_{pulVen}\frac{dP_{LA}}{\mathrm{dt}} = Q_{C\text{-}\,pulVen}, \tag{5.1}$$

$$Q_{pulVen} = Q_{C\text{-}\,pulVen} + Q_{LA\text{-}\,in}, \tag{5.2}$$

where the venous pulmonary flow rate (Q_{pulVen}) is considered to be constant in time.

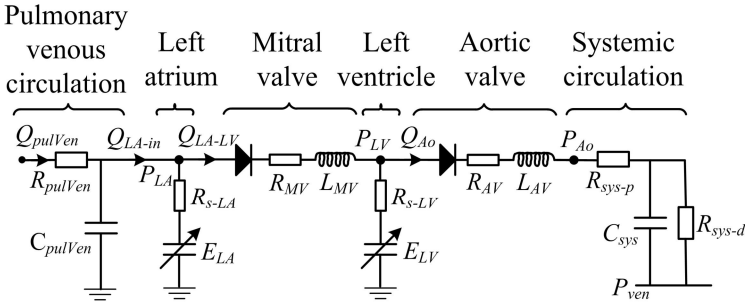

Figure 5.1: Lumped parameter model representing the venous pulmonary circulation, the left heart and the systemic circulation.

The left heart model has four components: left atrium (LA), mitral valve, left ventricle (LV) and aortic valve. A time-varying elastance model is used for the LA and the LV [Suga, 1971]:

$$P(t) = E(t)\times(V(t) - V_0) - R_s Q(t), \tag{5.3}$$

where E is the time-varying elastance, V is the cavity volume, V_0 is the dead volume of the cavity, and R_s is a source resistance which accounts for the dependence between the flow and the cavity pressure [Shroff et al., 1985] ($R_s = K_s E(t)(V(t) - V_0(t))$, K_s - constant). The cavity volume is equal to:

$$dV/\mathrm{dt} = Q_{in} - Q_{out}, \tag{5.4.}$$

where Q_{in} represents the inlet flow rate into the cavity and Q_{out} represents the outlet flow rate from the cavity. The mitral valve and the aortic valve are modeled using a resistance, an

inertance and a diode to simulate the closure and the opening of the valve [Mynard et al., 2012]. When the valve is open, the following relationship holds:

$$P_{in} - P_{out} = R_{valve} \times Q + L_{valve} \times dQ/\mathrm{dt}, \tag{5.5}$$

where P_{in} and P_{out} represent the pressures at the inlet and respectively the outlet of the valve. When the valve is closed, the flow rate through the valve is set to zero. Each valve opens when P_{in} becomes greater than P_{out}, and closes when the flow rate becomes negative. A three-element Windkessel model is used for the systemic circulation, represented by the following relationship between instantaneous flow and pressure:

$$\frac{dP_{Ao}}{\mathrm{dt}} = R_{sys-p}\frac{dQ_{Ao}}{\mathrm{dt}} - \frac{P_{Ao} - P_{ven}}{R_{sys-d} \times C_{sys}} + \frac{Q_{Ao}(R_{sys-p} + R_{sys-d})}{R_{sys-d} \times C_{sys}}, \tag{5.6}$$

where R_{sys-p} and R_{sys-d} are the proximal and distal resistances respectively, C_{sys} is the compliance, and P_{ven} is the venous pressure. A total of nine equations are obtained, which are solved implicitly using the forward Euler time integration scheme.

5.2.2 Parameter Estimation Framework

To compute patient-specific left ventricular PV loops using the lumped parameter model, the parameters of the model are personalized. The model personalization framework consists of two sequential steps. First, a series of parameters are computed directly, and next, a fully automatic optimization-based calibration method is employed to estimate the values of the remaining parameters, ensuring that the personalized computations match the measurements. Table 5.1 lists the patient-specific input parameters used in the current study, together with their source. Figure 5.2 displays an image acquired through echocardiography, illustrating the steps required for extracting the last two quantities from Table 5.1.

Table 5.1: List of patient-specific input parameters.

Input	Source
Systolic blood pressure (*SBP*)	Cuff measurement (arms)
Diastolic blood pressure (*DBP*)	Cuff measurement (arms)
Heart Rate (*HR*)	Routine measurement
Ejection fraction (*EF*)	Echocardiography
End-diastolic volume (*EDV*)	Echocardiography

During the first step of the parameter estimation framework, the mean arterial pressure (MAP) is determined:

$$MAP = DBP + \left[1/3 + \left(HR \times 0.0012\right)\right] \times \left(SBP - DBP\right). \tag{5.7}$$

Then, the end-systolic volume is computed:

$$ESV = EDV \times \left(1 - EF\right)/100. \tag{5.8}$$

Next, the stroke volume is determined:

$$SV = EDV - ESV, \tag{5.9}$$

and the average aortic flow rate is computed:

$$\overline{Q_{Ao}} = SV \times 60/HR. \tag{5.10}$$

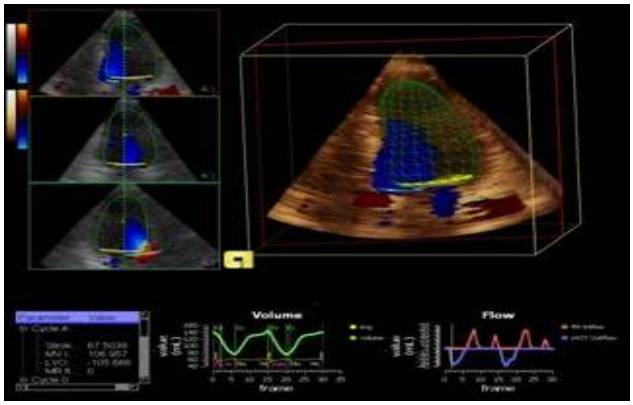

Figure 5.2: Image acquired through echocardiography illustrating the steps required to extract the end-diastolic volume and the ejection fraction.

Finally, the total systemic resistance, as well as the proximal and distal components, are determined:

$$R_{sys-t} = (MAP - P_v)/\overline{Q_{Ao}}, \quad R_{sys-p} = r \times R_{sys-t}; \quad R_{sys-d} = (1 - r) \times R_{sys-t}, \tag{5.11}$$

where ρ is the proximal resistance fraction. Since the lumped model is used for a pulsatile steady-state computation, the average inlet flow rate (Q_{pulVen}) is equal to the average outlet flow rate, given by (5.10). Hence:

$$Q_{pulVen} = \overline{Q_{Ao}}. \tag{5.12}$$

The normalized elastance curve is used for the left ventricle model [Suga, 1971], which is denormalized using the minimum and maximum elastance values, and the time at which the maximum elastance is reached. The minimum elastance value is set to 0.08 mmHg/ml, and the time at which the maximum elastance of the left ventricle is reached is computed using $t_{max} = 0.16 \cdot T + 0.17$, where T is the period.

The maximum elastance value is estimated as described further down. A two-hill function is used to determine the elastance curve for the left atrium, whereas the minimum elastance is set to 0.08 mmHg/ml, the maximum elastance is set to 0.17 mmHg/ml, and the onset of the contraction is set at $0.85T$ [Mynard et al., 2012].

During the second step of the parameter estimation framework, an optimization-based calibration method is employed to estimate the maximum elastance of the left ventricle model, E_{max-LV}, the dead volume of the left ventricle, V_{0-LV}, and the compliance of the systemic Windkessel model, C_{sys}.

The parameter estimation problem is formulated as a numerical optimization problem, the goal of which is to find a set of parameter values for which a set of objectives are met. Since the number of parameters to be estimated is set equal to the number of objectives, the parameter estimation problem becomes a problem of finding the root for a system of nonlinear equations. To solve the system of equations, the dogleg trust region method is used [Nocedal et al., 2006]. The objectives of the parameter estimation method are formulated based on the systolic and diastolic pressures, and the ejection fraction, leading to the system of nonlinear equations:

$$\mathbf{r}\begin{pmatrix} E_{max-LV} \\ V_{0-LV} \\ C_{sys} \end{pmatrix} = \begin{pmatrix} (SBP)_{comp} - (SBP)_{ref} \\ (DBP)_{comp} - (DBP)_{ref} \\ (EF)_{comp} - (EF)_{ref} \end{pmatrix} = \begin{pmatrix} 0 \\ 0 \\ 0 \end{pmatrix}, \tag{5.13}$$

where, $\boldsymbol{r}(\boldsymbol{x})$ is a vector function, called in the following objective function, and $\boldsymbol{x}$ is the vector of the unknowns, i.e. the parameters to be estimated. Each component of the objective function is formulated as the difference between the computed value of a quantity – $(\cdot)_{comp}$ (determined using the lumped parameter model) and its reference value – $(\cdot)_{ref}$ (determined through measurement). To evaluate the objective function for a given set of parameter values, the lumped parameter model is run exactly once.

An outline of the parameter estimation method is illustrated in Figure 5.3. First, a grid of physiological parameter value sets is considered, and the initial solution, $\boldsymbol{x}_0$, is chosen as the parameter value set leading to the smallest L_2 norm for the objective function $\boldsymbol{r}(\boldsymbol{x})$. Since the lumped parameter model has a small computational time, the Jacobian matrix required to compute the step size at each iteration of the optimization method is estimated using finite differences. The finite differences of the parameters, to be used for the computation of the Jacobian, are called in the following characteristic step sizes, s_j^{char}. To determine the characteristic step sizes, a set of characteristic values for the objective function are chosen, r_i^{char}, and apply a fixed point iteration method. The fixed point iteration method consists of two sequential steps. First, the characteristic step size values are computed:

$$s_j^{char} = 1 \Big/ \sqrt{\sum_{i=1}^{n_{eq}} \left(J_{ij} / r_i^{char} \right)}. \tag{5.14}$$

Next, the Jacobian matrix is computed:

$$J_{ij} = \frac{1}{s_j^{char}} \left[\mathbf{r}\left(\mathbf{x}_0 + \frac{1}{2} s_j^{char} \mathbf{d}_j \right) - \mathbf{r}\left(\mathbf{x}_0 - \frac{1}{2} s_j^{char} \mathbf{d}_j \right) \right] \times \mathbf{d}_i, \tag{5.15}$$

where $\boldsymbol{d}_i$ and $\boldsymbol{d}_j$ represent the unit vectors in the ith and jth direction. These two steps are iterated until the characteristic step size is consistent with the chosen characteristic objective function. Next, the lumped parameter model is run using the current parameter value set and the objective function is evaluated. Each computation, with a given set of parameter values, is run until the L_2 norms of the normalized differences between the aortic pressure and flow rate profiles at the current and the previous cardiac cycle are smaller than 10^{-5}. If all objective function values are smaller than the tolerance limit ($r_i^{char}/10$), the calibration method is terminated. Otherwise, the Jacobian matrix is recomputed and the parameter values are updated. The characteristic values for the pressure and ejection fraction objectives were set to 1 mmHg and 0.005 respectively. When applying the dogleg trust region method, the parameters and the objective function components are scaled using the previously determined characteristic values. Although the patient-specific values of the end-diastolic and end-systolic volumes are neither used directly as parameters of the lumped model nor tuned, they are automatically matched. This can be motivated as follows: the outlet flow rate of the model is imposed through the inlet pulmonary venous flow rate (eq. (5.12)), and since *HR* is imposed for the left atrium and ventricle models, the patient-specific stroke volume *SV* is matched (eq. (5.10)). In the system of equations composed of (5.8) and (5.9), *SV* is matched, and *EF* is matched as a result of running the

calibration method. Hence, only two unknowns are remaining (*EDV* and *ESV*), leading to a unique solution of the system.

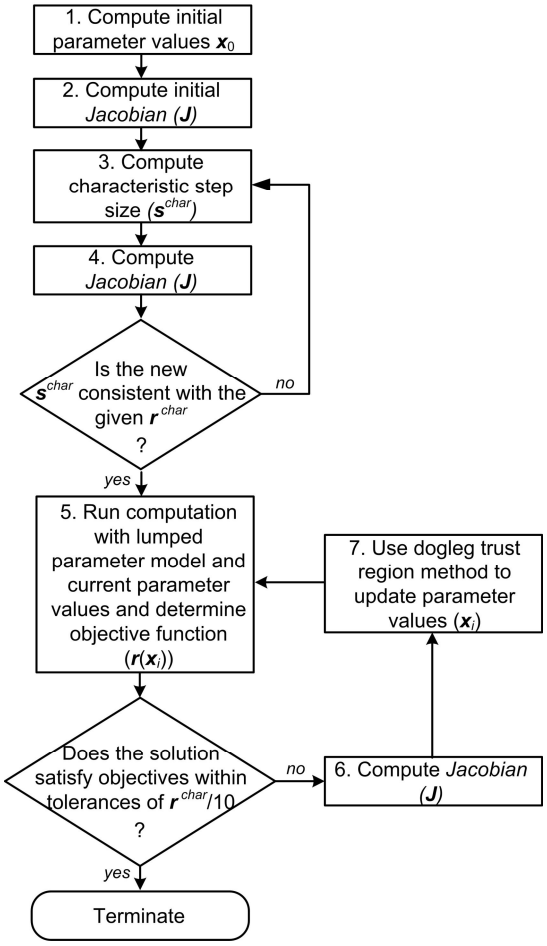

Figure 4.3: Parameter calibration method.

5.3 RESULTS

To evaluate the performance of the proposed methodology for the non-invasive estimation of left ventricular PV loops, next results are presented for three healthy volunteers. Systolic and diastolic pressure values were acquired using cuff-based measurements and the ejection fraction and end diastolic volumes were estimated from the echocardiography performed at rest state in a horizontal position using the Siemens ACUSON SC 2000 ultrasound system. The values of the parameters which are not estimated through the methodology described in the previous section were set as follows, based on literature data [Mynard et al., 2012], [Segers et al., 2003]: R_{AV} = 25.0 g/(cm^4·s), L_{AV} = 0.5 cm^2/s, R_{MV} = 20.0 g/(cm^4·s), L_{MV} = 0.5 cm^2/s, R_{pulVen} = 30.0 g/(cm^4·s), C_{pulVen} = 0.5 (cm^4·s^2)/g, ρ = 0.09, P_{ven} = 5.0 mmHg, $V_{0\text{-}LA}$ = 3 ml, $K_{s\text{-}LA}$ = 10·10-9 s/ml, and $K_{s\text{-}LV}$ = 4·10-9 s/ml.

Table 5.2 lists the input parameters for the three healthy volunteers, and the output parameters obtained after applying the parameter estimation framework. The output parameter values are in the physiological range reported in literature [Hall, 2011]. The computed time-varying pressure profiles and PV loops are displayed in Figure 5.4: left - aortic systolic and diastolic pressures, as well as the heart rate are matched exactly, right – end-diastolic volume and the ejection fraction, from Table 5.2, are exactly matched.

Table 5.2: Input and output parameter values for three healthy volunteers.

Parameter	Volunt. 1	Volunt. 2	Volunt. 3
SBP [mmHg]	120	117	117
DBP [mmHg]	70	65	67
HR [bpm]	86	61	90
EF	70 %	69 %	61 %
EDV [ml]	108	108	78
$E_{max\text{-}LV}$ [mmHg/ml]	3.30	2.40	1.52
$V_{0\text{-}LV}$ [ml]	2.18	4.33	-43.41
C_{sys} [$cm^4 \cdot s^2/g$]	$1.383 \cdot 10^{-3}$	$1.930 \cdot 10^{-3}$	$0.749 \cdot 10^{-3}$

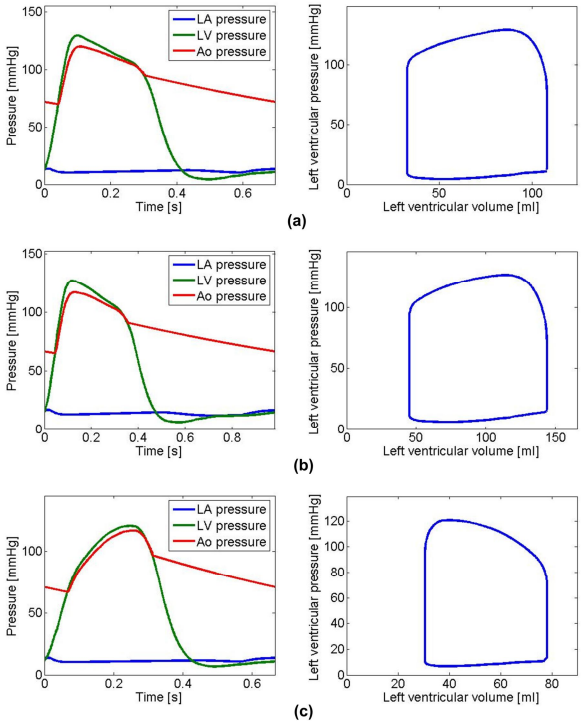

Figure 5.4: Computed time-varying LA pressure, LV pressure and aortic pressure (left side) and PV loops for (a) volunteer 1, (b) volunteer 2, and (c) volunteer 3.

Additionally, to perform an initial validation of the methodology, the PV loop was computed for a patient with mild aortic valve regurgitation and the results were compared against the invasively determined quantities. Figure 5.5 displays a comparison between model-based computed results and invasively performed measurements. The input data used for the parameter estimation framework were extracted from the invasive measurements as follows: *SBP* was the maximum aortic pressure (181.5 mmHg), *DBP* was the minimum aortic pressure (89.7 mmHg), *EDV* was the maximum LV volume (196.68 ml), *EF* (53.1 %) was computed from EDV and ESV, determined as minimum LV volume (92.26 *ml*), and *HR* was determined from the period of the time-varying pressure (47 bpm). All these values are matched exactly for the output parameter values: $E_{max\text{-}LV}$ = 0.968 mmHg/ml, $V_{0\text{-}LV}$ = -88.71 ml, C_{sys} = $1.065 \cdot 10^{-3}$ $cm^4 \cdot s^2/g$. There is a close agreement between the time-varying LV and aortic pressures, time-varying LV volumes, and PV loops. Moreover, the four phases of the cardiac cycle can be clearly identified in the computed results (Figure 5.5a and Figure 5.5b): 1: isovolumetric contraction phase, 2:

ventricular ejection phase, 3: isovolumetric relaxation phase, and 4: ventricular filling phase. The mild aortic valve regurgitation can be observed in the PV loop in Figure 5.5c, where the line corresponding to the isovolumetric relaxation has a slight curvature, and in Figure 5.5b, during the second part of phase 3, where the LV volume increases slightly. The average execution time for the four volunteers / patients was of 28.9 seconds on a standard Intel i7 CPU core with 3.4 GHz.

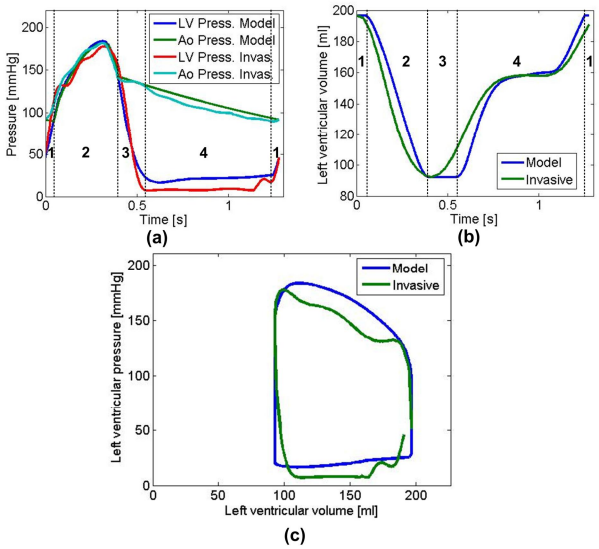

Figure 5.5: Comparison of model-based computation against invasive measurements, for (a) time-varying left ventricular and aortic pressures, (b) time-varying left ventricular volume, and (c) PV loop.

5.4 DISCUSSION AND CONCLUSIONS

A fully automated, non-invasive model-based method for the estimation of patient-specific left ventricular PV loops was introduced. Initial results demonstrate that the proposed parameter estimation framework ensures a perfect agreement between the computed quantities and the clinical measurements. The lumped parameter model used in the current study has been designed specifically for the estimation of the left ventricular PV loop: it leads to fast computation times, and it enables the accurate computation of the main quantities required for the PV loop (time-varying LV pressure and volume). Although the current study used LV volume information acquired through echocardiography, the proposed method can be applied, without any restriction, along with other medical imaging techniques which can provide similar data: magnetic resonance, computer tomography.

The current study has a series of limitations. First, *SBP* and *DBP* for the three volunteers were acquired through cuff-based measurements, which do not exactly represent the aortic systolic and diastolic values. Secondly, the lumped parameter model in Figure 5.1 is designed for the estimation of the PV loop of healthy subjects. Future work will focus in the implementation of different mitral/aortic valve models, capable of modeling valve stenosis/regurgitation.

6. A Machine Learning Approach for Computation of Fractional Flow Reserve from Coronary Computed Tomography

6.1 INTRODUCTION

Cardiovascular disease is the leading cause of death, globally. Of these deaths, approximately 42% are caused by Coronary Artery Disease (CAD) [***WHO, 2015]. CAD patients suffer from a buildup of plaque in the coronary arteries, which results in a corresponding decrease of blood flow to the cardiac muscle, especially under stress. In severe cases, this reduction in flow could result in myocardial ischemia, and potentially death.

Previous investigations have shown that revascularization of blocked coronary arteries is preferred for severe lesions, whereas mild to moderate lesions are best treated using medical therapy alone [De Bruyne et al., 2012]. The decision to revascularize blocked coronaries is commonly performed considering anatomical markers extracted from invasive coronary angiography, such as the percentage reduction in lumen diameter. Invasive coronary angiography is the gold standard in CAD imaging [Levin, 1982], [Ryan, 2002]. Subjective assessment of angiographically apparent CAD is inadequate due to high degrees of intra-observer and inter-observer variability. Hence, the significance of coronary stenoses is routinely assessed by computer-assisted quantitative coronary angiography [Ng et al., 2011].

There is strong evidence that this approach has a limited accuracy in evaluating the hemodynamic significance of lesions [Toth et al., 2014].

Due to the tremendous improvement in medical imaging technologies, non-invasive imaging plays an increasingly important role in the diagnosis of CAD. Coronary Computed Tomography Angiography (CCTA) is a non-invasive imaging modality which is being increasingly used for the visualization and diagnosis of CAD, prior to invasive catheterization. While CCTA-based measurements of lesion anatomy correlate well with those from angiography, many severe lesions indicated by CCTA do not cause ischemia, leading to patients being unnecessarily referred to coronary angiography for invasive evaluation [Hachamovitch et al., 2008], [Meijboom et al., 2008]. In view of the limitations of the pure anatomical evaluation of CAD, the functional index of Fractional Flow Reserve (FFR) has been recently introduced as an alternative. FFR is defined as the ratio of flow in the stenosed branch at hyperemia – a condition of stress, with maximum coronary blood flow – to the hypothetical hyperemic flow in the same branch under healthy conditions. This can be shown to be closely approximated by the ratio of hyperemic cycle-averaged pressure distal to the stenosis to the cycle-averaged aortic pressure [Pijls et al., 1996]. Following multiple successful clinical trials which showed the superiority of FFR-guided decision making [Tonino et al., 2009], FFR is currently the gold standard for determining the functional severity of a lesion [Fihn et al., 2012], [Windecker et al., 2014]. Clinical evaluation of FFR is done under angiographic guidance, using a catheter-based pressure transducer. Despite the advantages offered by FFR, the use of FFR is still relatively uncommon [Petraco et al., 2013] due to additional costs, the need to administer drugs to induce hyperemia, and the invasive nature of the measurement [Tu et al., 2015].

Recently, blood flow computations performed using computational fluid dynamics (CFD) algorithms in conjunction with patient-specific anatomical models extracted from medical images, e. g. CT scans of the heart and the coronary arteries, have shown great promise in being able to predict invasive, lesion-specific FFR from patient's medical images taken at resting conditions [Coenen et al., 2015], [Koo et al., 2011], [Min et al., 2012], [Morris et al., 2013], [Norgard et al., 2014], [Papafaklis et al., 2014], [Renker et al., 2014], [Tu et al., 2014]. The CFD-based models combine geometrical information extracted from medical imaging with background knowledge on the physiology of the system, encoded in a complex mathematical fluid flow model consisting of partial differential equations which can be solved only numerically. This approach leads to a large number of algebraic equations, making it computationally very demanding [Tayloer et al., 2013]. Typically the solution of these models requires a few hours on powerful clusters for high-fidelity models representing the complete three dimensional velocity field to minutes on a workstation for reduced-order models which solve for time-varying pressure and flow rate in each branch [Itu et al., 2012], [Deng et al., 2015].

The computationally demanding aspect of these CFD models and associated image segmentation process prevents adoption of this technology for real-time applications such as intra-operative guidance of interventions. An alternative approach with high predictive power is based on machine learning (ML) algorithms.

In this chapter, a machine learning model for FFR computation is presented as an alternative to CFD-based modeling [Itu et al., 2016]. The model is trained using a synthetically generated database of 12000 coronary anatomies, resulting in a rich sampling of the different morphologies of coronary blockage. For each generated coronary tree, stenoses are randomly placed among the different branches and bifurcations. A reduced order CFD model [Itu et al., 2012] is used to compute the pressure and flow distribution for each coronary tree. Subsequently,

for each location along the coronary tree, quantitative features describing the anatomy as well as the computed FFR value at that location are extracted. A machine learning model is then trained to learn the relationship between the anatomical features and the FFR value computed using the CFD model. Once the model is trained, the computational time for predicting the FFR value for a new case is significantly lower than that of the CFD model, going from 196.3 ± 78.5 seconds for the CFD model to around 2.4 ± 0.44 seconds for the machine learning model on a workstation with 3.4 GHz Intel i7 8-core processor.

In the rest of the chapter, the computed FFR value is referred to as cFFR, and one distinguishes between $cFFR_{CFD}$ – computed with a CFD method, and $cFFR_{ML}$ – computed with the proposed machine learning method. The performance of the proposed machine learning based approach is assessed in three steps: (i) comparison against CFD predictions on synthetic coronary trees, (ii) comparison against CFD predictions on a set of 87 patient-specific coronary anatomies, and (iii) comparison against invasively measured FFR for the same 87 patients.

6.2 METHODS

In this section, the machine learning framework developed for computing cFFR from coronary anatomical models is introduced. First the process of generating the synthetic coronary vessel trees, which are used for training the machine learning model, is described, followed by the features used to map the relationship between the coronary anatomy and the computed value.

As described above, the machine-learning based model is trained offline on a large database of synthetically generated coronary anatomies. The prediction phase is an online process, whereby the algorithm computes $cFFR_{ML}$ for a given patient's data, by using the learned mapping from the training phase. Given an anatomical model (i.e., lumen segmentation), the computation of $cFFR_{ML}$ is fully automatic, without requiring user intervention. The pre-processing pipeline to generate the anatomical model is semi-automatic. The system presents the user with automatically computed centerlines and luminal contours, which can then be interactively edited by the user to create the anatomical model [Grosskopf et al., 2009]. The features required for the machine learning algorithm are automatically extracted from the reconstructed coronary anatomical model of the patient, and then used as input to the pre-learned model. $cFFR_{ML}$ is computed at all locations in the coronary arterial tree, and the resulting values are visualized by color coding the anatomical model. A schematic of the workflow is shown in Figure 6.1.

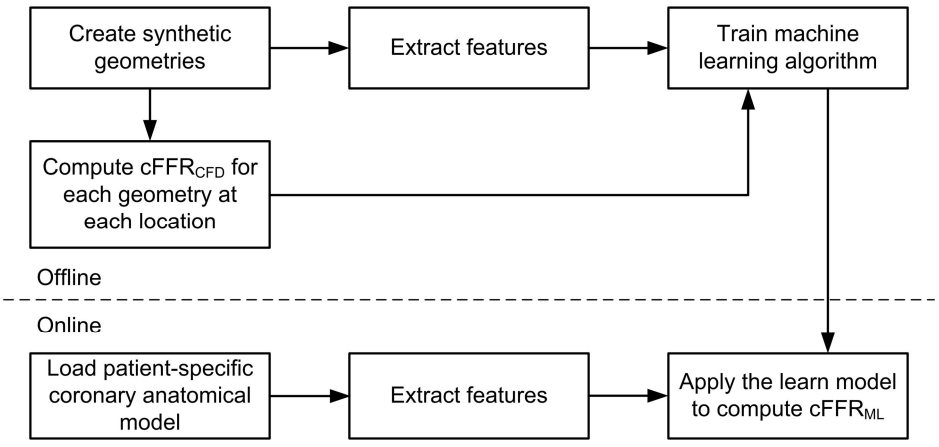

Figure 6.1: Overall workflow of the proposed framework.

6.2.1 Generation of synthetic training database

A database containing 12000 synthetically generated coronary vessel trees was created to reflect the anatomical variations representative of stable patients with suspected CAD. This database, used for training the machine learning model, is generated algorithmically using a three-step process, as shown in Figure 6.2. In the first step, the skeleton of the coronary geometry is initialized, by prescribing the number of vessels at each generation of the tree. During the second step, geometric information such as vessel radius, degree of tapering, branch length is prescribed for each generation of the vessel tree. The parameters representing these geometric quantities are sampled in pre-specified ranges derived from published literature (Table 6.1): the values have been selected to cover a broad range, ensuring that a wide array of anatomical variations and their corresponding hemodynamics is covered.

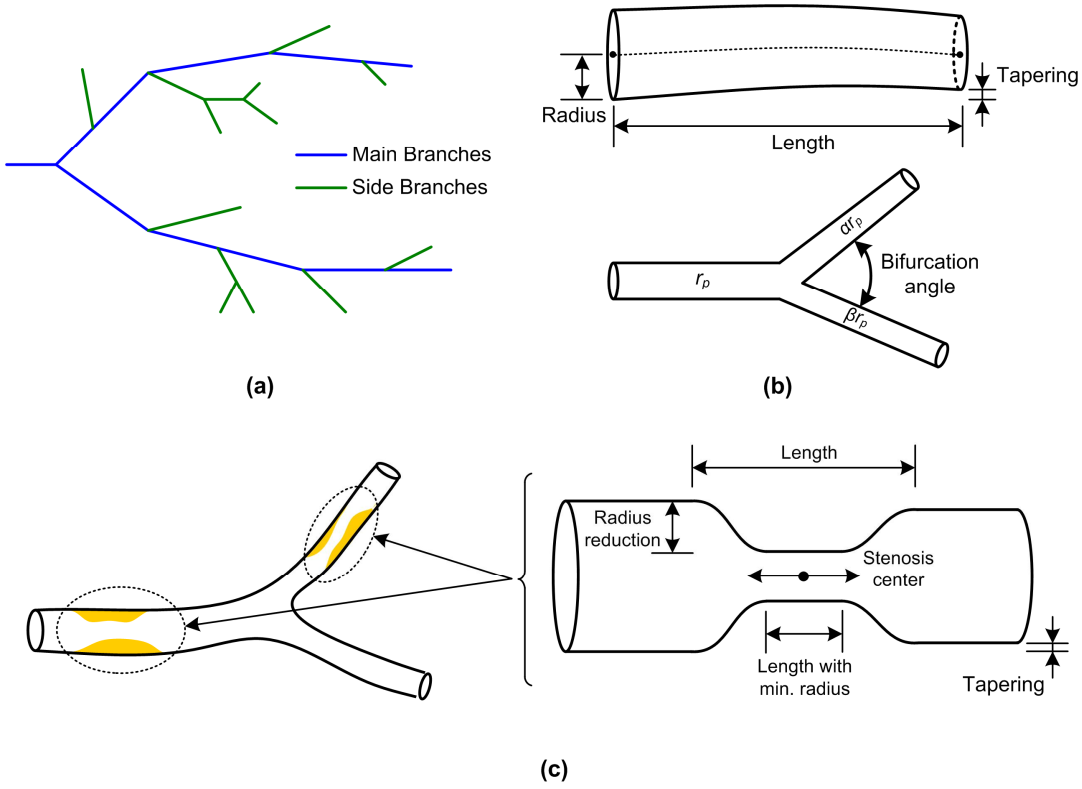

Figure 6.2: Generation of pathologic coronary geometries in three steps: (a) Set up coronary skeleton; (b) Generate healthy geometry information; (c) Generate stenoses.

During the third step, stenoses are generated in the coronary vessel trees. The number of stenoses on a vessel segment is sampled randomly between zero and three for a main branch segment, and between zero and two for a side branch segment. The following parameters are set for each stenosis: the maximum degree of radius reduction, the total length, the location of the stenosis center, the length of the stenosis region with minimum radius, the overall degree of tapering along the stenosis. Stenoses are placed either on a single segment, or at a bifurcation. If a bifurcation stenosis is generated, different stenosis parameter values are set for the parent and daughter branches of the bifurcation. A schematic description of the different parameters is shown in Figure 6.2. The parameters describing the root radius of the left main and the RCA

branch, and the maximum degree of radius reduction of a stenosis are sampled randomly based on a normal distribution. All other parameters are sampled with a uniform distribution.

Table 6.1: Parameters with corresponding ranges used to generate synthetic coronary trees.

Step	Parameter	Range
Step 1	Number of main branches	3 (LAD, LCx, RCA)
	Number of side branches (1^{st} gen)	2-5
	Number of side branches (2^{nd} gen)	0-2
Step 2	Root radius [Atta-Alla et al., 2015]	0.15-0.35cm
	Power coefficient [Kassab et al., 2006], [Murray, 1926], [Zamir et al., 1992]	2.1-2.7
	Area ratio [Olufsen et al., 2000]	0.35-0.45 (main branch), 0.6-0.8 (side branch)
	Degree of tapering [Zhou et al., 1999]	-20% to +5% from top to bottom
	Length [Aharinejad et al., 1998]	1.5-4cm
	Bifurcation angle [Kassab et al., 1995], [Atta-Alla et al., 2015]	30^0 - 90^0

By applying this three-step algorithm, a total of 12000 coronary geometries were generated. The coronary geometries generated are characteristic of many common pathological situations encountered in clinical practice. However, some rare conditions like anomalous origin of the coronary arteries and coronary artery aneurysms are not represented in this database.

6.2.2 Computational Fluid Dynamics simulations

The target values ($cFFR_{CFD}$), required for the training phase of the ML algorithm, are computed using a reduced-order computational blood flow model which has been previously introduced [Itu et al., 2012]. The model was recently validated in clinical studies by comparing $cFFR_{CFD}$ against invasively measured FFR and the diagnostic accuracy for the detection of functionally significant CAD was shown to be good, i.e. between 75% and 85% [Coenen et al., 2015], [Renker et al., 2014], [Wang et al., 2015], [Baumann et al., 2015], [Coenen et al., 2016],] [De Geer et al., 2016], [Kruk et al., 2016].

The CFD approach employs numerical methods to compute time-varying flow and pressures using the principles of fluid dynamics by solving the reduced-order Navier-Stokes equations, with blood being modeled as an incompressible fluid with constant viscosity. For the healthy non-stenotic coronary arteries a reduced-order model is used in combination with a lumped parameter model for the coronary microvasculature [Mantero et al., 1992]. To enable accurate pressure computation in the stenotic regions for a given anatomical model, locally defined pressure drop models are embedded into the reduced-order blood flow model, leading to a modified hybrid reduced-order formulation. This is done to account for the complex shape of the stenosis and its impact on the pressure drop across the respective vessel segment. A systemic circulation model and a heart model are included to provide proper proximal and distal boundary conditions for the coronary circulation.

The boundary conditions are estimated based on allometric scaling laws that describe the relation between form and function, the resting total coronary flow is derived from the reference

radius values of the branches in the anatomical model [Chou et al., 2008], [Kassab, 2006]. The resting total coronary flow is distributed over the coronary anatomical model following Murray's law [Murray, 1926], and the total microvascular resistance at each outlet is determined [Sharma et al., 2012] with an automatic parameter estimation algorithm [Itu et al., 2015]. In the CFD model, the effect of adenosine is simulated by appropriately modifying the boundary condition, specifically by decreasing the total resistance of each coronary outlet [Wilson et al., 1990]. $cFFR_{CFD}$ is finally computed throughout the entire coronary artery tree as ratio of cycle-averaged pressure at the corresponding location and cycle-averaged aortic pressure.

6.2.3 Feature extraction and training of machine learning algorithm

The ML algorithm is used to compute $cFFR_{ML}$ at all locations along the centerline of the given coronary anatomical model. Hence, features are computed separately for each location along the centerline of the coronary geometries. Since the pressure and the flow rate at a certain location are influenced by both the upstream and the downstream circulation, the features used at each location encapsulate local, upstream and downstream information. Upstream information is extracted along the path of the parent segments. Downstream features are computed along the path of the main branch. This path is determined automatically from the healthy reference radius of daughter branches, the number of generations downstream, and the vessel length downstream.

The machine learning algorithm is trained using a deep neural network with 4 hidden layers (shown in Figure 6.3).

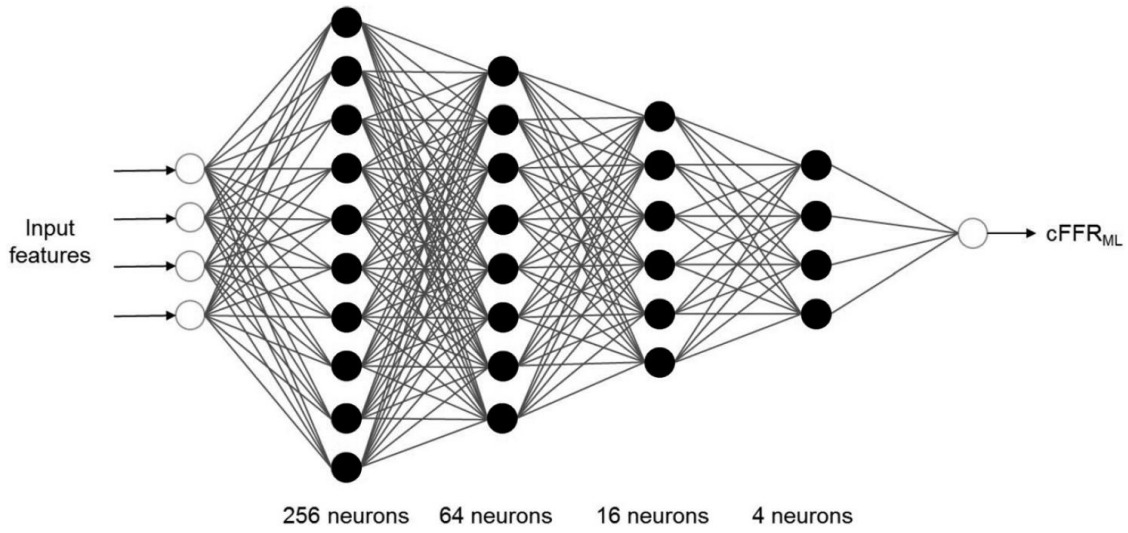

Figure 6.3: Deep-learning network architecture used for training the model. The network has 4 hidden layers, and uses a fully connected architecture.

A fully connected network model was used, i.e., each neuron in a layer is connected to all the neurons in the following layer, with no convolutional layers being used in this implementation. The input layer has 28 neurons corresponding to the different features computed from the coronary anatomy. The hidden layers contain 256, 64, 16 and 4 neurons respectively and use the sigmoidal activation function. Finally, the output layer has a single neuron with the linear activation function. To improve the model training time, each layer was initially pre-trained as an autoencoder. All the weights were initialized randomly (Xavier Initialization). The entire network is optimized using a mean-squared loss function with a Stochastic Gradient

Descent algorithm. A highly optimized GPU implementation was used to speed up the training process. The original feature set based on the synthetic coronary trees was randomized and split in a 5:1 ratio, and the smaller set was used for the validation of the results. In the model training process, the algorithm was never exposed to any patient data, with training and validation being done solely with the synthetic data. The model learning parameters like the learning rate, momentum, etc. were adaptively refined to control the model convergence behavior.

6.2.3.1 Local geometric features

At each spatial location, the local features used are the effective radius of the vessel, the reference radius of the branch and a segment-specific ischemic weight. The ischemic weight of each segment is a function of the set of reference radii of all the segments in the coronary tree, and is defined as the potential contribution of the segment to the total ischemic burden of the patient. This initial ischemic weight is afterwards adapted, as described further down.

6.2.3.2 Upstream and downstream geometric features

To compute the features upstream and downstream, first the stenoses upstream and downstream are identified. This is done with an automatic detection algorithm including all stenoses with a degree of radius reduction larger than 10%. The most significant four stenoses upstream and the most significant four stenoses downstream along the main branch path are selected. For each of these the following geometric features and their non-linear product combinations are extracted (Figure 6.4):

- Proximal, minimum and distal radius;
- Entrance length: length along the centerline between the start of the stenosis and the start of the segment with minimum radius;
- Minimum radius length: length along the centerline between the start and the end of the segment with minimum radius;
- Exit length: length along the centerline between the end of the segment with minimum radius and the end of the stenosis;
- Percentage diameter reduction:
- $$\%DR = \left(1 - \frac{r_{sten}}{(r_{prox} + r_{dist})/2}\right) \times 100$$

  where r_{sten} is the minimum radius of the stenosis, r_{prox} is the healthy radius proximal to the stenosis and r_{dist} is the healthy radius distal to the stenosis.

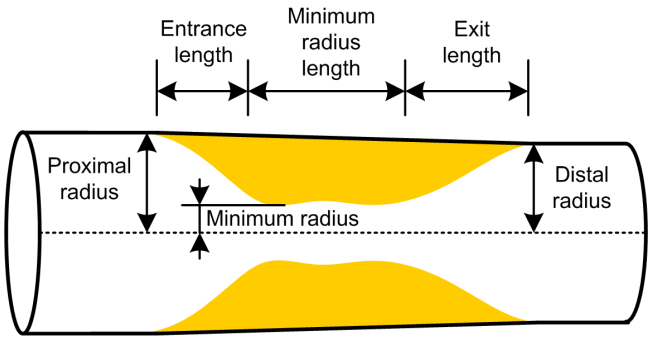

Figure 6.4: Stenosis specific features.

Note that the automatic detection algorithm identifies also very mild stenoses, which individually have a small effect on the flow characteristics, but, when aggregated, may have a significant effect. At each location, the aggregated values of the features described above were also computed at all upstream locations along the centerline, as well as the aggregated downstream values. In addition, the upstream and downstream coronary lengths are also used as features.

In the coronary circulation there is a significant degree of inter-dependence between branches. For example, in Figure 6.5a, the hemodynamics at points A and B are influenced by the stenosis on the side branch: the presence of the stenosis leads to a decreased flow, and hence to a lower pressure drop in the parent branch. This in turn influences the absolute pressure in the daughter branch to which point B belongs. Similarly, in Figure 6.5b the presence of the stenosis in the main branch influences the hemodynamics at point C: the stenosis leads to a lower flow and a lower pressure drop in the parent branch, and, thus, to different absolute pressure levels in the side branch.

To capture this inter-branch dependence, the machine learning model has functionality to adapt the initial ischemic weights of the coronary segments, computed as described above, to account for the interaction between different branches. Specifically, the ischemic weights are made dependent on the stenosis specific features on upstream, downstream and side branches.

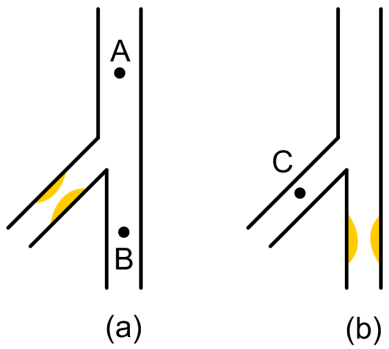

Figure 6.5: Flow interaction between vessels.

6.3 RESULTS

The methodology was validated in three different steps, which are presented below.

6.3.1 Validation of $cFFR_{ML}$ versus $cFFR_{CFD}$ on synthetic anatomical models

The 12000 synthetic geometries were randomly split into six sets, whereas five of them were used for training and one for testing. $cFFR_{ML}$ and $cFFR_{CFD}$ were compared at all locations in the testing set, and the correlation was excellent in all experiments ($r = 0.9998$, $p < 0.001$). There was no systematic bias between $cFFR_{ML}$ and $cFFR_{CFD}$ (mean difference was 0.0008). When $cFFR_{CFD}$ was considered as ground truth, with a cut-off of 0.8, $cFFR_{ML}$ predicted $cFFR_{CFD}$ with an accuracy of 99.7%.

6.3.2 Validation of $cFFR_{ML}$ versus $cFFR_{CFD}$ on patient specific anatomical models

A database of 87 patient-specific anatomical models generated from CT data using image segmentation, following a protocol described in [Coenen et al., 2015], [TRenker et al., 2014], was used. Invasive FFR was measured for 125 lesions in these 87 patients. The FFR

measurement locations were either determined from the angiogram images showing the pressure wire, or marked at a location that was approximately located 20 mm downstream from the stenosis [Pijls et al., 1996]. Correlation between $cFFR_{ML}$ and $cFFR_{CFD}$ was excellent (0.9994, $p < 0.001$) and no systematic bias was found in Bland-Altman analysis between $cFFR_{ML}$ and $cFFR_{CFD}$: mean difference was -0.00081 ± 0.0039, as shown in Figure 6.6 and Figure 6.7. The average computation time required for computing $cFFR_{ML}$ in the entire coronary tree of one patient was 2.4 ± 0.44 seconds, while the $cFFR_{CFD}$ computations required 196.3 ± 78.5 seconds, both on a 3.4 GHz Intel i7 8-core CPU.

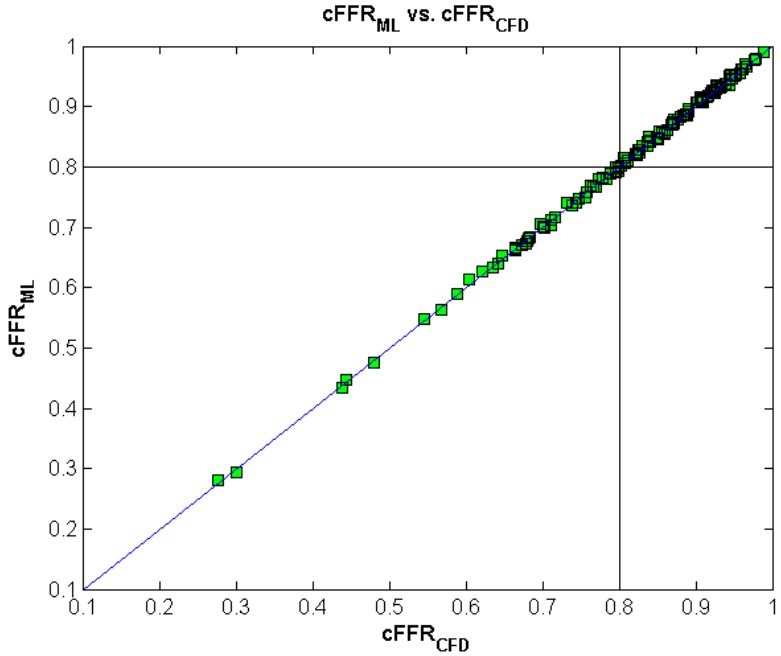

Figure 6.6: Scatterplot of $cFFR_{ML}$ and $cFFR_{CFD}$ (correlation = 0.9994).

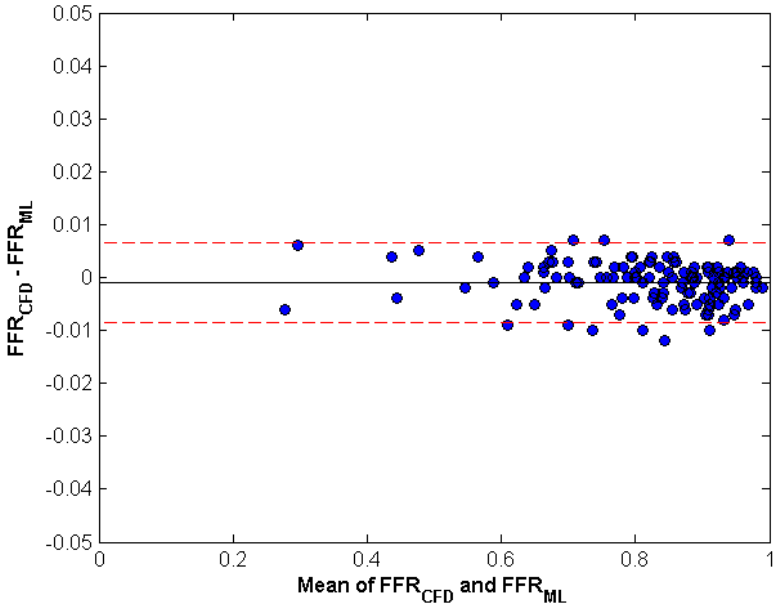

Figure 6.7: Bland-Altman analysis plot comparing $cFFR_{ML}$ and $cFFR_{CFD}$ shows no systematic bias (95% limits of agreement, -0.0085 to 0.0067).

Table 6.2 displays a more detailed analysis of the differences between $cFFR_{ML}$ and $cFFR_{CFD}$, where the lesions have been grouped in 5 different bins based on the $cFFR_{CFD}$ values (0.0 to 0.6, 0.6 to 0.7, 0.7 to 0.8, 0.8 to 0.9, and 0.9 to 1.0), either for all lesions, or separately for the three main branches: LAD, LCx and RCA. Although the mean difference slightly decreases with increasing $cFFR_{CFD}$ values, overall the variation is very small and the agreement between $cFFR_{ML}$ and $cFFR_{CFD}$ is high for all bins and all locations.

Table 6.2: Detailed analysis of the differences between $cFFR_{ML}$ and $cFFR_{CFD}$.

Lesions	$cFFR_{CFD}$ bin	Nr lesions	Mean differebce ± St. dev.
All	0.0 – 0.6	8	0.001 ± 0.004
	0.6 – 0.7	14	-0.001 ± 0.004
	0.7 – 0.8	23	0.000 ± 0.0040
	0.8 – 0.9	40	-0.001 ± 0.004
	0.9 – 1.0	40	-0.002 ± 0.003
LAD	0.0 – 0.6	6	0.000 ± 0.005
	0.6 – 0.7	10	-0.003 ± 0.004
	0.7 – 0.8	16	0.000 ± 0.004
	0.8 – 0.9	27	-0.002 ± 0.004
	0.9 – 1.0	20	-0.002 ± 0.003
LCx	0.0 – 0.6	2	0.002 ± 0.003
	0.6 – 0.7	1	0.002 ± 0.000
	0.7 – 0.8	4	0.001 ± 0.003
	0.8 – 0.9	5	-0.000 ± 0.003
	0.9 – 1.0	11	-0.003 ± 0.003
RCA	0.0 – 0.6	0	-
	0.6 – 0.7	3	0.003 ± 0.001
	0.7 – 0.8	3	0.000 ± 0.004
	0.8 – 0.9	8	0.001 ± 0.002
	0.9 – 1.0	9	0.001 ± 0.002

6.3.3 Diagnostic performance of $cFFR_{ML}$ and $cFFR_{CFD}$ versus invasive FFR

The same set of 87 patients was used to compare the performance of $cFFR_{ML}$ against invasively measured FFR. Invasive FFR ≤ 0.80 was regarded as criterion for positive ischemia, and was found in 38 lesions out of 125. For $cFFR_{ML}$, sensitivity was 81.6%, specificity 83.9%, and accuracy 83.2%. Table 6.3 displays the diagnostic performance of $cFFR_{CFD}$ and $cFFR_{ML}$ versus invasively measured FFR with corresponding 95% confidence intervals. The overall correlation between $cFFR_{ML}$ (0.814 ± 0.135) and invasive FFR (0.838 ± 0.11) was 0.729 ($p < 0.001$).

Figure 6.8 displays the scatter plots of $cFFR_{CFD}$ and $cFFR_{ML}$ versus invasive FFR, while Figure 6.9 displays the Bland-Altman analysis between $cFFR_{CFD}$/$cFFR_{ML}$ and invasive FFR. The close overlap between the two methods further demonstrates the statistical equivalence of the two approaches.

Table 6.3: Diagnostic parameters in all vessels (N = 125); a positive event, representing a significant stenosis, is defined by invasive FFR ≤ 0.80. $cFFR_{CFD}$ diagnostic parameters are obtained with the CFD algorithm, $cFFR_{ML}$ diagnostic parameters are obtained with the ML algorithm.

	$cFFR_{CFD}$	$cFFR_{ML}$
True positive	31	31
False positive	14	14
True negative	73	73
False negative	7	7
Sensitivity	81.6% (66.6%–90.8%)	81.6% (66.6%–90.8%)
Specificity	83.9% (74.8%–%90.1)	83.9% (74.8%–%90.1)
PPV	68.9% (54.3%–%80.2)	68.9% (54.3%–%80.2)
NPV	91.2% (83.2%–%95.7)	91.2% (83.2%–%95.7)
Accuracy	83.2% (75.6%–%88.7)	83.2% (75.6%–%88.7)
Correlation	0.725	0.729
Mean ± St. dev.	0.814 ± 0.135	0.815 ± 0.135

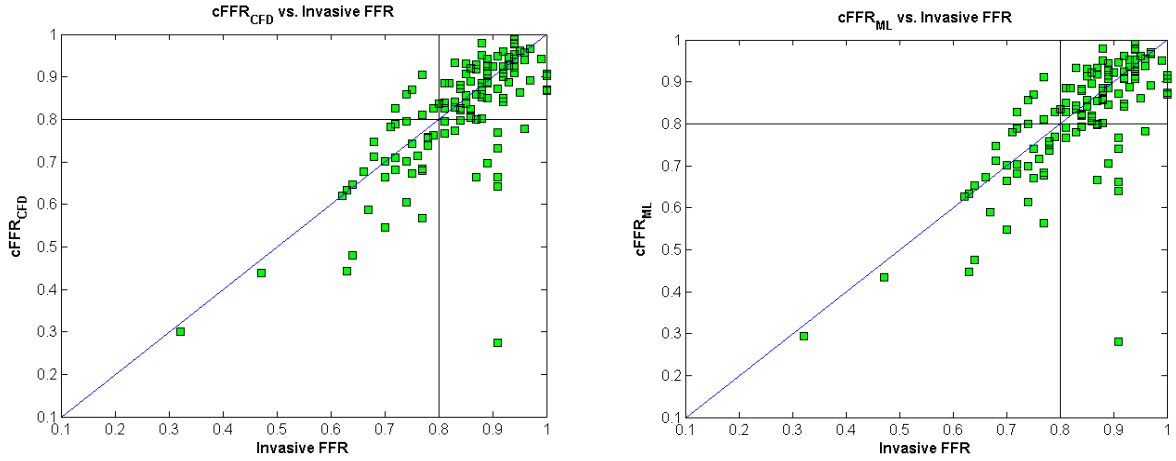

Figure 6.8: (a) Scatterplot of $cFFR_{CFD}$ and invasive FFR (correlation = 0.725); (b) Scatterplot of $cFFR_{ML}$ and invasive FFR (correlation = 0.729).

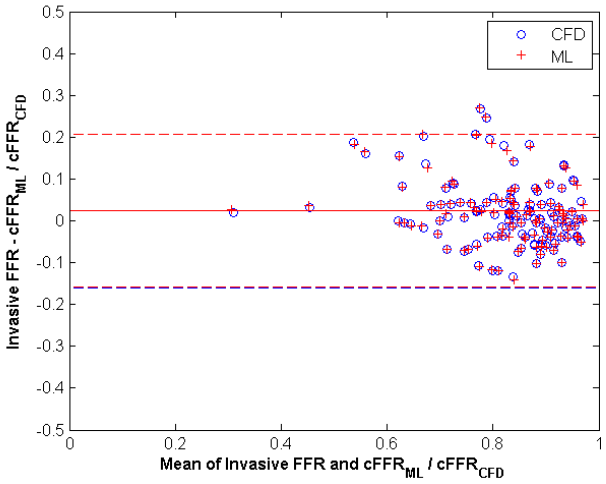

Figure 6.9: Bland-Altman analysis plot comparing $cFFR_{CFD}$ and $cFFR_{ML}$ vs. invasive FFR ($cFFR_{CFD}$ 95% limits of agreement, -0.159 to 0.207; $cFFR_{ML}$ 95% limits of agreement, -0.159 to 0.206).

In Figure 6.10, Figure 6.11, Figure 6.12 representative case examples are shown, illustrating the almost perfect agreement between the two algorithms at each point on the coronary tree. The receiver-operator characteristic (ROC) curves for $cFFR_{CFD}$ and $cFFR_{ML}$ are presented in Figure 6.13. The area under the curve (AUC) was 0.90 for both $cFFR_{CFD}$ and $cFFR_{ML}$.

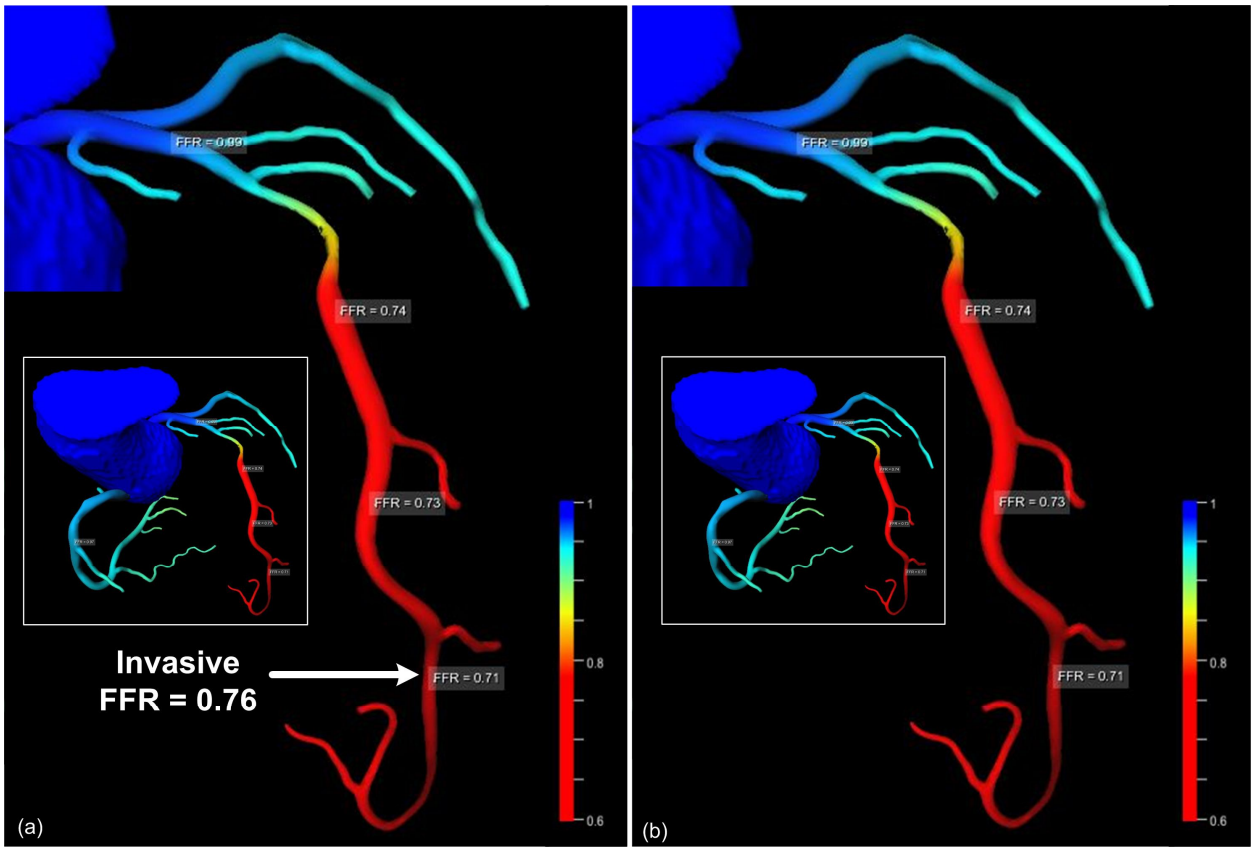

Figure 6.10: Case example of a coronary anatomical model reconstructed from CT data: (a) $cFFR_{CFD}$ map of the entire coronary tree, including a close-up view of the LAD, with invasive FFR = 0.76 and $cFFR_{CFD}$ = 0.71 (b) $cFFR_{ML}$ map of the entire coronary tree, including a close-up view of the LAD, with $cFFR_{ML}$ equal to cFFRCFD at the invasive FFR measurement location.

6.4 DISCUSSION

Similarly to previously published approaches based on computational modeling, the approach introduced herein provides a non-invasive assessment of FFR from routinely performed CCTA scans. This methodology represents the only currently available solution for non-invasive, near real-time computation of FFR in the entire coronary tree. Other approaches reported in literature required several minutes [Renker et al., 2014] to several hours [Norgaard et al., 2014] for the execution of the FFR algorithm. The approach is potentially well-suited for a clinical setting since it is computationally efficient both in terms of execution speed and hardware requirements, and is based on anatomical data acquired from routine CCTA. The diagnostic accuracy of the algorithm (83%) is in the same range as that of previously published data on FFR computed from CCTA images, which varied from 73% to 85% [Coenen et al., 2015], [Koo et al., 2011], [Min et al., 2012], [Norgard et al., 2014], [Renker et al., 2014], [De Geer et al., 2006], [Kruk et al., 2016].

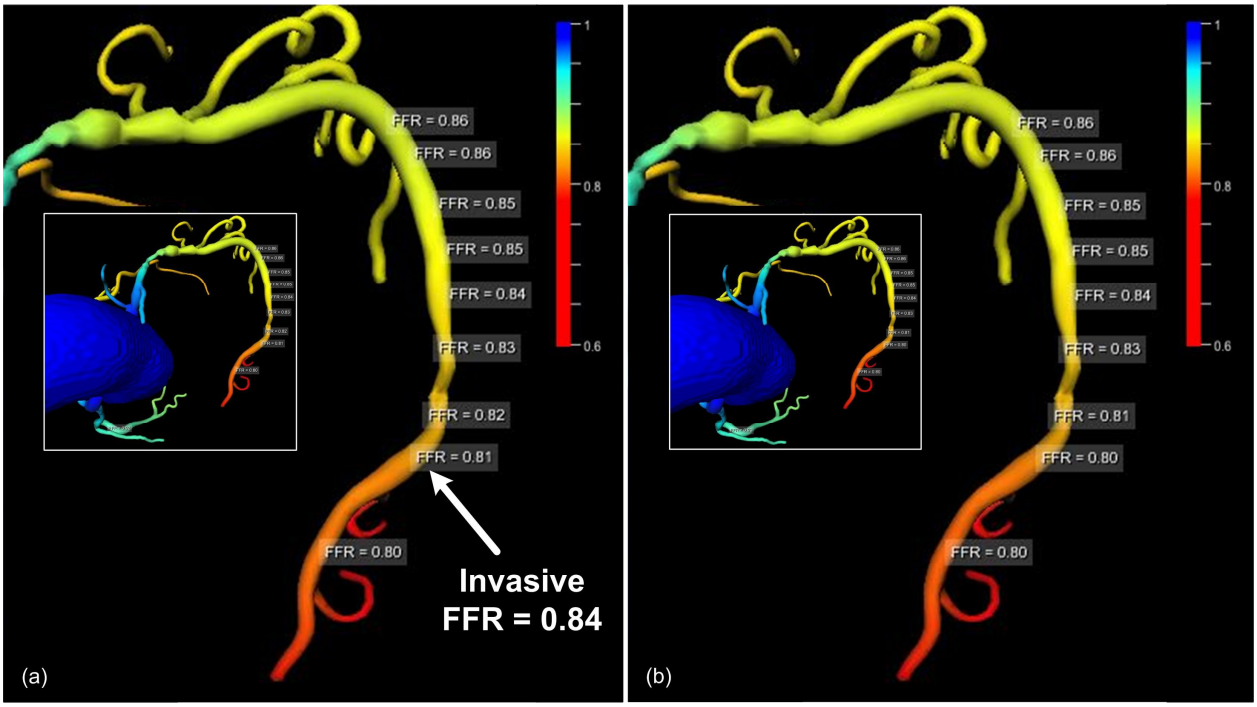

Figure 6.11: Case example of a coronary anatomical model reconstructed from CT data: (a) $cFFR_{CFD}$ map of the entire coronary tree, including a close-up view of the RCA, with invasive FFR = 0.84 and $cFFR_{CFD}$ = 0.81 (b) $cFFR_{ML}$ map of the entire coronary tree, including a close-up view of the RCA, with $cFFR_{ML}$ = 0.80 at invasive FFR measurement location.

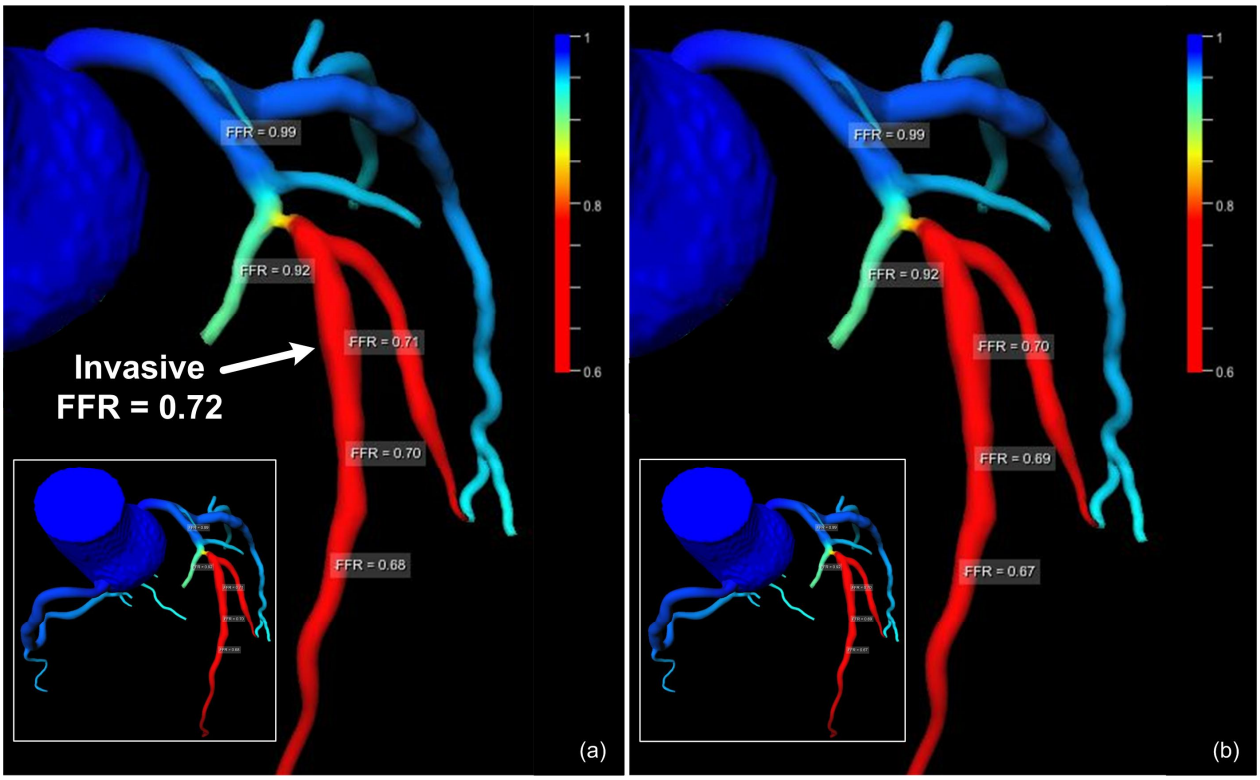

Figure 6.12: Case example of a coronary anatomical model reconstructed from CT data: (a) $cFFR_{CFD}$ map of the entire coronary tree, including a close-up view of the LAD, with invasive FFR = 0.72 and $cFFR_{CFD}$ = 0.71 (c) $cFFR_{ML}$ map of the entire coronary tree, including a close-up view of the LAD, with $cFFR_{ML}$ = 0.70 at invasive FFR measurement location.

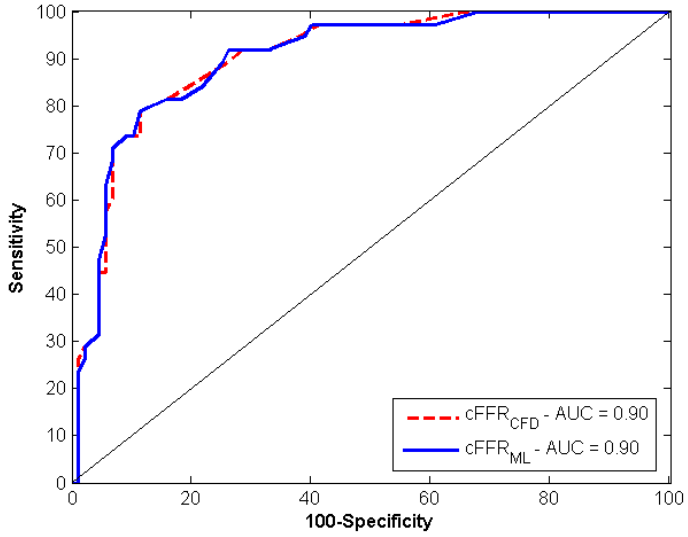

Figure 6.13: Receiver operating characteristic (ROC) curves for 189 vessels, as obtained with $cFFR_{CFD}$ and $cFFR_{ML}$.

As more data is emerging from such studies, the incremental diagnostic value of computed FFR over the traditional CCTA based visual or quantitative lesion grading is becoming more evident. As a result, this technology has the potential to further strengthen the role of CCTA as a gatekeeper to the catheterization lab.

Previous studies have tried to assess the functional significance of CAD from geometric features of the stenosis, with limited success [Ben-Dor et al., 2011], [Gonzalo et al., 2012], [Koo et al., 2011]. Herein, however, a comprehensive set of geometric features describing not only the stenotic region, but the entire coronary arterial tree, was used. Combined with state-of-the-art machine learning techniques, this approach demonstrates that geometric features alone can be used as predictors of patient-specific hemodynamic states, without the need of explicitly solving the hemodynamics equations.

The key ingredients for the design of this machine learning method are the availability of a comprehensive database of training data, as well as the proper selection of features that are most significant for the predicted quantity. In an ideal scenario, the training database would consist of thousands of anatomical models extracted from CCTA images, accounting for the variability of coronary vessels across different patient populations, and the corresponding invasive FFR measurement of each lesion. From a practical point-of-view, establishing such a large database would be prohibitively expensive and time-consuming.

To address this issue, the concept of a training database consisting of synthetically generated vascular geometries representing the coronary tree was introduced, and corresponding FFR values computed from a CFD algorithm at all locations of the coronary tree. The synthetic database is parameterized on the morphological features of the vascular tree, allowing the proper sampling of relatively uncommon configurations such as serial stenoses, multi-branch stenoses, bifurcation stenoses, diffuse disease, or rare pathological conditions. After training, the machine learning algorithm encodes the correlation between the set of chosen geometric features and the quantity of interest, herein FFR, predicted by the validated CFD model. In the population on which the algorithm was tested, the patient anatomical features were well within the region of high-confidence for the machine learning algorithm.

This approach can also be extended to compute other hemodynamic quantities, such as coronary flow reserve (CFR), rest Pd/Pa [Kern, 2000], the instantaneous wave-free ratio (iFR) [Sen et al., 2012], hyperemic/basal stenosis resistance (HSR/BSR) [Meuwissen et al., 2012], [van de Hoef et al., 2012], or shear stress [Smady et al., 2011], each of which can be used as a ground-truth in the training database.

Additionally, the set of features can be expanded to include other characteristics of the vascular tree, e.g. plaque composition, or even information such as the clinical history of the patient that could play a role in determining the functional significance of a lesion and its stability over time [Pijls, 2007].

It should be noted that the presented approach is generic with respect to the CFD model used for training the algorithm. For this work, a reduced-order CFD approach was used to generate the training database.

On the other hand, these results also point to the fact that the accuracy of $cFFR_{ML}$ will depend on the accuracy of the CFD model used in the training phase. In general terms, the performance of this method is expected to be statistically equivalent to that of the CFD model.

Since the machine learning algorithm computes cFFR at all locations of a coronary tree, a natural extension of this work is to generate virtual pull-back curves, where the variation of cFFR along a path from ostium to a distal coronary location is depicted. Such an analysis could be useful for determining the most significant lesion in case of serial stenoses.

The study has a number of limitations. Since the proposed machine learning algorithm learns the output of a computational blood flow model, with almost perfect results, the limitations are mainly given by the limitations of the blood flow model. First of all, although the set of patient geometries used herein comprises a significant amount of lesions, further clinical studies are required for extensive validation of the methodology. In the current study the majority of lesions had an invasive FFR between 0.7 and 1.0 (only 11 lesions had an FFR < 0.7) and further validation of the model is required under different conditions. However, the most difficult lesions in terms of classification are those which are close to the cut-off value of 0.8. In this regard, one interesting study based was recently conducted [Kruk et al., 2016]: $cFFR_{CFD}$ thresholds of 0.74 and 0.87 were determined for which PPV and NPV respectively were both >90%. Hence, in the proposed hybrid approach $cFFR_{CFD} > 0.87$ was used to defer revascularization, $cFFR_{CFD} < 0.74$ to confirm treatment, whilst lesions with intermediate $cFFR_{CFD}$ values were classified based on invasive FFR. The hybrid approach resulted in an overall 95% agreement with the FFR-only strategy, and would potentially obviate the need for invasive pressure measurements in 50% of the patients.

Secondly, the definition of the parameters of the blood flow model uses physiological assumptions, which would also require validation on larger data sets. Such assumptions include for example the allometric scaling laws applied for estimating the flow rate distribution, the effect of hyperemia (for patients with microvascular disease, the decreased effect of a hyperemia inducing drug may lead to an underestimation of the FFR value), the use of population-averaged rheological properties of the blood etc. Moreover, the collateral circulation has not been taken into account. Collaterals can have a significant impact on the hemodynamics, especially for very severe lesions.

Properties of blood, such as density and viscosity also influence the pressure losses. This dependence has not affected the comparison between CFD and machine learning results in this chapter, since the same constant density and viscosity were used for the CFD computations in

synthetic and patient-specific geometries. Such parameters can also be easily incorporated into the machine learning model by appropriately sampling over these variables in the synthetic database.

The models used for generating the synthetic coronary trees are representative of many commonly occurring clinical cases. However, the database as used in this chapter does not contain less frequent pathological conditions, like anomalous origin of the coronary arteries and coronary artery aneurysms. Further, the shapes of the stenosis used to generate the synthetic vessel trees are of a smooth nature and do not account for the noise typically found in medical images. In future work, the augmentation of the database with noisy variants of the geometries will be of interest.

Finally, an important limitation in leveraging the real-time capabilities of the algorithm is the time required for data preparation, i.e. the generation of the coronary anatomical model, which varies between 10 and 60 minutes. In this study, the time spent in model preparation (i.e., lumen segmentation) was not systematically evaluated, but in a different pre-clinical study using the same pre-processing pipeline as the one used in this chapter [Renker et al., 2014], a total processing time of 37.5 ± 13.8 minutes was reported. Future work will focus on a significant speed up of this step to mitigate this limitation.

7. GPU Accelerated Geometric Multigrid Method: Comparison with Preconditioned Conjugate Gradient

7.1 INTRODUCTION

Computational science is one of the main targets for high performance computational approaches. Scientific computations heavily rely on numerical methods, and in many of these applications the most time-consuming step is the solution of large linear systems of equations [Feng et al., 2012]. These systems are generated by discretizing complex partial differential equations (PDEs), for which no analytical solution exists. Hence, the resulting systems of equations are sparse, and require specialized algorithms for efficient solutions. Moreover, the Poisson equation is the most often encountered type of equation, and, thus, a fast Poisson solver is crucial for an efficient solution scheme [Xu, 2010]. The Poisson equation is based on the Laplace operator and models various physical phenomena such as electrostatics, wave propagation, gravitational potential and computational fluid dynamics [Köstler et al., 2008], [Shi et al., 2009], [Sturmer et al., 2008].

The two most popular algorithms for the solution of the Poisson equation are the preconditioned conjugate gradient method (PCG) [Gui et al., 2012] and the multigrid method (MG) [Briggs et al., 2000], [Trottenberg et al, 2000], in its two variants geometric MG (GMG) and algebraic MG (AMG). All these methods rely on iterative solution schemes, which are faster than direct solution schemes for large systems of equations [Feng et al., 2012]. The PCG method

is regularly used for solving sparse symmetric positive definite linear systems, it is easy to implement, and converges in at most *n* steps to the solution (*n* is the size of the system) [Ament et al., 2010].

Originally, multigrid methods were developed to solve boundary value problems posed on spatial domains. Such problems were discretized by choosing a set of grid points in the domain of the problem. More recently, the original multigrid approach has been abstracted to problems in which the grids have been replaced by more general levels of organization [Briggs et al., 2000]. The multigrid method is based on a hierarchy of discretization levels, whereas the corrections performed at the coarser discretization levels improve the convergence rate of the solution on the finest discretization level. The GMG method requires specific information on the hierarchy of discretizations, but, if this information is available, it is considerably more efficient than the AMG method [Ruge et al., 1987].

Graphic Processing Units (GPUs) are dedicated processors, designed originally as graphic accelerators. Since CUDA (Compute Unified Device Architecture) was introduced in 2006 by NVIDIA as a graphic application programming interface (API), the GPU has been used increasingly in various areas of scientific computations due to its superior parallel performance and energy efficiency.

When a GPU is programmed through CUDA, it is viewed as a compute device, which is able to run thousands of threads in parallel by launching a kernel (a function, written in C language, which is executed by the threads on the GPU) [Zou et al., 2009]. GPU based applications are run in a CPU-GPU tandem manner [Ryoo et al., 2008], whereas the CPU, usually called host, launches the main application, and allocates and initializes the data. Then, the buffers are transferred to the global memory of the GPU and the CPU calls the kernel which performs the computations on the GPU. Finally, the results are copied back to the CPU, which performs post-processing tasks.

Due to its very efficient performance-cost ratio, and its widespread availability, the GPU is currently the most used massively parallel processor [Itu et al., 2013(b)]. GPU-based implementations of PCG and MG methods have been recently introduced and analyzed. Most of the PCG oriented researches have focused on efficient preconditioners, since the preconditioning step is time consuming and difficult to parallelize. Specifically, a specialized preconditioner based on a matrix-vector multiplication operation, which is particularly well suited for the GPU architecture was introduced [Labutin et al., 2013]. Furthermore, a new diagonal storage format for the preconditioner was proposed [Gui et al., 2012]. Ament et al. have addressed a multi-GPU configuration with special focus on reducing the effect of data transfer between GPUs [Ament et al., 2010]. Another efficient solution for very large sparse linear systems of equations, i.e. which do not fit into the global memory of a single GPU, has been recently proposed [Nita et al., 2014]. In the category of GMG oriented researches, Singh has analyzed the effect of different optimization techniques and has compared the performance of the GPU-based algorithm against various CPU-based implementations [Williams et al., 2012]. A similar analysis was performed for finite element solvers, and, again, the GPU-based implementation performed best [Geveler et al., 2013]. Since the smoothing step of the GMG algorithm occupies most of the execution time, many activities have focused on developing more advanced smoothers. For example, a block-asynchronous smoother that performs more flops in order to reduce synchronization, and hence data transfer operations, has been proposed [Anzt et al., 2012].

All the above mentioned researches have demonstrated that the GPU-based implementation of the GMG outperforms its CPU-based counterpart. Hence, in this chapter a more in-depth analysis of the GPU-based GMG algorithm is performed [Stroia et al., 2015]. Specifically different GMG variants, different discretization schemes for the Poisson equation, and varying number of smoothing steps during restriction and prolongation are employed, and single and double precision computations, and different discretization resolutions are used. Finally, the performance gap between the GMG method and the PCG method on a state-of-the-art GPU is determined.

7.2 METHODS

7.2.1 Preliminaries

To study the performance of the GMG method the Poisson equation is considered:

$$\begin{cases} \Delta u = f & in \quad \Omega \\ u = u_{BC} & on \quad \partial\Omega \end{cases} \tag{7.1}$$

where u is a scalar and unknown, Ω is the domain on which the equation is solved ($\Omega \subset R^d$), u_{BC} is the value of the unknown on the boundary of the domain (Dirichlet type boundary condition), and f is a scalar. Through discretization a sparse linear system of equations is obtained:

$$A\bar{u} = \bar{f}, \tag{7.2}$$

where $\bar{u}$ and $\bar{f}$ are the discretized counterparts of u and f. To address the aspects mentioned in the introduction, in the following reference is made specifically to the steady-state heat conduction problem and a finite difference method is applied for its discretization in a three-dimensional domain. A uniform mesh of points is used, and, by applying central differencing, three different discretization schemes are considered, leading to:

- a 7-point stencil:

$$T_{i+1,j,k} + T_{i-1,j,k} + T_{i,j+1,k} + T_{i,j-1,k} + T_{i,j,k+1} + T_{i,j,k-1} - 6T_{i,j,k} = 0 \tag{7.3}$$

- a 19-point stencil:

$$\begin{aligned} &T_{i,j,k-1} + T_{i-1,j,k-1} + T_{i+1,j,k-1} + T_{i,j-1,k-1} + T_{i,j+1,k-1} + T_{i-1,j,k} + T_{i+1,j,k} + T_{i,j-1,k} + T_{i,j+1,k} + T_{i-1,j-1,k} + \\ &+ T_{i-1,j+1,k} + T_{i+1,j-1,k} + T_{i+1,j+1,k} + T_{i,j,k+1} + T_{i-1,j,k+1} + T_{i+1,j,k+1} + T_{i,j-1,k+1} + T_{i,j+1,k+1} - 18T_{i,j,k} = 0 \end{aligned} \tag{7.4}$$

- a 27-point stencil:

$$\begin{aligned} &T_{i,j,k-1} + T_{i-1,j,k-1} + T_{i+1,j,k-1} + T_{i,j-1,k-1} + T_{i,j+1,k-1} + T_{i-1,j-1,k-1} + T_{i-1,j+1,k-1} + T_{i+1,j-1,k-1} + T_{i+1,j+1,k-1} + T_{i-1,j,k} + \\ &+ T_{i+1,j,k} + T_{i,j-1,k} + T_{i,j+1,k} + T_{i-1,j-1,k} + T_{i-1,j+1,k} + T_{i+1,j-1,k} + T_{i+1,j+1,k} + T_{i,j,k+1} + T_{i-1,j,k+1} + T_{i+1,j,k+1} + T_{i,j-1,k+1} \\ &+ T_{i,j+1,k+1} + T_{i-1,j-1,k+1} + T_{i-1,j+1,k+1} + T_{i+1,j-1,k+1} + T_{i+1,j+1,k+1} - 26T_{i,j,k} = 0 \end{aligned} \tag{7.5}$$

where an isotropic discretization was considered ($\Delta x = \Delta y = \Delta z$) and $T_{i,j,k}$ represents the temperature value at the grid point (i, j, k).

As described in the previous section, geometric multigrid methods (GMG) refer to a group of algorithms for solving differential equations using a hierarchy of discretizations (Figure 7.1).

The discretization (eqs. (7.3) / (7.4) / (7.5)) is applied for different grids, whereas the grids have successively larger spacing between the nodes. All GMG variants are based on successive transitions from fine to coarse grids and back. Hence, the basic steps of the GMG method are:

- Relaxation (smoothing): a simple iterative method like Jacobi or Gauss-Seidel is used to reduce the high frequency errors in the solution;
- Restriction: the residual determined on a finer grid is downsampled to a coarser grid;
- Prolongation: the residual on a finer grid is determined by interpolating the values from the coarser grid.

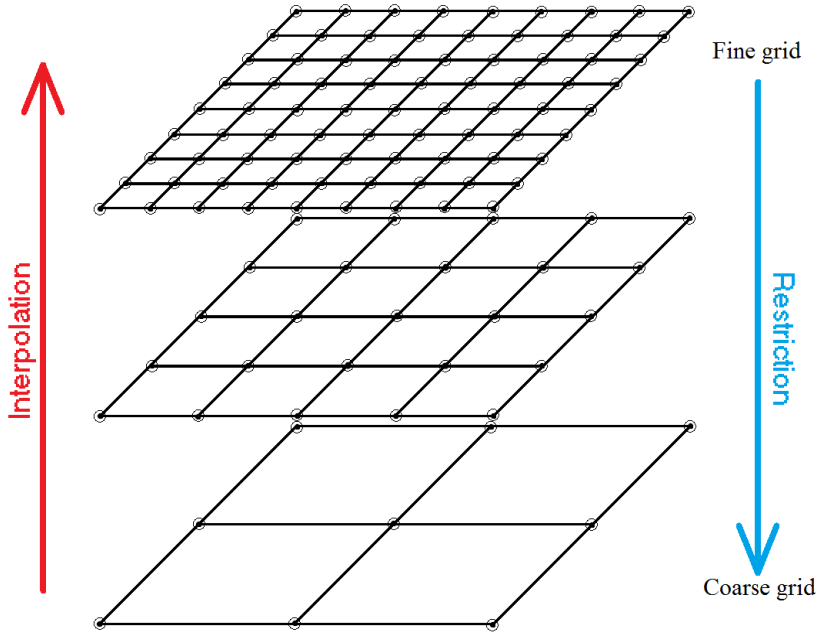

Figure 7.1: Basic concept of the geometric multigrid method: the solution is iterated through different discretization levels.

The relaxation methods employed herein are red-black Gauss-Seidel (RBGS) for the 7-point stencil [Vizitiu et al., 2014], and Jacobi for the 19-point and 27-point stencils [Chung, 2010]. The red-black Gauss-Seidel method requires one array for storing the values, but the computations are divided into two sequential steps: grid nodes are marked as being *red* or *black*, whereas all neighbors of a node have the opposite color of the current node. Hence, when updating the values of the red nodes only values at black nodes are used, and vice-versa. The Jacobi method uses only values from the previous iteration and hence only one computation step is required at each iteration, but two different arrays are allocated for storing the previous and the current values at the grid nodes.

The GMG variants considered in this chapter are displayed in Figure 7.2: V-cycle, W-cycle and full MG (FMG) scheme. Each figure depicts the strategy for a single iteration (multiple iterations are required to converge to the final solution). Whereas for the V and W schemes an iteration starts from the finest level, for the FMG scheme an iteration starts from the coarsest level. Before the finest level is reached, the scheme returns several times back to the coarsest level. Moreover, once the finest level is reached, a V-cycle is performed to finalize the iteration.

An optimized GPU-based implementation of the preconditioned conjugate gradient (PCG) method is used for comparison [Nita et al., 2014]. Whereas GMG is based on an explicit solution scheme, the PCG method employs an implicit solution scheme for solving sparse linear systems of the form $Ax = b$, where x is the vector of unknown, A is a matrix with coefficients given by the discretization, and b is the right hand side vector determined by f and u_{BC} in (7.1).

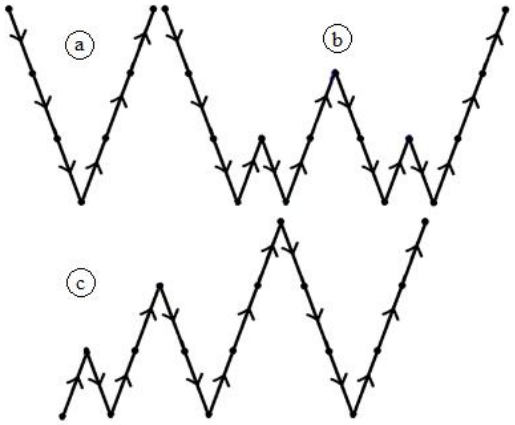

Figure 7.2: Geometric Multigrid variants: (a) V-cycle; (b) W-cycle; (c) Full MG (FMG).

7.2.2 GPU Accelerated Geometric Multigrid

The implementation of the V-cycle and W-cycle GMG variants are based on the μ-Cycle algorithm (algorithm 1), which is a recursive scheme. The only difference is given by the parameter μ, which dictates how many times a new function will be launched: for the V-cycle μ = 1, whereas for the W-cycle μ = 2. When it is first launched, the algorithm starts at level 0, and, every time a new function is launched, a coarser grid is used [Briggs et al., 2000]. The values n_1, n_2, n_3 determine the number of smoothing steps on the descending branch, at the coarsest level, and respectively on the ascending branch. Additionally to the prolongation step, on the ascending branch, a correction is employed: the values on the destination level are corrected based on the interpolated values computed from the source level (a matrix-sum operation is performed).

Algorithm 1. μ-Cycle

```
μ-Cycle(level)
    if( level is coarsestLevel )
        apply n2 smoothing steps
    else
        apply n1 smoothing steps
        compute residual
        restrict to a coarser grid
        μ-Cycle(level+1) μ times
        prolongate
        correct
        apply n3 smoothing steps
    end
```

The multigrid method requires one storage array for each level (level 0 uses the largest array and occupies most of the execution time). At the coarsest level (level L) a 3D grid with 3x3x3 nodes is used. Dirichlet boundary conditions were considered, and, hence, the values on all faces of the domain are known (the values on five faces are set to 0, and one face to a non-zero value). If n is the number of nodes in one direction at a given discretization level, the number of nodes with unknown values is equal to:

$$N = (n - 2)^3. \tag{7.6}$$

Each operation in algorithm 1 uses a separate kernel. For the red-black Gauss-Seidel smoother $N/2$ computations can be safely performed in parallel, and, hence, a kernel with three-dimensional thread organization and a total of $N/2$ threads is launched twice for each smoothing step. For the Jacobi smoother N threads are launched and the kernel is executed exactly once at each smoothing step.

The thread organization of the restriction and prolongation operators, which perform the transition from one level to another, is slightly different. If the transition is performed from level i to level $i+1$ (restriction) $N_{i+1} = (n_{i+1} - 2)^3$ threads are created. If the transition is performed from level $i+1$ to level i (prolongation) $N_i = (n_i - 2)^3$ threads are created. Hence, the destination level determines the number of threads to be launched.

To compare the numerical results and the execution time of GMG and PCG, the same residuals are computed for both methods. For the PCG method only the finest discretization level is considered and the $n \times n \times n$ unknowns are organized into a vector of unknowns, x, of size $N_{PCG} = n \times n \times n$. Hence, matrix A is of size $N \times N$, while b has the same size as x. The residuals are computed using:

$$r = Ax - b. \tag{7.7}$$

7.3 RESULTS

To evaluate the performance of the GPU based GMG implementation a NVIDIA GeForce GTX Titan Black graphics card was used, together with the CUDA toolkit version 6.0. The steady-state heat conduction problem was solved on a rectangular domain, and the Dirichlet boundary conditions, were set to 0^0C for five facets and to 100^0C for the remaining facet. The numerical solution was obtained on a grid of 129x129x129 nodes. Different numbers of smoothing steps were considered at different levels of the GMG method. Each configuration is described by a three-figure number (e.g. 213 – Figure 7.3): the first value determines the smoothing steps while restricting the grid, the second value determines the smoothing steps at the coarsest level, while the third number determines the smoothing steps while prolongating. All computations are performed in double precision and use the 7-point stencil when not otherwise stated, and iterations are performed until the average residual value no longer decreases from one iteration to the next (a value close to the limit of the corresponding floating point representation limit is reached).

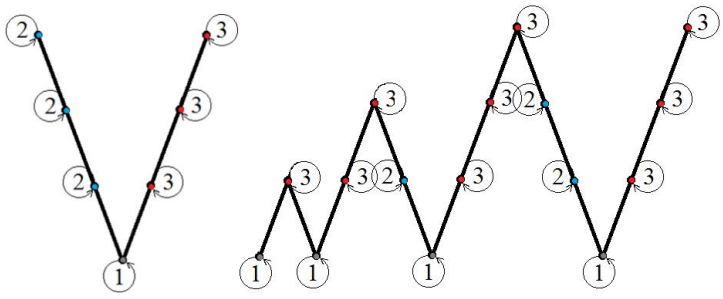

Figure 7.3: A 213 sample smoothing configuration.

First, the different GMG schemes are compared (V-cycle, W-cycle and FMG) in a 313 configuration with red-black Gauss-Seidel smoother. Figure 7.4 displays the dependence between the execution time and the average residual. The V-cycle scheme performs best:

although it requires more iterations than the W and FMG schemes (13 iterations for V, 8 iterations for W, 11 iterations for FMG), the average residual decreases to 1e-14 in the shortest amount of time. Hence, for the following steps results are presented for the V-cycle scheme.

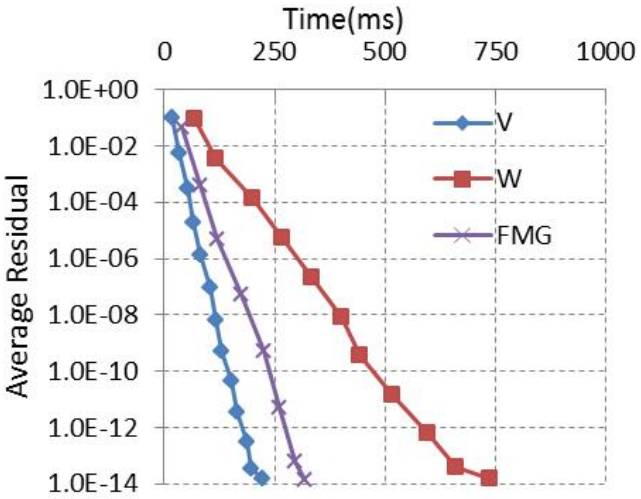

Figure 7.4: Comparison of different GMG schemes (V, W, FMG) when the RBGS smoother is used.

Next, the effect of the smoothing configuration is analyzed (for a RBGS smoother). Figure 7.5 displays the four best performing configurations: two or three smoothing steps are required during restriction and prolongation, while only one smoothing step is required at the coarsest level. From the four depicted strategies, 212 and 312 perform best: 212 is slightly faster but requires one more iteration to reach an average residual of 1e-14 (11 vs 10 iterations), leading to approximately the same execution time. If fewer than two smoothing steps are applied during restriction and prolongation the number of iterations increases considerably, and outweighs the time saving given by the fewer smoothing steps. If more than three smoothing steps are applied, the execution time of each iteration increases, and outweighs the time saving given by the fewer number of iterations.

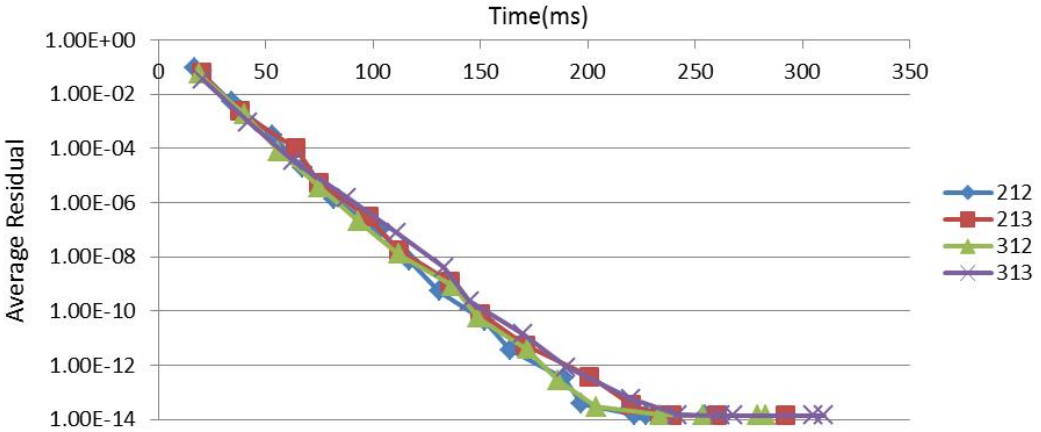

Figure 7.5: Effect of smoothing steps on the performance of the GMG method.

In the following the effect of the floating precision on the performance of the GMG method is analyzed (Figure 7.6). Single and double precision were considered, in combination with the best performing smoothing configurations (212 and 312). The average residual in single

precision is limited to approx. 1e-5, whereas in double precision it decreases to 1e-14. The residual of 1e-5 is reached slightly faster in single precision since the GTX Titan Black card has a higher GFLOP processing power in single precision than in double precision. The difference is however small, and, since most scientific computation applications require high accuracy, double precision should be used. Next, the relative execution time used by each operation in the GMG algorithm is analyzed (Table 7.1). The smoothing step is the most expensive operation, occupying almost half of the execution time. Moreover, the transition from the coarser grid to the finer grid (prolongation + correction) is costlier than the transition from the finer grid to the coarser grid (restriction + residual computation). This is given by the fact that during prolongation the destination levels are finer than during restriction (e.g. the finest grid level is only used at prolongation).

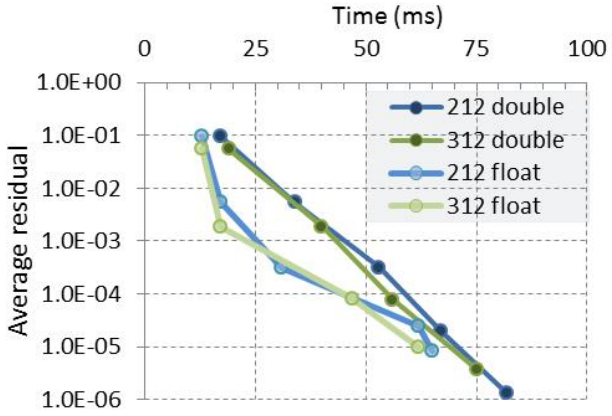

Figure 7.6: Effect of floating point precision on the performance of the GMG method.

Table 7.1: Percentage of execution time occupied by each GMG operation.

Operation	% of Exec. time
Smoother	46.7%
Prolongation	26.7%
Residual computation	14.4%
Correction	6.1%
Restriction	5.9%
Memset(0)	0.2%

Another important aspect is the effect of the stencil configuration on the performance of the GMG method (Figure 7.7). The 7-point stencil with RBGS smoother and the 19-point and 27-point stencil with Jacobi smoother were considered. The 19-point and 27-point stencils require 40% and respectively 155% more execution time to reach a similar level of accuracy. However, opposed to the analysis performed for different GMG schemes, different number of smoothing steps, and single / double floating point precision were used, one cannot state that one approach performs better than the others. Practically, for each stencil configuration a different problem is solved: although the analytical equations are the same, the different discretization schemes lead to different numerical equations. Hence, although the 27-point stencil leads to the largest execution time, its numerical solution has the highest numerical accuracy. This numerical

accuracy should not be confounded with the residuals computed in (7.7), which are specific for each discretization scheme. The stencil choice is a trade-off between execution time performance and numerical accuracy.

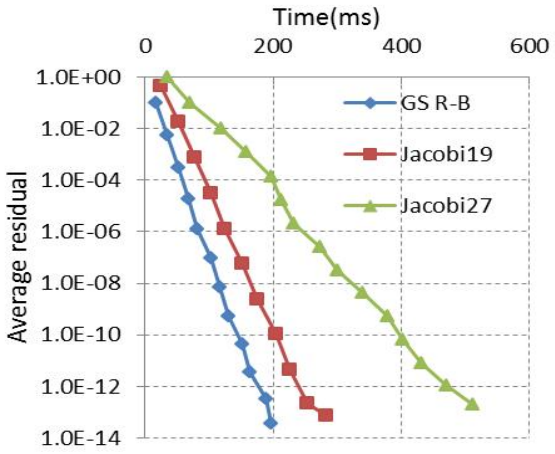

Figure 7.7: Effect of stencil configuration on GMG performance.

Finally, the performance of the best performing GMG variant is compared (V-cycle, 312 smoothing steps) with the optimized PCG method, in double precision. Different fine grid resolutions were considered and the three different discretization schemes. The results in Table 7.2 indicate that on the fine grid of 129x129x129 GMG offers a speed-up of 7.1x-9.2x over PCG, while it also leads to a smaller average residual. The speed-up is smaller on the intermediate grid, while on the coarse grid, PCG performs slightly better. This is given by the fact that for GMG the parallelism on the coarse grid (33x33x33) is limited, whereas for PCG the size of matrix *A* is still large enough to utilize the computational power of the GPU. In practice, typically used grids have more than 1 million nodes, case in which the GPU based GMG implementation performs better than the GPU based PCG implementation. While GMG offers these execution time advantages over PCG, it requires information regarding the underlying PDEs to be solved in order to generate different levels of discretization. On the contrary PCG only requires the coefficients of *A* and *b* in (7.2). Thus, the higher performance of GMG comes at the cost of a tighter link with the specific mathematical model which has to be solved numerically.

Table 7.2: Execution time and average error comparison for GMG and PCG.

Fine grid resolution		129x129x129		65x65x65		33x33x33	
Method		PCG	GMG	PCG	GMG	PCG	GMG
RBGS	Avg. Error	5.22e-12	1.44e-14	1.41e-11	1.66e-14	4.21e-11	1.43e-14
7p stencil	Time [ms]	1118	121	124	50	28	33
Jacobi	Avg. Error	5.21e-12	7.00e-14	1.25e-11	6.99e-14	3.89e-11	6.79e-14
19p stencil	Time [ms]	1255	172	127	48	28	32
Jacobi	Avg. Error	4.30e-12	1.49e-13	1.40e-11	1.17e-13	2.94e-11	1.19e-13
27p stencil	Time [ms]	1502	211	145	61	29	35

7.4 CONCLUSIONS

In this chapter an in-depth analysis of a GPU-based geometric multigrid method was presented. Different GMG variants, different number of smoothing steps, single and double precision, different discretization schemes and various discretization resolutions have been used.

Overall, the V-cycle GMG variant, with 312 smoothing step configuration performs best. Importantly, this version offers a speed-up of 7.1-9.2x over the PCG method on the same hardware configuration, while also leading to a smaller average residual.

Future work will focus on optimizing the smoothing step, which is the most time consuming operation of GMG, and on more advanced data storage schemes which are required for large stencils and/or very fine grids.

8. Optimized Three-Dimensional Stencil Computation on Fermi and Kepler GPUs

8.1 INTRODUCTION

Graphics Processing Units (GPUs) are dedicated processors, designed originally as graphic accelerators. Since CUDA (Compute Unified Device Architecture) was introduced in 2006 by NVIDIA as a graphic application programming interface (API), the GPU has been used increasingly in various areas of scientific computations due to its superior parallel performance and energy efficiency [Kirk et al., 2010].

The GPU is viewed as a compute device which is able to run a very high number of threads in parallel inside a kernel (a function, written in C language, which is executed on the GPU and launched by the CPU). The threads of a kernel are organized at three levels: blocks of threads are organized in a three dimensional (3D) grid at the top level, threads are organized in 3D blocks at the middle level, and, at the lowest levels, threads are grouped into warps (groups of 32 threads formed by linearizing the 3D block structure along the *x*, *y* and *z* axes respectively) [***NVIDIA, 2013].

The GPU contains several streaming multiprocessors, each of them containing several cores. The GPU (usually also called device) contains a certain amount of global memory to/from which the CPU or host thread can write/read, and which is accessible by all multiprocessors. Furthermore, each multiprocessor also contains shared memory and registers which are split between the thread blocks and the threads, which run on the multiprocessor, respectively. With the introduction of the third and fourth generation general purpose GPU (GPGPU), the Fermi

and the Kepler generations respectively [***NVIIDA, 2011], [***NVIDIA, 2013], the double precision performance has increased, and a true cache hierarchy (L1/L2) and more shared memory are available. Furthermore, the global memory bandwidth plays an important role since the performance of many kernels is bound by the peak global memory throughput: current GPUs have a bandwidth of up to 300 GB/s. The shared memory on the other side is a fast on-chip memory which can be accessed with similar throughput as the registers.

Stencil computation is a computational pattern on an *n*-dimensional grid, whereas each location is updated iteratively as a function of its neighboring locations. This pattern is found in several application domains, like image processing, computational fluid dynamics, weather prediction, quantum physics. Previous studies have shown that, if regular Cartesian grids are used, GPU based implementations are able to significantly speed up the execution compared to regular CPU based implementations [Phillips et al., 2010], [Shimokawet al., 2016].

Research activities on stencil based computations have been reported long before the introduction of general purpose GPUs. These activities focused on the information transfer between nodes [Fox, 1984] and the relationship between partition shape, stencil structure and architecture [Reed et al., 1987]. Different optimization techniques have been reported more recently for GPU based stencil computations. The most often encountered optimization techniques used in the past are blocking at registers and at shared memory [Micikevicius, 2009], [Itu et al., 2011]. Pre-Fermi GPUs did not have any cache memories, making the shared memory blocking technique vital for reducing memory access counts. Temporal blocking is another extensively used technique, with mixed performance improvements on GPUs [Grosser et al., 2011], [Holewinski et al., 2012], [Zumusch et al., 2013]. Non-GPU architectures have also been used for stencil based computations [Datta et al., 2008].

The goal of the work presented in this chapter was to evaluate the performance of 3D stencil based algorithms on a series of recent GPUs [Vizitiu et al., 2014]. Previous research activities have focused on single precision computations. With the introduction of the Fermi and the Kepler architecture, the performance of double precision computations on NVIDIA GPU cards has increased substantially. To meet the high accuracy requirements, inherent for scientific computations [Nita et al., 2013], [Zaspel et al., 2013], herein the focus is put on double precision computations. Starting from two baseline implementations, different optimization techniques are employed which lead to seven different kernel versions. Both Fermi and Kepler GPUs are used, to evaluate the impact of different optimization techniques for the two architectures.

8.2 METHODS

For studying 3D stencil based algorithms implemented on graphics processing units, the 3D unsteady heat conduction problem is considered, which is modeled as a second order partial differential equation describing the distribution of heat over time over a given 3D space:

$$\frac{\partial T}{\partial t} - a\left(\frac{\partial^2 T}{\partial x^2} + \frac{\partial^2 T}{\partial y^2} + \frac{\partial^2 T}{\partial z^2}\right) = 0, \tag{8.1}$$

where α is the thermal diffusivity constant and T represents the temperature at any point in space (x, y, z) or time (t).

For the numerical solution of (8.1) a finite difference method is applied on a 3D grid of points. A uniform mesh of points is used and the forward difference in time and central difference in space (FTCS) method is applied, leading to a 3D 7-point stencil:

$$\frac{T_{i,j,k}^{n+1} - T_{i,j,k}^{n}}{\Delta t} = \alpha\left(\frac{T_{i+1,j,k}^{n} - 2T_{i,j,k}^{n} + T_{i-1,j,k}^{n}}{\Delta x^2} + \frac{T_{i,j+1,k}^{n} - 2T_{i,j,k}^{n} + T_{i,j-1,k}^{n}}{\Delta y^2} + \frac{T_{i,j,k+1}^{n} - 2T_{i,j,k}^{n} + T_{i,j,k-1}^{n}}{\Delta z^2}\right) \tag{8.2}$$

which can be rewritten as:

$$T_{i,j,k}^{n+1} = T_{i,j,k}^{n} + d\left(T_{i+1,j,k}^{n} + T_{i-1,j,k}^{n} + T_{i,j+1,k}^{n} + T_{i,j-1,k}^{n} + T_{i,j,k+1}^{n} + T_{i,j,k-1}^{n} - 6T_{i,j,k}^{n}\right) \tag{8.3}$$

where $d = \alpha\Delta t/\Delta x^2$.

In the above equation n represents the discrete time step number, (i, j, k) represents the spatial index, Δt is the time step and Δx is the mesh spacing, which is equal in all directions. $T_{i,j,k}^{n}$ represents the temperature value at point (i, j, k), at time step n. The numerical solution is stable if the CFL condition holds: $d = \alpha\Delta t/\Delta x^2 < 1/6$.

As can be observed in (8.3), the value at a grid point at time step n+1 is computed from the values at the previous time step, from the same grid point and from its six neighboring points, leading to a 7 point stencil computation (Figure 8.1).

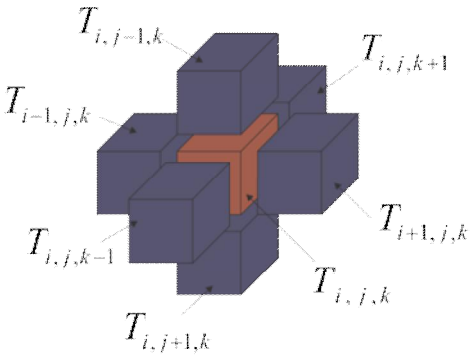

Figure 8.1: 7-point stencil used for the numerical solution of the unsteady heat diffusion equation.

This solution scheme is fully explicit: the computation of the new value at any grid point is fully independent from the computations at the other grid points.

8.2.1 Baseline GPU-based implementations

In the following two baseline GPU-based implementations of the unsteady heat diffusion problem are introduced. For the first baseline implementation (called in the following 3DBase) each grid point is handled by a separate thread. Two buffers are allocated, one for the values at the previous time step and one for the values at the new time step. To eliminate the memory copy requirement from one buffer to the other, the buffers are swapped at the end of each time step.

Since for the latest GPUs the execution configuration allows not only for 3D blocks of threads, but also for a 3D grid of thread blocks, the threads and the thread-blocks are organized both into 3D structures. Thus, each thread of the grid corresponds to a grid point in the 3-D computational domain. To compute the new value at a grid point each thread performs seven global memory read operations at each time step. Since global memory operations are very slow, this represents a severe limitation of the kernel performance.

In the CUDA architecture, each thread block is divided into groups of 32 threads called warps, each of which is executed in a SIMD fashion (all threads of the same warp execute the same instruction at a time). If the threads inside a warp follow different execution paths, the execution of the branches is serialized. Thus, warp divergence is another aspect which leads to loss of parallel efficiency (a minimum amount of warp divergence is required to distinguish between boundary and non-boundary nodes, so as to perform the computations only for the latter ones).

On the other hand, stencil codes can be characterized by their FLOPs per byte ratio. The baseline implementation performs 13 double-precision floating point operations per update [Maruyama et al., 2014]. This leads to $13 \cdot xDim \cdot yDim \cdot zDim$ operations performed at each iteration (*xDim*, *yDim* and *zDim* represent the grid dimensions). If one assumes that at each time step once the old values are loaded they remain in the cache memory (which is unlikely for grid dimensions which exceed the cache size) the amount of data loaded and stored per time step is equal to $xDim \cdot yDim \cdot zDim \cdot$ sizeof(double) $\cdot 2$. Hence the flop per DRAM byte ratio is:

$$\frac{13 \times xDim \times yDim \times zDim}{xDim \times yDim \times zDim \times sizeof\,(double) \times 2} = 0.8125 \tag{8.4}$$

Current GPUs, however, have a significantly higher ratio. According to this model the performance of the stencil on the GPU is therefore limited by its memory bandwidth.

To allow for a better memory usage, also a more efficient approach is considered, whereas threads and thread-blocks are organized into 2D structures. The computational grid is divided into *x*-*y* planes and the subdomains are assigned to separate thread blocks. Each 2-D slice is represented through the grid points in the *x* and *y* directions, providing for the threads the (*i*, *j*) indices of the grid points. A loop is then used to traverse the grid in the *z*-direction and obtain the final *k* coordinate as shown in Figure 8.2 (this kernel version is called in the following 2DBase).

Unlike the 3DBase implementation, for which a thread updates a single point, herein the same thread operates on several grid points. These points are placed equidistant from each other, the distance from one grid point to another is determined based on the size of the 3D domain ($xDim \cdot yDim$).

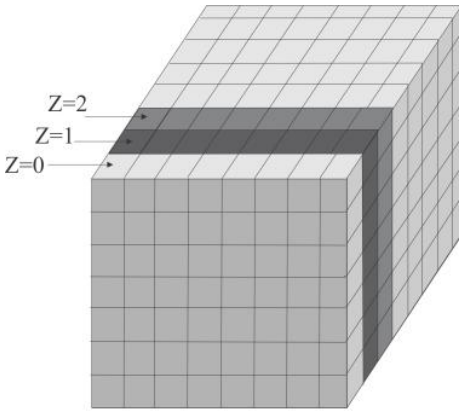

Figure 8.2: 2DBase kernel: the computational grid is divided into *x*-*y* planes and a loop is then used to traverse the grid in the *z*-direction.

8.2.2 Optimized implementations

Next, a series of optimization techniques are described for the two baseline implementations. The focus is mainly put on minimizing warp divergence and global memory accesses. Besides global memory, the GPU architecture provides fast on-chip memory, registers and shared memory, which is distributed between threads and thread blocks respectively.

8.2.2.1 Three-dimensional baseline implementation with Shared Memory Usage and Data Overlap

The starting point for the new kernel is the 3DBase implementation. Since shared memory is allocated at thread block level, threads can cooperate when populating data blocks allocated in the shared memory. If data can then be reused by different threads, global memory accesses are reduced and overall kernel performance is improved.

Shared memory arrays of size $blockXDim \cdot blockYDim \cdot blockZDim$ are allocated (*blockXDim*, *blockYDim* and *blockZDim* represent the dimensions of the thread blocks).

Each thread within a block loads the value of the grid point it handles from global memory to shared memory. To avoid undefined behavior and incorrect results when sharing data read by different threads, a synchronization barrier is introduced. All values required for the implementation of (8.4) are then read from the shared memory.

With this technique, threads lying at the border of a thread block do not have access to all their neighbors and can not compute the corresponding new values. Hence, the execution configuration is designed so as to ensure block overlapping in all directions (Figure 8.3 - 3DShMOverL). This, however, results in global memory read redundancy: grid points lying in the overlapping regions of the blocks are read more than once for a single time step.

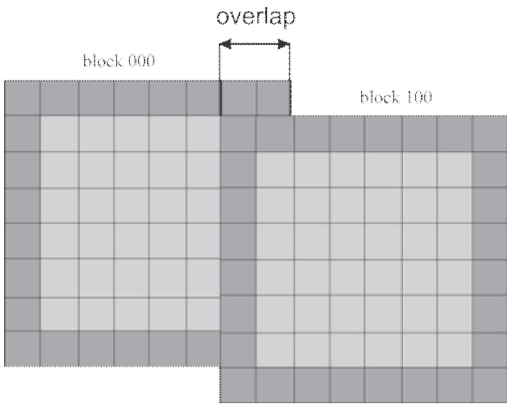

Figure 8.3: 3DShMOverL kernel: the shared memory arrays have the same size as the thread blocks. Thread blocks overlap to enable the computation at all grid points.

8.2.2.2 Three-dimensional baseline implementation with Shared Memory Usage and no Data Overlap

Starting again from the 3DBase implementation, a different shared memory based strategy is developed. The shared memory arrays are padded with an additional slice on each side of the 3D block leading to a total size of $(blockXDim + 2) \cdot (blockYDim + 2) \cdot (blockZDim + 2)$, as shown in Figure 8.4.

First, each thread populates the value of the grid point it handles in shared memory. Next, the threads located on the boundary of the block load the remaining data slices from global

memory to the shared memory (note that the corner points of the blocks are not required for the 7-point stencil). To load points located outside of the block, conditional operations are introduced which cause branch divergence.

Thus, each thread of a thread block has access to all its neighbors and is able to update the corresponding grid point (no overlapping between thread blocks is required - 3DShMNoOverL).

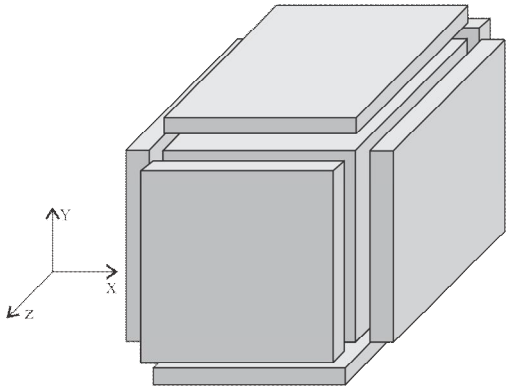

Figure 8.4. 3DShMNoOverL: the shared memory arrays are padded with additional data slices loaded by the threads located at the border of the thread block.

8.2.2.3 Two-dimensional distribution of threads with additional register usage

The 2DBase implementation can be optimized by storing redundant data in registers. Therein, the value of the current grid point for adjacent 2D slices is read from the global memory by the same thread. The same holds true for grid points which lie on the front or back sides of the 2D slices.

Because slices are iterated along the *z* direction, the value at grid point (*i*, *j*, *k*+1) becomes the value at (*i*, *j*, *k*) at the next iteration. Similarly, the value at (*i*, *j*, *k*) becomes the value at (*i*, *j*, *k*–1). Instead of rereading these values, registers are used for caching them and two global memory accesses are saved at each iteration along the *z* axis (in the following this kernel is called 2DReg).

8.2.2.4 Two-dimensional distribution of threads with Shared Memory Usage

As for the kernels with 3D thread blocks, shared memory can also be used to reduce global memory accesses for the kernels with 2D thread blocks. The size of the shared memory array chosen for this kernel version is (*blockXDim* + 2) · (*blockYDim* + 2). To allow each thread of the thread block to compute the new value of the corresponding grid point, additional slices are populated at each border of the 2D shared memory array. Hence, the size of the shared memory array used for this configuration is (*blockXDim* + 2) · (*blockYDim* + 2). Each thread first reads the value of the grid point it handles and stores it in the shared memory. Next, threads located on the boundary of the block load the remaining values (in the following this kernel is called 2DShM).

8.2.2.5 Two-dimensional distribution of threads with Additional Register and Shared Memory Usage

For the implementation version described in section 8.2.2.4 the loading of the central section of the shared memory does not introduce any divergent branches since it is not

conditioned. The loading of the slices with *y* index equal to 0 or *blockYDim* + 2 introduces a maximum of two divergent branches, one for each half-warp, depending on the compute capability of the GPU. On the other side, the slices with *x* index equal to 0 or *blockXDim* + 2 lead to divergent branches and only one thread of the entire half-warp performs a read operation. This aspect may be alleviated by the cache memory, but this depends on the size of the slices.

To reduce branch divergence, the shared memory array is used only for the central section and for the slices with index equal to 0 or *blockYDim* + 2, while the other values are read from the global memory and stored into registers. Only the threads lying at the left or right border perform separate global memory reads (Figure 8.5 - 2DShMReg), while the other values are safely read from the shared memory**.**

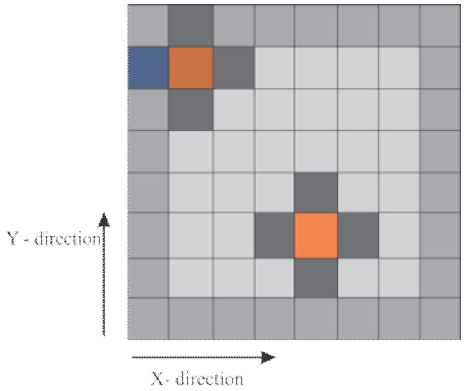

Figure 8.5: 2DShMReg: Northern and southern slices are read from the shared memory, eastern and western values from the global memory.

Hence, the size of shared memory array used in this case is *blockXDim* · (*blockYDim* + 2). Each thread first reads the value of the grid point it handles and stores it in the shared memory. Next, threads located on the upper and lower boundary of the block load the remaining values.

Besides the two registers that store the values of the nodes located next to the left and right boundaries, another 2 registers are used for the optimization described in section 8.2.2.2.

8.3 RESULTS

To evaluate the performance of the different strategies for running 3D stencil based algorithms on GPUs, three different NVIDIA GPU cards were used: GeForce GTX 480, GeForce GTX 660M and GeForce GTX 680 (the first one is based on the Fermi architecture, while the other two are based on the Kepler architecture), together with the CUDA toolkit version 5.5. The unsteady heat conduction problem was solved on a rectangular domain with Dirichlet boundary conditions, whereas the boundary values were set to 100°C for one side of the rectangle and 0°C for the other sides. The thermal diffusivity constant was se to $1.9 \cdot 10^{-5}$ m^2/s and the computations are performed until convergence is reached. The numerical solution was obtained on a grid of 128x128x128 nodes and is displayed in Figure 8.6. The numerical solution was identical for all three GPU cards and for all implementation versions down to the 15^{th} decimal, i.e. close to the precision of the double-type representation in computer data structures.

Table 8.1 displays the execution times for one time step for the three above mentioned GPU cards, obtained for the seven different kernel versions introduced in the previous section. The GTX660M card leads to the largest execution times although it has been considerably later released compared to the GTX480 card. This can be explained however by the fact that this card

was specifically designed for low power consumption, so as to be used in notebook PCs (whereas the GTX480 and GTX680 were reported with a power consumption of 250 W and 195 W respectively, the GTX660M only required 50W). The GTX680 is the best performing card: for each of the seven implementation versions it leads to the smallest execution times. The ratio of the execution times for the GTX660M and GTX680 cards varies between 4.26 and 5.56 for different kernel versions. This roughly reflects the inverse of the power consumption ratio, which is equal to 3.9.

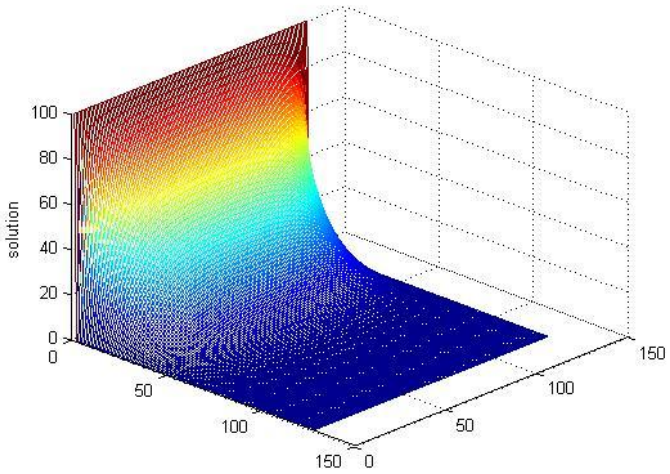

Figure 8.6: Computation result for the unsteady heat conduction problem on a rectangular domain with Dirichlet boundary conditions.

Table 8.1: Execution time [ms] for a single time step, obtained for the seven different implementation versions on three different GPU cards.

Method	GTX480	GTX 660M	GTX 680
3Dbase	1.7	3.45	0.62
3DShMOverL	3.5	6.17	1.13
3DShMNoOverL	1.8	3.78	0.73
2Dbase	1.2	3.09	0.63
2Dreg	0.9	2.47	0.58
2DShM	1.2	2.87	0.59
2DShMReg	1.09	2.32	0.48

Interestingly, whereas for the GTX660M and the GTX680 cards the 2DShMReg kernel performs best, for the GTX480 card the 2DReg kernel leads to the smallest execution time. Shared memory based optimizations were particularly important for pre-Fermi GPU cards. For the Fermi architecture these optimizations were not always leading to a better performance due to the fact that the global memory read operations were cached at L1 level. Even though the cache size is regularly small, it is efficient for algorithms based on Cartesian grids where data access patterns are regular [Shimokawabe et al., 2011]. For the Kepler architecture however the L1 cache is no longer used for caching global memory read operations, but only for register spilling [***NVIIDA, 2013].

Hence, for the GTX480 card (Fermi), since the L1 cache is intensively used for caching global memory read operations, the 2DReg kernel outperforms the 2DShMemReg kernel. On the other hand, for the GTX660M and the GTX680M, since the L1 cache functionality is limited to register spilling, shared memory usage became more important, illustrated by the better performance of the 2DShMReg kernel.

In the following the focus is put on the differences between the kernel versions for the GTX680 card, which was determined as the best performing one considered herein. Table 8.2 displays besides the execution time other important details of the various kernel versions.

Table 8.2: Kernel performance and details for the GTX680 card.

Method	Execution time [ms]	Reg. per thread	Divergent branches	Shared memory per block [bytes]	Total number of 64 bit global load instr.	Total number of 64 bit global store instr.
3DBase	0.62	25	12016	-	14002632	2000376
3DShMOverL	1.13	19	20811	4096	4741632	2000376
3DShMNoOverL	0.73	21	12694	8000	3524851	2000376
2DBase	0.63	25	94	-	14002632	2000376
2DReg	0.58	25	94	-	10033632	2000376
2DShM	0.59	25	94	800	6953688	2000376
2DShMReg	0.48	25	94	640	2984688	2000376

The two baseline implementations (2DBase and 3DBase) lead to almost identical execution times. Referring first to the kernels based on a 3D thread block structure, the 3DShMOverL performs worse than the 3DBase kernel: execution time increased by 82% although the number of global accesses was reduced by 66.13%. This can be explained by the fact that a considerable amount of threads perform only load operations.

Compared to the 3DShMOverL kernel, the execution time decreased by 35.39% and the total number of read operations was reduced by 25.66% for the 3DShMNoOverL kernel. Compared to the 3DBase kernel, this implementation is compute limited instead of bandwidth limited. The main reason for the change of the limitation type lies in the number of divergent branches, which increased considerably and which in the end leads to a higher execution time than for the 3DBase kernel.

Next, the focus is put on the kernels which are based on a 2D thread block structure. The 2DReg kernel leads to a significant reduction of memory operations (28.34%) and as a result of the execution time (7.93%), compared to the 2DBase kernel. The 2DShM kernel further reduces the number of global memory load operations but execution time increases slightly, which is caused by the non-optimized register usage. Finally the 2DShMReg combines both techniques (optimized register and shared memory usage), and reduced execution time by 17.24% and the total number of read operations by 70.25% compared to the 2Dreg kernel.

Overall, the kernels with 2D thread block structure outperform the ones with 3D thread block structure for double precision computations, confirming the findings for single precision computation reported in [Maruyama et al., 2014].

8.4 CONCLUSIONS

In this chapter, performance studies for 3D stencil based algorithms have been presented for recent NVIDIA GPUs. This is the first study to evaluate different implementation and optimization strategies for double precision computations. The increased accuracy obtained for double precision is required in scientific computations, which represent the main area of application for the 3D stencil based algorithms.

Starting from two different baseline implementations (based on 3D and 2D thread block structures), different optimization strategies have been applied which have lead to different performance changes for the Fermi and Kepler cards. Overall the GTX680 GPU card (Kepler architecture) performed best for a kernel with 2D thread block structure and optimized register and shared memory usage. Conversely, for the GTX480 GPU card (Fermi architecture) the 2D kernel, which does not use shared memory but is optimized in terms of register usage, performed best, mainly due to the different L1 cache usage in the Fermi architecture. Hence, shared memory usage has become essential for double precision stencil based computation on Kepler GPUs.

Finally, for the Kepler architecture, the performance was evaluated for a GPU designed for desktop PCs (GTX680) and for a GPU designed for notebook PCs (GTX660M). The results have indicated that the ratio of execution time is roughly equal to the inverse of the ratio of power consumption.

Part III

The Evolution and Development Plans for Career Development

9. Academic and Research Career

Past Research Activities
Past Academic Activities
Future Academic and Research Activities

9.1 PAST RESEARCH ACTIVITIES

I have started my research activities during the bachelor studies, mainly through publications in local journals and participation at scienctific student competitions. I have then started in 2010 my PhD studies at the Faculty of Eletrical Engineering of the *Transilvania University of Brasov*. The studies have been carried out under the umbrella of the Sectorial Operational Programme for Human Resources – PhD studies for continuous development – POSDRU/107/1.5/S/76945, through a PhD scholarship.

I have obtained my PhD title in 2013 for the PhD thesis entitled *Parallel Processing in the Multiscale Modeling of Coronary Hemodynamics*.

The main goal of the PhD thesis was the development, implementation, testing and validation of a reduced-order multiscale model of the coronary circulation for the non-invasive diagnosis of coronary stenoses. Based on the properties of this multiscale model, a secondary goal of the thesis was to develop, implement, test and validate a multiscale model for the non-invasive diagnosis of aortic coarctations. The final goal of the developed models was for them to be applied in a clinical setting for the non-invasive, patient-specific assessment of cardiovascular pathologies. Thus, execution time was a crucial aspect, on one hand to diagnose a patient faster, and, on the other hand, to run more computations in a certain amount of time. Hence, to reduce the execution time, the numerical solution of the quasi one-dimensional model, which represents

the main component of the multiscale models developed herein, was implemented on a parallel processor (graphics processing unit).

Additionally, I have had three research internships at Siemens Corporate Research in Princeton, New Jersey USA (Febr. 2011 – Apr. 2011, Aug. 2011 – Nov. 2011, July 2012 – Sept. 2012), and since Oct. 2013 I am also a Research Engineer at Siemens SRL, Brasov, Romania. The main research activities carried out after the PhD studies have been described extensively in the previous chapters.

Overall, the research activities carried out to date have lead to the publication of 52 research papers in journals and conferences, 22 of them as first author. Importantly, nine papers have been published in ISI journals with high impact factor (five of them as first author). I am also author or co-author of six books, including one published with Springer.

Furthermore, I am joint-author of over 20 patent applications filed with the US / World / European Patent Offices. My works have received over 100 citations (excluding self-citations) and I have an h-index and i10-index of 7, according to google scholar (https://scholar.google.com/citations?user=6azBRUAAAAAJ).

I have been reviewer for several ISI journals with high impact factor, like *International Journal for Numerical Methods in Biomedical Engineering*, *Computer Methods in Biomechanics* and *Biomedical Engineering şi Medical & Biological Engineering & Computing*.

I have been / am a member in several research projects:

- **Model-Driven European Paediatric Digital Repository (MD-Paedigree)**, funded by the EC (FP7), 2013-2017;
- **High Performance Computing of Personalized Cardio Component Models (HEART)**, funded by the Romanian Government (PNII), 2012-2016;
- **Large scale experiments and simulations for the second generation of FuturICT (FuturICT 2.0)**, funded by FLAG ERA, Jan. 2017 – Jan. 2020;
- **Rethinking Robotics for the Robot Companion of the future (Robocom++)**, funded by FLAG ERA, Jan. 2017 – Jan. 2020.

I am a principle investigator (responsible for project partner) in the following ongoing research projects:

- **MyHealth-MyData (MHMD)**, funded by the EC (H2020), Nov. 2016 – Oct. 2019 (project coordinator for partner *Transilvania University of Braşov*, managed budget: 147.750 Euros). The project aims at changing the existing patients' privacy and data security scenarios by introducing a distributed architecture, based on Blockchain and Personal Data Accounts. Our goal in the project is the development of a blood flow model of the systemic circulation for demonstrating the feasibility of personalized hemodynamic modeling on securely anonymized data;
- **Information Technology: The Future of Cancer Treatment (ITFoC)**, funded by FLAG ERA, Jan. 2017 – Jan. 2020 (project coordinator for partner *Transilvania University of Braşov*, managed budget: 62.500 Euros). The project will showcase federated activities on breast cancer to propose an advanced TRL 5-6 demonstrator in digital medicine. Our goal is to employ deep learning based techniques for developing an alternative to the compute intensive mechanistic models;
- **Frictionless Energy Efficient Convergent Wearables for Healthcare and Lifestyle Applications (CONVERGENCE)**, funded by FLAG ERA, Jan. 2017 – Jan. 2020 (project coordinator for partner *Transilvania University of Braşov*, managed budget: 35.000 Euros). The project aims at developing a wearable sensor platform, centred on

energy efficient wearable proof-of-concepts at system level exploiting data analytics developed in a context driven approach (in contrast with more traditional research where the device level research and the data analytics are carried out on separate path, rarely converging). Our goal is to develop a predictive personalized model for cardiovascular risk assessment. Specifically, a patient-specific multiscale reduced-order blood flow model of the entire systemic circulation will be employed, which is personalized from a set of initial measurements (height, weight, BMI, gender, length of arms, legs, neck, head, etc.) and a set of continuous measurements derived from wearable sensors.;

- **Image-based functional assessment of complex coronary artery lesions using optical coherence tomography and routine angiography (FUNCTIONAL-OCT)**, funded by the Romanian Government (PNIII), Jan. 2017 – July 2018 (project coordinator for partner *Siemens SRL*, managed budget: 100.000 Euros). The main goal of this project is to develop, implement, test and validate a patient-specific computational hemodynamics model for computing Fractional Flow Reserve (FFR) from medical images acquired through Optical Coherence Tomography (OCT) and X-ray Angiography (XA), and routine patient-specific measurements;
- **Image-based functional assessment of renal artery stenosis using Computer Tomography Angiography or routine X-ray Angiography (RENA)**, funded by the Romanian Government (PNIII), Jan. 2017 – July 2018 (project coordinator for partner *Siemens SRL*, managed budget: 117.000 Euros). The main goal of this project is to develop, implement, test and validate a patient-specific computational hemodynamic model for determining renal hemodynamic diagnostic indices, renal Fractional Flow Reserve and peak / mean trans-stenotic pressure gradient, from medical images acquired through either Computer Tomography Angiography (CTA) or X-ray Angiography (XA).

9.2 PAST ACADEMIC ACTIVITIES

My teaching activity began in 2009, as an associate lecbturer, consisting in the teaching of the laboratories for the course *Programmable Logic Controllers*, which started right after I had graduated the Faculty of Eletrical Engineering and Computer Science of the *Transilvania University of Brasov*. In 2014, after finishing the PhD studies, I became a full time lecturer at the Department of Automation and Information Technology of the *Transilvania University of Brasov*. During the following years I have taught the courses:

- *Programmable Logic Controllers*: the goal of the course is to instruct students in the topics of design, implementation and usage of the hardware structures and software applications destined for controlling processes run with programmable logic controllers. A significant emphasis is put on the familiarization with hardware and software aspects, in the context of programmable logic controller usage in the industry;
- *Programming of Real Time Applications*: the goal of the course is to instruct master students in the topics of conception, design, implementation and exploitation of real time programs for process control. The course and the laboratory allow the master students to become familiarized with software aspects, in the context of employing real time computers in industry. Furthermore, the course enables the training of the master students for using real time systems in the development of technical informatics applications;

- *Control Systems for Technological Processes*: the goal of the course is to provide know-how for exploiting and designing automated systems typically encountered in industry. The course presents the components of these systems, methods for deriving analytical models, methods for calibration, as well as ways for embedding the automated systems in industrial installations, with exemplification in several study cases;
- *Industrial Control Networks*: the goal of the course is to instruct students in the topics of design, implementation and usage of the hardware structures and software applications of industrial control networks. A significant emphasis is put on the familiarization with hardware and software aspects, in the context of programmable logic controller usage in the industrial control networks.

Three of the books I have published are related to these courses:

- *Programarea aplicatiilor de timp real*, Editura Universităţii Transilvania din Braşov, 2016, ISBN: 978-606-19-0751-9;
- *Automate Programabile. Aplicații*, Editura Universităţii Transilvania din Braşov, 2016, ISBN: 978-606-19-0862-2;
- *Introducere în Rețele Industriale de Comunicație*, Editura Universităţii Transilvania din Braşov, 2016, ISBN: 978-606-19-0885-1.

During the years I have developed several practical applications using programmable logic controllers, which are now used in the laboratory of the course *Programmable Logic Controllers*. Herein I would like to mention two of these applications:

- Positioning system using brushless servomotors, inverter 635 and a XC200 programmable logic controller;
- Distributed control network of sequential processes using Moeller Programmable Logic Controllers.

Given the interdisciplinarity of the above mentioned courses, I have continuously tried to improve the teaching methods, the collaboration with the students, and to diversify the materials and the information presented during the classes. My preferred teachning methods are: classic lecture, explanations, problems, demonstrations, conversation, case studies, and experiments in small groups.

I have always maintained a close connection between the academic and the research activities, by collaborating with students on topics that are highly relevant in various research areas like computational modelling, parallel processing, and biomedical engineering. As such I have coordinated students which have taken part in the event *Researcher's Night* which is organized yearly at the *Transilvania University of Brașov*, based on the topics:

- Non-invasive methods for diagnosing cardiovascular pathologies;
- System for detecting bone metastasis in the spine using deep learning techniques;
- Fluid-solid interaction simulations for non-invasive diagnosis of teh aortic valve.

Furthermore I have supervised several works presented at the *Student's Research Communications Workshop* organized yearly at the *Transilvania University of Brașov*. Several of these works have been awarded prizes. Herein I would like to mention especially the work of Costin Ciușdel, who developed a machine learning-based model for predicting average strain as an alternative to physics-based approaches for the non-invasive evaluation of osteoporosis patients.

I have supervised and co-supervised numerous bachelor and master theses on the following topics:

- Lattice Boltzmann based blood flow simulations;
- GPU-based implementation of the multigrid algorithm;
- Semantic search and information retrieval.

Importantly, the students who have worked on these topics have also managed to publish research papers at international conferences. Herein I would like to mention only a subset of those:

- GPU Accelerated Information Retrieval Using Bloom Filters, International Conference on System Theory, Control and Computing, 2015;
- GPU Accelerated Geometric Multigrid Method: Performance Comparison on Different Architectures, Inter. Conf. on System Theory, Control and Computing, 2015;
- GPU-accelerated model for fast, three-dimensional fluid-structure interaction computations, Annual Inter. Conf. of the IEEE Engineering in Medicine & Biology Society, 2015;
- Optimized Three-Dimensional Stencil Computation on Fermi and Kepler GPUs, IEEE High Performance Extreme Computing Conference, 2014.

I am also actively involved in the supervision of two PhD students, Cosmin Niță and Anamaria Vizitiu, on the topics of Lattice Boltzmann based *Fluid-Structure Interaction Blood Flow Models* and *Deep Learning based Diagnosis of Breast Cancer Patients*.

Finally, I would like to mention that I am a member of the Romanian Society of Automation and Technical Informatics since 2010.

9.3 FUTURE RESEARCH AND ACADEMIC ACTIVITIES

Hemodynamic computations represent a state-of-the-art approach for patient-specific assessment of cardiovascular pathologies. Thus, blood-flow computations, when used in conjunction with patient-specific anatomical models extracted from medical images, provide important insights into the structure and function of the cardiovascular system. In recent years, these techniques have been proposed for diagnosis, risk stratification, and surgical planning.

Future research activities will focus on the further development of computational methods for personalized cardiovascular medicine, by combining the methods employed in the past:

- Computational modeling;
- Artificial intelligence / Machine learning;
- High performance computing.

The ultimate goal of each such development will be its implementation in a clinical workflow, enabling truly personalized medicine, and thus improving patient diagnosis, outcome, and life quality, and at the same time reducing overall healthcare costs patient risks.

I believe that future activities should form a cycle containing: research projects, scientific research, and development of the teaching process.

Research projects provide a framework which introduces structure into the research activities, it ensures the financing and demands progress and capitalization of the previously identified future research directions. Research activities require continuos personal development, providing thus an opportunity for transforming scientific know-how into teaching material. Finally, teaching activities represent sources for ideas for future grant proposals, but also allow for a recruitment of students willing to start a research career, with the following possible milestones: class, student research activities, bachelor thesis, master thesis, PhD thesis.

As such, I am highly motivated to take part in grant calls, both at national and international level. I have submitted / contributed to the submission of three such grant proposals at the start of 2017:

- Image-based real-time functional assessment of patients with acute coronary syndromes using routine angiography (FUNCTIONAL-ACS), competition PN-III-PD, organized by UEFISCDI (grant amount: 55.000 Euros);
- Quantum based signal filtering architecture for enhancing real-time Brain-Computer Interface (QuantBCI), competition QUANT-ERA 2017, organized by the European Commission (grant amount: 200.000 Euros);
- CLEVER: Ct-based pLaquE VulnErability pRediction, competition ERA-CVD 2017, organized by the European Commission (grant amount: 200.000 Euros).

I will work towards developing a research group based on young researchers so as to steadily increase the volume of scientific results and to sustain the tasks that need to be carried out in various research projects.

I will continue to publish research papers, especially in high impact ISI journals, like: Journal of Buimechanic, Annals of Biomedical Engineering, Journal of Computational Physics, International Journal on Numerical Methods in Biomedical Enginerring, Computational Optimization and Applications, Concurrent Engineering-Research and Applications.

Furthermore, based on the scientific results achieved in the past, I will publish books focused on specific topics, so as to accelerate the transfer of know-how into the teaching process.

A few specific research activities that will be considered in the near future are described below in greater detail.

9.3.1 Machine learning based real-time computation of hemodynamic quantities from medical images

Computational Fluid Dynamics (CFD) based blood flow computations, when used in conjunction with patient-specific anatomical models extracted from medical images, have been proposed for determining non-invasively the above mentioned hemodynamic quantities [Taylor et al., 2013]. The CFD-based models combine geometrical information extracted from medical imaging with background knowledge on the physiology of the patient, encoded in a complex mathematical fluid flow model consisting of partial differential equations which can be solved only numerically. This approach leads to a large number of algebraic equations, making it computationally very demanding [Taylor et al., 2013]. Typically the solution of these models requires a few hours on powerful clusters for high-fidelity models, and, hence, their application in routine clinical workflows for providing results in real time is not feasible.

Thus, a future development will focus on the development, implementation, and validation of a machine learning-based method for determining in real-time hemodynamic quantities from medical images and routine patient-specific measurements (Figure 9.1).

Several Machine Learning (ML) based models will be developed and validated for predicting cycle-averaged quantities (e.g. cycle-averaged pressure, flow rate), regional averaged quantities (ESS), and instantaneous quantities (e.g. peak velocity). In ML based workflows, the relationship between input data, e.g. the anatomy of a vascular tree, and hemodynamic quantities of interest, is represented by a model built from a database of samples with known characteristics and output. Once the model is trained, its application to unseen data provides results in real-time.

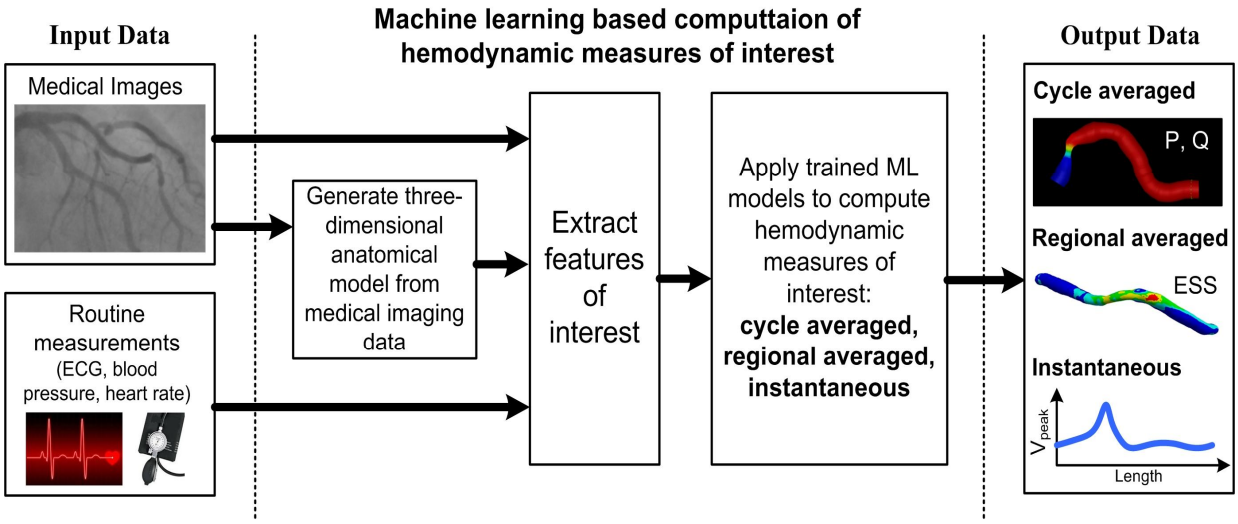

Figure 9.1: Workflow of the method proposed for machine learning based computation of hemodynamic measures of interest.

9.3.2 Image-based functional assessment of complex coronary artery lesions using Optical Coherence Tomography and Routine Angiography

CAD patients suffer from a buildup of plaque in the coronary arteries, resulting in a decrease of blood flow to the cardiac muscle. Since in severe cases this reduction of flow can result in myocardial ischemia and death, Percutaneous Coronary Intervention (PCI) is performed for revascularizing functionally significant CAD. Invasive coronary X-ray Angiography (XA) is the gold standard in CAD imaging [Ryan, 2002], but intravascular imaging techniques like Optical Coherence Tomography (OCT) are being employed increasingly for evaluating the cross-sectional and 3D microstructure of blood vessels. OCT provides high-resolution images of intraluminal and endothelial / intimal structures such as ruptured plaques, thrombi, spontaneous dissections, and angiographically vague coronary anatomy, such as ostial, bifurcation, and left main lesions.

Furthermore, OCT is of value in determining stent parameters and defining mechanisms of stent restenosis.

Since anatomical markers have a limited accuracy for the evaluation of CAD [Toth et al., 2014], the functional index of Fractional Flow Reserve (FFR), defined as the ratio of hyperemic cycle-averaged pressure distal to the stenosis to the cycle-averaged aortic pressure [Ijls et al., 1996], has been introduced and validated as an alternative [Tonino et al., 2009].

Thus, a future development will focus on the development, implementation, and validation of a patient-specific computational hemodynamics model for computing FFR (FFR_{OCT}) from medical images acquired through OCT and XA, and routine patient-specific measurements (Figure 9.2).

The output of this method will be FFR_{OCT} at each location along the centerline of the anatomical models reconstructed from the medical images. Model-based computation of FFR has been previously performed using Computational Fluid Dynamics (CFD) algorithms based on anatomical models reconstructed from Coronary Computed Tomography Angiography (CCTA) [Coenen et al., 2015] or XA [Tröbs et al., 2016].

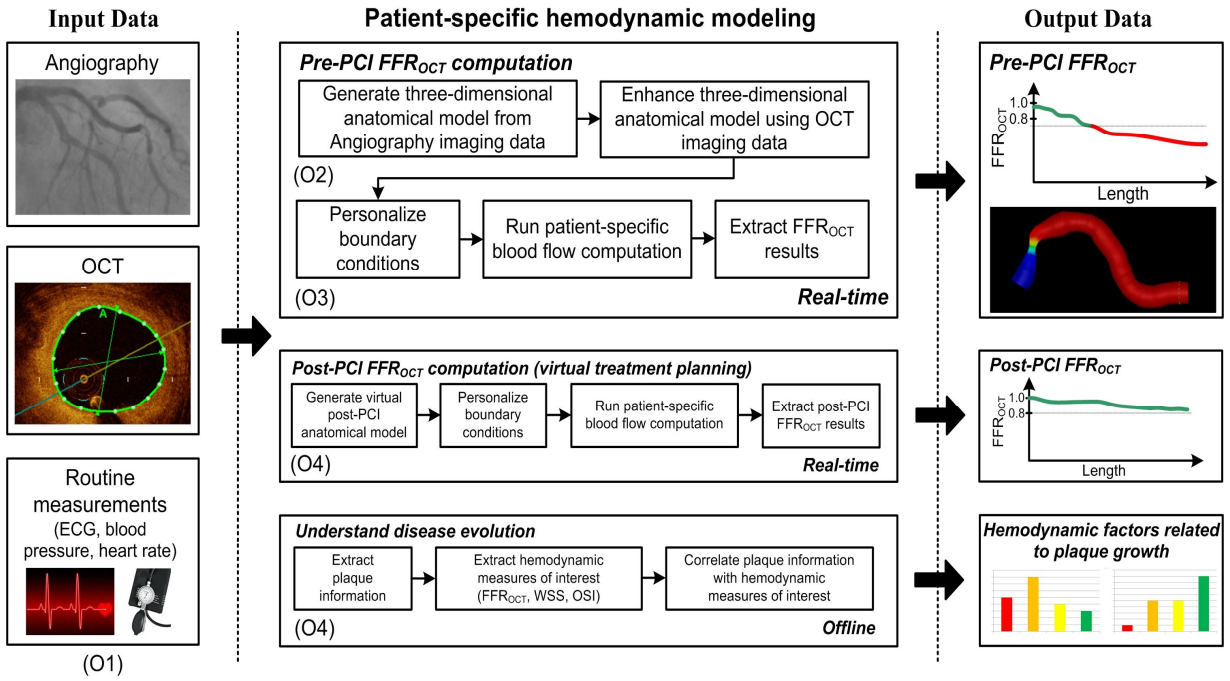

Figure 9.2: Workflow of the method proposed for functionall assessment of CAD.

9.3.3 Image-based functional assessment of renal artery stenosis using Computer Tomography Angiography or routine X-ray Angiography

Hypertension is the most important source of morbidity and mortality among the 19 major risk factors affecting global health [***WHO, 2009]. Renal Artery Stenosis (RAS) is a cardiovascular pathology consisting in the narrowing of the renal artery and represents the major cause for secondary hypertension, being encountered in 0.5 to 5% of all hypertensive patients [Hansen et al., 2002]. If left untreated, RAS progresses relentlessly in time and patient survival rate decreases with increasing RAS severity [Safian et al., 2001]. X-ray Angiography (XA) remains the standard method for the detection of RAS, although Computer Tomography Angiography (CTA) and other techniques are increasingly being used [Khan et al., 2013]. Similar to coronary artery stenosis diagnosis, the renal fractional flow reserve (rFFR – ratio of cycle-averaged distal renal pressure to cycle-averaged aortic pressure) was introduced [Subramanian et al., 2005]. However, the routine use of invasive pressure measurements (pressure gradient / rFFR) is still relatively uncommon due to additional risks and significant costs in patient care.

Thus, a future development will focus on the development, implementation, and validation of a patient-specific computational hemodynamic model for determining renal hemodynamic diagnostic indices, rFFR and peak / mean trans-stenotic pressure gradient, from medical images acquired through either CTA or XA, and other patient-specific quantities: Doppler Ultrasound (US) blood flow velocity measurements, blood biomarkers and routine patient-specific measurements (Figure 9.3). The output of this method will be $rFFR_{CTA}$ / $rFFR_{Angio}$ at each location along the centerline of the anatomical models reconstructed from the medical images and the peak / mean trans-stenotic pressure gradients for each stenosis ($\Delta P_{peak–CTA}$, $\Delta P_{mean–CTA}$ / $\Delta P_{peak–Angio}$, $\Delta P_{mean–Angio}$).

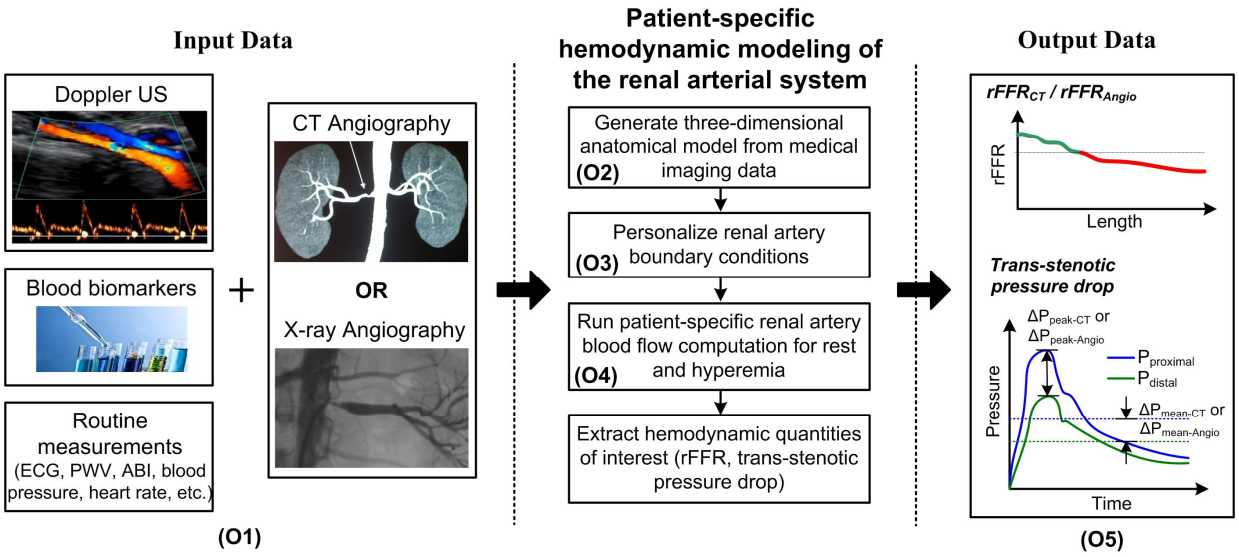

Figure 9.3: Workflow of the method proposed for the patient-specific hemodynamic modeling of the renal arterial system.

9.3.4 Continuous health monitoring using wearavle devices

9.3.4.1 Introduction

The World Health Organization [WHO, 2009] considers hypertension to be by far the most important source of morbidity and mortality among its 19 listed major risk factors affecting global health. By predisposing for heart failure, kidney disease, stroke, and dementia and the subsequent costs to society, hypertension is a major therapeutic target for improving the health and wellbeing of the elderly in low-, middle- as well as high-income countries. Despite intense research activities over the last 70 years, the etiology of hypertension is still not well understood. This lack of understanding hampers development of more effective therapeutic strategies.

Peripheral Arterial Disease (PAD) of the lower extremities is a common disease affecting approximately 12 million people in the United States [Marso et al., 2006]. Atherosclerosis is the major cause of PAD of lower extremities [Weitz et al., 1996].

The prevalence of PAD varies based on the population surveyed and the methodology of computing the Ankle-Brachial Index (ABI) [Selvin et al., 2004], [McDermot et al., 2000]. ABI is the screening test of choice for the diagnosis of patients with PAD due its simplicity, reproducibility and cost effectiveness.

9.3.4.2 Proposed Methods

A methodology which goes beyond the above described approaches is envisaged: a patient-specific reduced-order blood flow model of the entire systemic circulation is employed, which is personalized from a set of initial measurements and a set of continuous measurements derived from wearable sensors (Figure 9.4).

During the first step a set of initialization measurements are performed: these may be based on medical imaging, like MRI, or only on more basic measurements like height, weight, BMI, etc. of the subject. These measurements are used to perform an initial personalization of the arterial model, i.e. the systemic arterial geometry is defined. Next, continuous measurements are acquired from the wearable sensors. These measurements have been described in the previous section and include quantities like heart rate, blood pressure, pulse oximetry measurements,

ECG, etc. These measurements are used together with the previously personalized arterial geometry to run fully personalized blood flow computations. The outputs of the hemodynamic computations are: time-varying flow rate, pressure and cross-sectional area at all locations in the systemic arterial tree. Based on these quantities the measures of interest are extracted, which may be central arterial blood pressure, severity of PAD, severity of coarctation, onset of hypertension, risk of CVD, etc.).

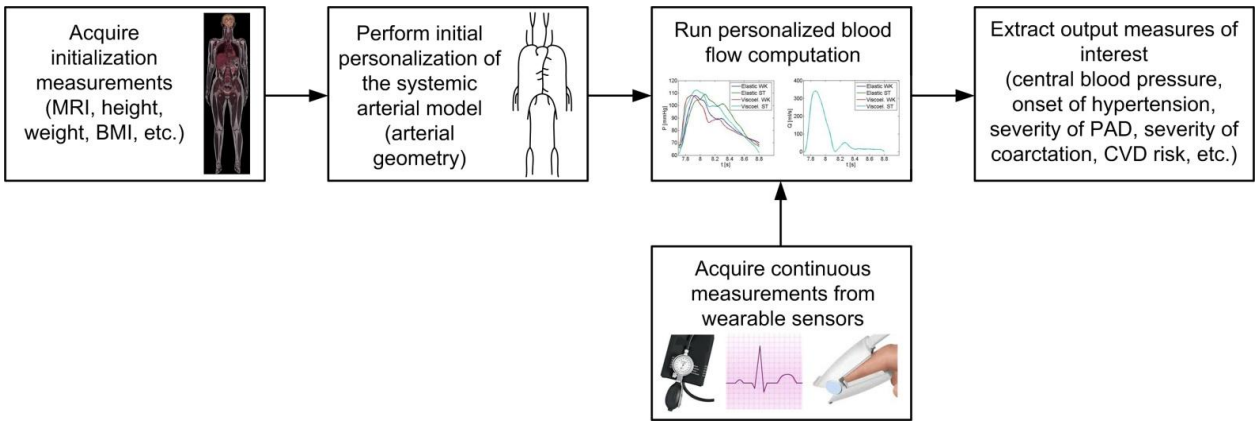

Figure 9.4: Overview of the proposed methodology.

To perform patient-specific hemodynamic computations, the blood flow model has to be personalized. The following components need to be personalized:

- arterial geometry;
- arterial wall properties;
- inlet boundary condition: time-varying flow rate profile at the aortic inlet;
- outlet boundary conditions: parameters of the windkessel models coupled at the outlet of each terminal artery .

The arterial geometry is personalized during the initial personalization step in Figure 9.4. The starting point is a population average whole-body systemic arterial model [Reymond et al., 2011]. Previously reported blood flow computation frameworks typically rely on one or two sets of patient-specific measurements which are taken in the hospital. This has several disadvantages:

- the blood flow model can only be personalized for the patient state at which the measurements were performed;
- the white coat syndrome (white coat hypertension): in a clinical setting patients typically exhibit a blood pressure level above the normal range. This is attributed to the anxiety experienced during a clinical visit.

By using the proposed methodology the blood flow model can be personalized for an almost infinite number of states: rest, lying down, sitting, upright, different levels of physical exercise, sleep, pre- and post-interventional, etc. This allows for a significantly more comprehensive evaluation of the patient's health state, than with regular blood flow computations which focus on a single patient state.

References

NEW

[Acevedo-Bolton et al., 2006] Acevedo-Bolton, G., Jou, L. D., Dispensa, B. P., Lawton, M. T., Higashida, R. T., Martin, A. J., Young, W. L., Saloner, D. "*Estimating the Hemodynamic Impact of Interventional Treatments of Aneurysms: Numerical Simulation with Experimental Validation: Technical Case Report*", Neurosurgery, Vol. 59, pp. 429–430, 2006.

[Aharinejad et al., 1998] Aharinejad, S., Schreiner, W., Neumann, F. "*Morphometry of human coronary arterial trees*", The Anatomical Record, Vol. 251, pp. 50-59, 1998.

[Alastruey et al., 2009] Alastruey, J., Nagel, S., Nier, B., Hunt, A., Weinberg, P. D., Peiro, J. "*Modelling pulse wave propagation in the rabbit systemic circulation to assess the effects of altered nitric oxide synthesis*", Journal of Biomechanics, Vol. 42, pp. 2116–2123, 2009.

[Ament et al., 2010] Ament, M., Knittel, G., Weiskopf, D., Strasser, W. "*A parallel preconditioned conjugate gradient solver for the poisson problem on a multi-GPU platform*", Proc. of the Parallel, Distributed and Network-Based Processing Conference - PDP 2010, Pisa, Italy, Fenruary 2010, pp. 583-592.

[Antiga et al., 2008] Antiga, L., Piccinelli, M., Botti, L., Ene-Iordache, B., Remuzzi, A., Steinman, D. A. "*An Image-Based Modeling Framework for Patient-Specific Computational Hemodynamics*", Medical and Biological Engineering and Computing, Vol. 46, pp. 1097–1112, 2008.

[Anzt et al., 2012] Anzt, H., Tomov, S., Gates, M., Dongarra, J., Heuveline, V. "*Block-asynchronous multigrid smoothers for GPU-accelerated systems*", Procedia Computer Science, Vol. 9, pp. 7-16, 2012.

[Atta-Alla et al., 2015] Atta-Alla, S., El Sawa, E., Atta-Alla, A., El Baassiri, E., Hassan, K.H. "*Morphometric Study of the Right Coronary Artery*", International Journal of Anatomy and Research, Vol. 3, pp. 1362-1370, 2015.

[Avolio et al., 1983] Avolio, A.P., Chen, S.G., Wang, R.P., Zhang, C.L., Li, M.F., O'Rourke, M.F. "*Effects of aging on changing arterial compliance and left ventricular load in a northern Chinese urban community*", Circulation, Vol. 68, pp. 50–58, 1983.

[Baumann et al., 2015] Baumann, S., Wang, R., Schoepf, J., Steinberg, D., Spearman, J., Bayer, R., Hamm, C., Renker, M. "*Coronary CT angiography-derived fractional flow reserve correlated with invasive fractional flow reserve measurements – initial experience with a novel physician-driven algorithm*", European Radiology, Vol. 25, pp. 1201–1207, 2015.

[Ben-Dor et al., 2011] Ben-Dor, I., Torguson, R., Gaglia, M.A. Jr, Gonzalez, M.A., Maluenda, G., Bui, A.B., Xue, Z., Satler, L.F., Suddath, W.O., Lindsay, J., Pichard, A.D., Waksman, R. "*Correlation between fractional flow reserve and intravascular ultrasound lumen area in intermediate coronary artery stenosis*", EuroIntervention, Vol. 7, pp. 225-233, 2011.

[Bensalah et al., 2013] Bensalah, M. et al "*Hemodynamic modeling of the intrarenal circulation*", Annals of Biomedical Engineering, Vol. 41, pp. 2630-2644, 2013.

[Bertoglio et al., 2012] Bertoglio, C., Moireau, P., Gerbeau, J. F. "*Sequential Parameter Estimation for Fluid–Structure Problems: Application to Hemodynamics*", Inter. Journal for Numerical Methods in Biomedical Engineering, Vol. 28, pp. 434–455, 2012.

[Bessems, 2007] Bessems, D. "*On the Propagation of Pressure and Flow Waves through the Patient-Specific Arterial System*", Ph.D. Thesis, TU Eindhoven, Netherlands, 2007.

[Bishop, 2006] Bishop, C.M. "*Pattern recognition and machine learning*", Springer, New York, USA, 2006.

[Blanco et al., 2007] Blanco, P. J., Feijoo, R. A., Urquiza, S. A. "*A Unified Variational Approach for Coupling 3D–1D Models and its Blood Flow Applications*", Computer Methods in Applied Mechanics and Engineering, Vol. 196, pp. 4391–4410, 2007.

[Blanco et al., 2012] Blanco, P. J., Watanabe, S. M., Feijo, R. A. "*Identification of Vascular Territory Resistances in One-dimensional Hemodynamics Simulations*", Journal of Biomechanics Vol. 45 pp. 2066–2073, 2012.

[Boussel et al., 2008] Boussel, L., Rayz, V., McCulloch, C., Martin, A., Acevedo-Bolton, G., Lawton, M., Higashida, R., Smith, W. S., Young, W. L., Saloner, D. "*Aneurysm Growth Occurs at Region of Low Wall Shear Stress: Patient-Specific Correlation of Hemodynamics and Growth in a Longitudinal Study*", Stroke, Vol. 39, pp. 2997–3002, 2008.

[Boussel et al., 2009] Boussel, L., Rayz, V., Martin, A., Acevedo-Bolton, G., Lawton, M. T., Higashida, R., Smith, W. S., Young, W. L., Saloner, D. "*Phase-Contrast Magnetic Resonance Imaging Measurements in Intracranial Aneurysms: In Vivo of Flow Patterns, Velocity Fields, and Wall Shear Stress: Comparison with Computational Fluid Dynamics*", Magnetic Resonance in Medicine, Vol. 61, pp. 409–417, 2009.

[Briggs et al., 2000] Briggs, W.L., McCormick, S.F. et al. "*A multigrid tutorial*", Siam, New York, USA, 2000.

[Burkhoff, 2013] Burkhoff, D. "*Pressure-Volume Loops in Clinical Research: A Contemporary View*", Journal of the American College of Cardiology, Vol. 62, pp. 1173-1176, 2013.

[Cebral et al., 2005] Cebral, J. R., Castro, M. A., Burgess, J. E., Pergolizzi, R. S., Sheridan, M. J., Putman, C. M. "*Characterization of Cerebral Aneurysms for Assessing Risk of Rupture by Using Patient-Specific Computational Hemodynamics Models*", American Journal of Neuroradiology, Vol. 26, pp. 2550–2559, 2005.

[Cebral et al., 2011] Cebral, J. R., Mut, F., Weir, J., Putman, C. M. "*Association of Hemodynamic Characteristics and Cerebral Aneurysm Rupture*", American Journal of Neuroradiology, Vol. 32, pp. 264–270, 2011.

[Choy et al., 2008] Choy, J.S., Kassab, G.S. "*Scaling of myocardial mass to flow and morphometry of coronary arteries*", Journal of Applied Physiology, Vol. 104, pp. 1281-1286, 2008.

[Chung, 2002] Chung, T. J. "*Computational Fluid Dynamics*", Cambridge University Press, Cambridge, UK, 2002.

[Coenen et al., 2015] Coenen, A., Lubbers, M.M., Kurata, A., Kono, A., Dedic, A., Chelu, R.G., Dijkshoorn, M.L., Gijsen, F.J., Ouhlous, M., van Geuns, R.J.M., Nieman, K. "*Fractional flow reserve computed from noninvasive CT angiography data: diagnostic performance of an on-site clinician-operated computational fluid dynamics algorithm*", Radiology, Vol. 274, pp. 674-683, 2015.

[Coenen et al., 2016] Coenen, A., Lubbers, M.M., Kurata, A., Kono, A., Dedic, A., Chelu, R.G., Dijkshoorn, M.L., van Geuns, R.J., Schoebinger, M., Itu, L.M., Sharma, P., Nieman, K. "*Coronary CT angiography derived fractional flow reserve: Methodology and evaluation of a point of care algorithm*", Journal of Cardiovascular Computed Tomography, Vol. 10, pp. 105-113, 2016.

[Coogan et al., 2012] Coogan, J. S., Humphrey, J. D., Figueroa, C. A. "*Computational Simulations of Hemodynamic Changes within Thoracic, Coronary, and Cerebral Arteries Following Early Wall Remodeling in Response to Distal Aortic Coarctation*", Biomechanics and Modeling in Mechanobiology, Vol. 12, pp. 79–93, 2012.

[Corban et al., 2014] Corban, M.T. et al. "*Combination of plaque burden, wall shear stress, and plaque phenotype has incremental value for prediction of coronary atherosclerotic plaque progression and vulnerability*", Atherosclerosis, Vol. 232, pp. 271-6, 2014.

[Cousins et al., 2012] Cousins, W., Gremaud, P.A. "*Boundary Conditions for Hemodynamics: The Structured Tree Revisited*", Journal of Computational Physics, Vol. 231, pp. 6086–6096, 2012.

[Cousins et al., 2013] Cousins, W., Gremaud, P.A., Tartakovsky, D.M. "*A New Physiological Boundary Condition for Hemodynamics*", SIAM Journal on Applied Mathematics, Vol. 73, pp. 1203–1223, 2013.

[Cousins et al., 2014] Cousins, W., Gremaud, P.A. "*Impedance boundary conditions for general transient hemodynamics*", International Journal of Numerical Methods in Biomedical Engineering, Vol. 30, pp. 1294–1313, 2014.

[Datta et al., 2008] Datta, K., Murphy, M., Volkov, V., Williams, S., Carter, J., Oliker, L., Patterson, D., Shalf, J., Yelick, K. "*Stencil Computation Optimization and Autotuning on State-of-the-art Multicore Architectures*", ACM/IEEE Conf. on Supercomputing – SC '08, New York, USA, March 2008, pp. 55–66.

[De Bruyne et al., 2012] De Bruyne, B., Pijls, N. H., Kalesan, B. "*Fractional Flow Reserve-Guided PCI versus Medical Therapy in Stable Coronary Disease*", The New England Journal of Medicine, Vol. 367, pp. 991–1001, 2012.

[De Geer et al., 2016] De Geer, J., Sandstedt, M., Björkholm, A., Alfredsson, J., Janzon, M., Engvall, J., Persson, A. "*Software-based on-site estimation of fractional flow reserve using standard coronary CT angiography data*", Acta Radiologica, Vol. 57, pp. 1186-1192, 2016.

[Deng et al., 2015] Deng, S.B., Jing, X.D., Wang, J., Huang, C., Xia, S., Du, J.L., Liu, Y.J., She, Q. "*Diagnostic performance of noninvasive fractional flow reserve derived from coronary computed tomography angiography in coronary artery disease: A systematic review and meta-analysis*", International Journal of Cardiology, Vol. 184, pp. 703-709, 2015.

[Feng et al., 2010] Feng, J., Khir, A. "*Determination of wave speed and wave separation in the arteries using diameter and velocity*", Journal of Biomechanics, Vol. 43, pp. 455–462, 2010.

[Feng et al., 2012] Feng, C., Shu, S. Xu, J., Zhang, C.-S. "*Numerical study of geometric multigrid methods on cpu-gpu heterogeneous computers*", arXiv preprint arXiv:1208.4247, 2012.

[Fihn et al., 2012] Fihn, S.D. et al. "*2012 ACCF/AHA/ACP/AATS/PCNA/SCAI/STS guideline for the diagnosis and management of patients with stable ischemic heart disease: a report of the American College of Cardiology Foundation/American Heart Association task force on practice guidelines, and the American College of Physicians, American Association for Thoracic Surgery, Preventive Cardiovascular Nurses Association, Society for Cardiovascular Angiography and Interventions, and Society of Thoracic Surgeons*", Journal of the American College of Cardiology, Vol. 60, pp. e44-e164, 2012.

[Florkow et al., 2016] Florkow, M., Harana, J.M., van Engelen, A., Schneider, T., Rafiq, I., De Bliek, H. et al. "*An integrated software application for non-invasive assessment of local aortic haemodynamic parameters*", Procedia Computer Science, Vol. 90, pp. 2–8, 2016.

[Formaggia et al., 1999] Formaggia, L., Nobile, F., Quarteroni, A., Veneziani, A. "*Multiscale Modeling of the Circulatory System: a Preliminary Analysis*", Computing and Visualizations in Science, Vol. 2, pp. 75–83, 1999.

[Formaggia et al., 2001] Formaggia, L., Gerbeau, G. F., Nobile F., Quarteroni, A. "*On the Coupling of 3D and 1D Navier-Stokes Equations for Flow Problems in Compliant Vessels*", Computational Methods Applied Mechanical Engeneering, Vol. 191, pp. 561–582, 2001.

[Formaggia et al., 2006] Formaggia, L., Lamponi, D., Tuveri, M., Veneziani, A.. "*Numerical Modeling of 1D Arterial Networks Coupled with a Lumped Parameters Description of the Heart*", Computer Methods in Biomechanics and Biomedical Engineering, Vol. 9, pp. 273–288, 2006.

[Formaggia et al., 2009] Formaggia, L., Quarteroni, A., Vergara, C. "*On the physical consistency between three-dimensional and one-dimensional models in haemodynamics*", Journal of Computational Physics, Vol. 244, pp. 97–112, 2013.

[Fox, 1984] Fox, G.C. "*Concurrent processing for scientific calculations*", IEEE Computer Society International Conference, Vol. 10, pp. 70-73, 1984.

[Geveler et al., 2013] Geveler, M., Ribbrock, D., Göddeke, D., Zajac, P., Turek, S. "*Towards a complete FEM-based simulation toolkit on GPUs: Unstructured grid finite element geometric multigrid solvers with strong smoothers based on sparse approximate inverses*", Computers & Fluids, Vol. 80, pp. 327-332, 2013.

[Gijsen et al., 2007] Gijsen, F. J., Wentzel, J. J., Thury, A., Lamers, B., Schuurbiers, J. C., Serruys, P. W., van der Steen, A. F. "*A New Imaging Technique to Study 3-D Plaque and Shear Stress Distribution in Human Coronary Artery Bifurcations In Vivo*", Journal of Biomechanics, Vol. 40, pp. 2349–2357, 2007.

[Gonzalo et al., 2012] Gonzalo, N., Escaned, J., Alfonso, F., Nolte, C., Rodriguez, V., Jimenez-Quevedo, P., Bañuelos, C., Fernández-Ortiz, A., Garcia, E., Hernandez-Antolin, R., Macaya, C.

"*Morphometric assessment of coronary stenosis relevance with optical coherence tomography: a comparison with fractional flow reserve and intravascular ultrasound*", Journal of the American College of Cardiology, Vol. 59, pp. 1080-1089, 2012.

[Groen et al., 2007] Groen, H. C., Gijsen, F. J., van der Lugt, A., Ferguson, M. S., Hatsukami, T. S., van der Steen, A. F., Yuan, C., Wentzel, J. J. "*Plaque Rupture in the Carotid Artery is Localized at the High Shear Stress Region: a Case Report*", Stroke, Vol. 38, pp. 2379–2381, 2007.

[Grosser et al., 2011] Grosser, T., Cohen, A., Kelly, P. H. J., Ramanujam, J., Sadayappan, P., Verdoolaege, S. "*Split tiling for GPUs: automatic parallelization using trapezoidal tiles*", Workshop on General Purpose Processor Using Graphics Processing Units, Vol. 15., pp. 24-31, 2013.

[Grosskopf et al., 2009] Grosskopf, S., Biermann, C., Deng, K., Chen, Y. "*Accurate, fast, and robust vessel contour segmentation of CTA using an adaptive self-learning edge model*", Proc. of SPIE, Vol. 7259, pp. 72594D, 2009.

[Gui et al., 2012] Gui, Y., Zhang, G. "*An improved implementation of preconditioned conjugate gradient method on GPU*", Journal of software, Vol. 7, pp. 2695-2702, 2012.

[Gulsun et al., 2015] Gulsun, M.A., Littmann, A., Slesnick, T., Jin, N., Greiser, A., Jolly, M.P. et al. "*MR Phase-Contrast Imaging with Automatic Inline Flow Quantification and Visualization*", Proceedings of ISMRM, 2015.

[Hachamovitch et al., 2008] Hachamovitch, R., Di Carli, M.F. "*Methods and Limitations of Assessing New Noninvasive Tests Part II: Outcomes-Based Validation and Reliability Assessment of Noninvasive Testing*", Circulation, Vol. 117, pp. 2793-2801, 2008.

[Hall, 2011] Hall, J. "*Guyton and Hall Textbook of Medical Physiology*", 12th Ed., Saunders Elsevier, Philadelphia, USA, 2011.

[Hansen et al., 2002] Hansen, K.J. et al. "*Prevalence of renovascular disease in the elderly: a population based study*", Journal of Vascular Surgery, Vol. 36, pp. 443-451, 2002.

[Hansson, 2005] Hansson, G.K. "*Inflammation, atherosclerosis, and coronary artery disease*", New England Journal of Medicine, Vol. 352, pp. 1685-95, 2005.

[Hassan et al., 2004] Hassan, T., Ezura, M., Timofeev, E. V., Tominaga, T., Saito, T., Takahashi, A., Takayama, K., Yoshimoto, T. "*Computational Simulation of Therapeutic Parent Artery Occlusion to Treat Giant Vertebrobasilar Aneurysm*", American Journal of Neuroradiology, Vol. 25, pp. 63–68, 2004.

[Hirsch et al., 2006] Hirsch, A.T. et al. "*ACC/AHA 2005 guidelines for the management of patients with peripheral arterial disease: executive summary*", Circulation, Vol. 113, pp. 463-654, 2006.

[Holewinski et al., 2012] Holewinski, J., Pouchet, L. N., Sadayappan, P. "*High-performance code generation for stencil computations on GPU architectures*", ACM Intern. Conf. on Supercomputing, Vol. 25, pp. 311-320, 2012.

[Huo et al., 2012] Huo, Y., Svendsen, M., Choy, J. S., Zhang, Z. D., Kassab, G. S. "*A Validated Predictive Model of Coronary Fractional Flow Reserve*", Journal of the Royal Society Interface, Vol. 9, pp. 1325–38, 2012.

[Iberall, 1967] Iberall, A. S. "*Anatomy and Steady Flow Characteristics of the Arterial System with an Introduction to its Pulsatile Characteristics*", Mathematical Biosciences, Vol. 1, pp.

375–385, 1967.

[Ibrahim et al., 2010] Ibrahim, E. S., Johnson, K., Miller, A., Shaffer, J., White, R. "*Measuring Aortic Pulse Wave Velocity using High-Field Cardiovascular Magnetic Resonance: Comparison of Techniques*", Journal of Cardiovascular Magnetic Resonance, Vol. 12, pp. 26–38, 2010.

[Ismail et al., 2012] Ismail, M., Gee, M. W., Wall, W. A. "*Hemodynamic Simulation of a Patient-Specific Aortic Coarctation Model with Adjoint-Based Calibratied Windkessel Elements*", STACOM 2012, MICCAI 2012, Nice, France.

[Ismail et al., 2013] Ismail, M., Wall, W. A., Gee, M. W. "*Adjoint-based Inverse Analysis of Windkessel Parameters for Patient-Specific Vascular Models*", Journal of Computational Physics, Vol. 244, pp. 113–130, 2013.

[Ismail et al., 2015] Ismail, M., Wall, W.A., Gee, M.W. "*Adjoint-based inverse analysis of windkessel parameters for patient-specific vascular models*", Journal of Computational Physics, Vol. 244, pp. 113–130, 2015.

[Itu et al., 2011] Itu, L. M., Suciu, C., Moldoveanu, F., Postelnicu, A., "*GPU Optimized Computation of Stencil Based Algorithms*", Proc. of the 10th RoEduNet Inter. Conf. - RoEduNet, Iaşi, Romania, June 2011, pp. 1–4.

[Itu et al., 2012] Itu, L. M., Sharma, P., Mihalef, V., Kamen, A., Suciu, C., Comaniciu, D., "*A Patient-specific Reduced-order Model for Coronary Circulation*", Proc. of the IEEE Inter. Symp. On Biomedical Imaging - ISBI, Barcelona, Spain, May 2012, pp. 832–835.

[Itu et al., 2013(a)] Itu, L. M., Sharma, P., Ralovich, K., Mihalef, V., Ionasec, R., Everett, A., Ringel, R., Kamen, A., Comaniciu, D. "*Non-Invasive Hemodynamic Assessment of Aortic Coarctation: Validation with In Vivo Measurements*", Annals of Biomedical Engineering, Vol. 41, No. 4, pp. 669–681, 2013.

[Itu et al., 2013(b)] Itu, L. M., Sharma, P., Kamen, A., D., Suciu, C., Comaniciu, D. "*Graphics Processing Unit Accelerated One-Dimensional Blood Flow Computation in the Human Arterial Tree*", International Journal on Numerical Methods in Biomedical Engineering, published through early view, doi: 10.1002/cnm.2585.

[Itu et al., 2014(a)] Itu, L.M., Suciu, C. "*A method for modeling surrounding tissue support and its global effects on arterial hemodynamics*", Proc. of the IEEE EMBS Int. Conf. On Biomedical Health Informatics – BHI 2014, Valencia, Spain, June 2014, pp. 589-592.

[Itu et al., 2014(b)] Itu, L. M., Sharma, P., Georgescu, B., Kamen, A., D., Suciu, C., Comaniciu, D. "*Model Based Non-invasive Estimation of PV Loop from Echocardiography*", Proc. of the 36th Annual Inter. Conf. of the IEEE Engineering in Medicine & Biology Society - EMBC 2014, Chicago, USA, August 26-30, 2014.

[Itu et al., 2015] Itu, L.M., Sharma, P., Kamen, A., Suciu, C., Comaniciu, D. "*A Parameter Estimation Framework for Patient-specific Hemodynamic Computations*", Journal of Computational Physics, Vol. 281, pp. 316-333, 2015.

[Itu et al., 2016] Itu, L.M. et al. "*A Machine Learning Approach for Computation of Fractional Flow Reserve from Coronary Computed Tomography*", Journal of Applied Physiology, Vol. 121, pp. 42-52, 2016.

[Itu et al., 2017] Itu, L., Sharma, P., Suciu, C., Moldoveanu, F., Comaniciu, D. "*Personalized Blood Flow Computations: A Hierarchical Parameter Estimation Framework for Tuning Boundary Conditions*", International Journal of Numerical Methods in Biomedical Engineering,

Vol. 33, pp. e02803, 2017.

[Jesperson, 2009] Jesperson, D. C. "*Acceleration of a CFD Code with a GPU*", NAS Technical Report NAS-09-003, Nov. 2009.

[Kalsho et al., 2004] Kalsho, G., Kassab, G.S. "*Bifurcation asymmetry of the porcine coronary vasculature and its implications on coronary flow heterogeneity*", American Journal of Physiology - Heart and Circulatory Physiology, Vol. 287, pp. 2493–2500, 2004.

[Kamiya et al., 1980] Kamiya, A., Togawa, T. "*Adaptive Regulation of Wall Shear Stress to Flow Change in the Canine Carotid Artery*", American Journal of Physiology, Vol. 239, pp. 14–21, 1980.

[Karamanoglu et al., 1993] Karamanoglu, M., Orourke, M.F., Avolio, A.P., Kelly, R.P. "*An analysis of the relationship between central aortic and peripheral upper limb pressure waves in man*", European Heart Journal, Vol. 14, pp. 160–167, 1993.

[Karch et al., 2000] Karch, R., Neumann, F., Neumann, M., Schreiner, W. "*Staged growth of optimized arterial model trees*", Annals of Biomedical Engineering, Vol. 28, pp. 495–511, 2000.

[Kassab et al., 1995] Kassab, G., Fung, Y. "*The Pattern of Coronary Arteriolar Bifurcations and the Uniform Shear Hypothesis*", Annals of Biomechanical Engineering, Vol. 23, pp. 13–20, 1995.

[Kassab, 2006] Kassab, G. S. "*Scaling Laws of Vascular Trees: of Form and Function*", American Journal of Physiology: Heart and Circulatory Physiology, Vol. 290, pp. 894–903, 2006.

[Kern, 2000] Kern, M.J. "*Coronary physiology revisited practical insights from the cardiac catheterization laboratory*", Circulation, Vol. 101, pp. 1344-1351, 2000.

[Keshavarz-Motamed et al., 2011] Keshavarz-Motamed, Z., Garcia, J., Pibarot, P., Larose, E., Kadem, L. "*Modeling the Impact of Concomitant Aortic Stenosis and Coarctation of the Aorta on Left Ventricular Workload*", Journal of Biomechanics, Vol. 44, pp. 2817–2825, 2011.

[Keshavarz-Motamed et al., 2015] Keshavarz-Motamed, Z., Edelman, E.R., Motamed, P.K., Garcia, J., Dahdah, N., Kadem, L. "*The role of aortic compliance in determination of coarctation severity: Lumped parameter modeling, in vitro study and clinical evaluation*", Journal of Biomechanics, Vol. 48, pp. 4229-37, 2015.

[Khan et al., 2013] Khan, A.N. "*Imaging in renal artery stenosis/renovascular hypertension*", http://emedicine.medscape.com/article/380308-overview, 2013.

[Khir et al., 2001] Khir, A., O'Brien, A., Gibbs, J., Parker, K. "*Determination of wave speed and wave separation in the arteries*", Journal of Biomechanics, Vol. 34, pp. 1145–1155, 2001.

[Kim et al., 2013] Kim, J., Peruski, B., Hunley, C. "*Influence of surrounding tissues on biomechanics of aortic wall*", International Journal of Experimental and Computational Biomechanics, Vol. 2, pp. 105-117, 2013.

[Kind et al., 2010] Kind, T., Faes, T. J., Lankhaar, J.W., Vonk-Noordegraaf, A., Verhaegen, M. "*Estimation of three- and four-element windkessel parameters using subspace model identification*", IEEE Transactions on Biomedical Engineering, Vol. 57, pp. 1531-1538, 2010.

[Kirk et al., 2010] Kirk, D., Hwu, W. M. "*Programming Massively Parallel Processors: A Hands-on Approach*", Elsevier, London, UK, 2010.

[Koo et al., 2011] Koo, B.K., Erglis, A., Doh, J.H., Daniels, D.V., Jegere, S., Kim, H.S., Dunning, A., DeFrance, T., Lansky, A., Leipsic, J., Min, J.K. "*Diagnosis of ischemia-causing*

coronary stenoses by noninvasive fractional flow reserve computed from coronary computed tomographic angiograms: results from the prospective multicenter DISCOVER-FLOW (Diagnosis of Ischemia-Causing Stenoses Obtained Via Noninvasive Fractional Flow Reserve) study", Journal of the American College of Cardiology, Vol. 58, pp. 1989-1997, 2011.

[Köstler et al., 2008] Köstler, H., Schmid, R., Rüde, U., Scheit, C. "*A parallel multigrid accelerated poisson solver for ab initio molecular dynamics applications*", Computing and Visualization in Science, Vol. 11, no. 2, pp. 115-122, 2008.

[Kruk et al., 2016] Kruk, M., Wardziak, L., Demkow, M., Pleban, W., Pregowski, J., Dzielinska, S., Witulski, M., Witkowski, A., Ruzyllo, W., Kepka, C. "*Workstation-based calculation of CTA-based FFR for intermediate stenosis*", Journal of the American College of Cardiology: Cardiovascular Imaging, Vol. 9, pp. 690-699, 2016.

[Labutin et al., 2013] Labutin I. B., Surodina, I. V. "*Algorithm for sparse approximate inverse preconditioners in the conjugate gradient method*", Reliable Computing, Vol. 19, pp. 121, 2013.

[LaDisa et al., 2011] LaDisa, J. F. J., Figueroa, C. A., Vignon-Clementel, I. E., Kim, H. J., Xiao, N., Ellwein, L. M., Chan, F. P., Feinstein, J. A., Taylor, C. A. "*Computational Simulations for Aortic Coarctation: Representative Results from a Sampling of Patients*", Journal of Biomechanical Engineering, Vol. 133, pp. 091008, 2011.

[Laurent et al., 2006] Laurent, S., Cockcroft, J., Van Bortel, L., Boutouyrie, P., Giannattasio, C., Hayoz, D. Pannier, B. Vlachopoulos, C. Wilkinson, I., Struijker-Boudier, H. "*Expert consensus document on arterial stiffness: methodological issues and clinical applications*", European Heart Journal, Vol. 27, pp. 2588–2605, 2006.

[Lawes et al., 2008] Lawes, C.M., Vander Hoorn, S., Rodgers, A. "*Global burden of bloodpressure- related disease, 2001*", Lancet, Vol. 371, pp. 1513–1518, 2008.

[Levin, 1982] Levin, D.C. "*Invasive evaluation (coronary arteriography) of the coronary artery disease patient: clinical, economic and social issues*", Circulation, Vol. 66, pp. III71-79, 1982.

[Liberson et al., 2016] Liberson, A.S., Lillie, J.S., Day, S.W., Borkholder, D.A. "*A physics based approach to the pulse wave velocity prediction in compliant arterial segments*", Journal of Biomechanics, Vol. 49, pp. 3460-3466, 2016.

[Liu et al., 2007] Liu, Y., Dang, C., Garcia, M., Gregersen, H., Kassab, G. S. "*Surrounding tissues affect the passive mechanics of the vessel wall: theory and experiment*", American Journal of Physiology - Heart and Circulatory Physiology, Vol. 293, pp. 3290-3300, 2007.

[Liu et al., 2008] Liu, Y., Zhang, W., Kassab, G. S. "*Effects of myocardial constraint on the passive mechanical behaviors of the coronary vessel wall*", American Journal of Physiology - Heart and Circulatory Physiology, Vol. 294, pp. 514-523, 2008.

[Low et al., 2012] Low, K., van Loon, R., Sazonov, I., Bevan, R. L. T., Nithiarasu, P. "*An Improved Baseline Model for a Human Arterial Network to Study the Impact of Aneurysms on Pressure-Flow Waveforms*", International Journal for Numerical Methods in Biomedical Engineering, Vol. 28, pp. 1224–46, 2012.

[Malek et al., 2015] Malek, J., Azar, A.T., Nasralli, B., Tekari, M., Kamoun, H., Tourki, R., "*Computational analysis of blood flow in the retinal arteries and veins using fundus image*", Computers & Mathematics with Applications, Vol. 69, pp. 101–116, 2015.

[Mansi et al., 2013] Mansi, T., Georgescu, B., Hussan, J., Hunter, P.J., Kamen, A., Comaniciu, D. "*Data-driven reduction of a cardiac myofilament model*", Functional Imaging and Modeling

of the Heart, Vol. 14, pp. 232-240, Springer, 2013.

[Mantero et al., 1992] Mantero, S., Pietrabissa, R., Fumero, R. "*The Coronary Bed and its Role in the Cardiovascular System: a Review and an Introductory Single-Branch Model*", Journal of Biomedical Engineering, Vol. 14, pp. 109–116, 1992.

[Marso et al., 2006] Marso, S.P., Hiatt, W.R. "*Peripheral Arterial Disease in Patients with-Diabetes*", Journal of the American College of Cardiology, Vol. 47, pp. 921-29, 2006.

[Maruyama et al., 2014] Maruyama, N., Aoki, T. "*Optimizing stencil computations for NVIDIA Kepler GPUs*", Intern. Workshop on High-Performance Stencil Computations, Vol. 2, pp. 1-7, Jan. 2014.

[Matthys et al., 2007] Matthys, K. S., Alastruey, J., Peiró, J., Khir, A. W., Segers, P., Verdonck, P. R., Parker, K. H., Sherwin, S. J. "*Pulse Wave Propagation in a Model Human Arterial Network: Assessment of 1-D Numerical Simulations Against In Vitro Measurements*", Journal of Biomechanics, Vol. 40, pp. 3476–3486, 2007.

[McDermot et al., 2000] McDermot, M.M., Criqui, M.H., Liu, K. et al. "*Lower Ankle / brachial index, as calculated by averaging the dorsalis pedis and posterior tibial arterial pressures, and association with leg functioning in peripheral arterial disease*", Journal of Vascular Surgery, Vol. 32, pp. 1164-71, 2000.

[McVeigh et al., 1991] McVeigh, G.E., Burns, D.E., Finkelstein, S.M., McDonald, K.M., Mock, J.E., Feske, W. et al. "*Reduced vascular compliance as a marker for essential hypertension*", American Journal of Hypertension, Vol. 4, pp. 245–251, 1991.

[Meijboom et al., 2008] Meijboom, W.B., Van Mieghem, C.A., van Pelt, N., Weustink, A., Pugliese, F., Mollet, N.R., Boersma, E., Regar, E., van Geuns, R.J., de Jaegere, P.J., Serruys, P.W., Krestin, G.P., de Feyter, P.J. "*Comprehensive assessment of coronary artery stenoses: computed tomography coronary angiography versus conventional coronary angiography and correlation with fractional flow reserve in patients with stable angina*", Journal of the American College of Cardiology, Vol. 52, pp. 636-643, 2008.

[Meuwissen et al., 2002] Meuwissen, M., Siebes, M., Chamuleau, S.A., van Eck-Smit, B.L., Koch, K.T., de Winter, R.J., Tijssen, J.G., Spaan, J.A., Piek, J.J. "*Hyperemic stenosis resistance index for evaluation of functional coronary lesion severity*", Circulation, Vol. 106, pp. 441-446, 2002.

[Micikevicius, 2009] Micikevicius, P. "*3D Finite difference computation on GPUs using CUDA*", Workshop on General Purpose Processing on Graphics Processing Units, Vol. 6, pp. 79-84, 2009.

[Migliavacca et al., 2006] Migliavacca, F., Balossino, R., Pennati, G., Dubini, G., Hsia, T. Y., de Leval, M. R., Bove, E. L. "*Multiscale Modelling in Biofluidynamics: Application to Reconstructive Paediatric Cardiac Surgery*", Journal of Biomechanics, Vol. 39, pp. 1010–1020, 2006.

[Milner et al., 1998] Milner, J. S., Moore, J. A., Rutt, B. K., Steinman, D. A. "*Hemodynamics of Human Carotid Artery Bifurcations: Computational Studies with Models Reconstructed from Magnetic Resonance Imaging of Normal Subjects*", Journal of Vascular Surgery, Vol. 28, pp. 143–156, 1998.

[Min et al., 2012] Min, J.K., Leipsic, J., Pencina, M.J., Berman, D.S., Koo, B.K., van Mieghem, C., Erglis, A., Lin, F.Y., Dunning, A.M., Apruzzese, P., Budoff, M.J., Cole, J.H., Jaffer, F.A., Leon, M,B., Malpeso, J., Mancini, G.B., Park, S.J., Schwartz, R.S., Shaw, L.J., Mauri, L.

"*Diagnostic accuracy of fractional flow reserve from anatomic CT angiography*", JAMA, Vol. 308, pp. 1237-1245, 2012.

[Mitchell et al., 2010] Mitchell, G.F., Hwang, S.J., Vasan, R.S., Larson, M.G., Pencina, M.J., Hamburg, N.M. et al. "*Arterial stiffness and cardiovascular events: the Framingham Heart Study*", Circulation, Vol. 121, pp. 505–511, 2010.

[Moireau et al., 2012] Moireau, P. Xiao, N. Astorino, M. Figueroa, C. A., Chapelle, D., Taylor, C. A., Gerbeau, J-F. "*External tissue support and fluid-structure simulation in blood flows*", Biomechanics and Modeling in Mechanobiology, Vol. 11, pp. 1-18, 2012.

[Morris et al., 2013] Morris, P. D., Ryan, D., Morton, A., Lycett, R., Lawford, P. V., Rodney Hose, D., Gunn, J. P. "*Virtual Fractional Flow Reserve From Coronary Angiography: Modeling the Significance of Coronary Lesions*", Journal of the American College of Cardiology: Cardiovascular Interventions, Vol. 6, pp. 149–157, 2013.

[Mounier-Vehier et al., 2004] Mounier-Vehier, C. et al. "*Changes in renal blood flow reserve after angioplasty of renal artery stenosis in hypertensive patients*", Kidney Interventions, Vol. 65, pp. 245-250, 2004.

[Murray, 1926(a)] Murray, C. D. "*The Physiological Principle of Minimum Work: I. The Vascular System and the Cost of Blood Volume*", Proc. of the National Academy of Sciences of the USA, Vol. 12, pp. 207–214, 1926.

[Mynard et al., 2012] Mynard, J. P., Davidson, M. R., Penny, D. J., Smolich, J. J. "*A Simple, Versatile Valve Model for Use in Lumped Parameter and One-Dimensional Cardiovascular Models*", International Journal for Numerical Methods in Biomedical Engineering, Vol. 28, pp. 626–641, 2012.

[Ng et al., 2011] Ng, V.G., Lansky, A.J. "*Novel QCA methodologies and angiographic scores*", International Journal of Cardiovascular Imaging, Vol. 27, pp. 157-165, 2011.

[Nita et al., 2014] Nita, C., Chen, Y., Lazar, L., Mihalef, V., Itu, L. M., Viceconti, M., Suciu, C. "*GPU Accelerated Finite Element Analysis of Trabecular Bone Tissue*", Proc. of the Virtual Physiological Human Conference, Trondheim, Norway, Sept 9-12, 2014.

[Niţă et al., 2013] Niţă, C., Itu, L. M., Suciu, C. "*GPU Accelerated Blood Flow Computation using the Lattice Boltzmann Method*", 17th IEEE High Performance Extreme Computing Conference, Waltham, MA, USA, Sept. 2013.

[Nocedal et al., 2006] Nocedal, J., Wright, S. J. "*Numerical Optimization*", Springer, New York, NY, USA, 2006.

[Nordsletten et al., 2006] Nordsletten, D.A., Blackett, S., Bentley, M.D., Ritman, E.L., Smith, N.P. "*Structural morphology of renal vasculature*", American Journal of Physiology - Heart and Circulatory Physiology, Vol. 291, pp. 296–309, 2006.

[Nørgaard et al., 2014] Nørgaard, B.L., Leipsic, J., Gaur, S., Seneviratne, S., Ko, B.S., Ito, H., Jensen, J.M., Mauri, L., De Bruyne, B., Bezerra, H., Osawa, K., Marwan, M., Naber, C., Erglis, A., Park, S.J., Christiansen, E.H., Kaltoft, A., Lassen, J.F., Bøtker, H.E., Achenbach, S. "*Diagnostic performance of noninvasive fractional flow reserve derived from coronary computed tomography angiography in suspected coronary artery disease: the NXT trial (Analysis of Coronary Blood Flow Using CT Angiography: Next Steps)*", Journal of the American College Cardiology, Vol. 63, pp. 1145-1155, 2014.

[O'Rourke et al., 1990] O'Rourke, M. "*Arterial stiffness, systolic blood pressure, and logical*

treatment of arterial hypertension", Hypertension Vol. 15, pp. 339– 347, 1990.

[Olufsen et al., 2000] Olufsen, M., Peskin, C., Kim, W. Y., Pedersen, E. "*Numerical Simulation and Experimental Validation of Blood Flow in Arteries with Structured-Tree Outflow Conditions*", Annals of Biomedical Engineering, Vol. 28, pp. 1281–1299, 2000.

[Olufsen et al., 2002] Olufsen, M. S., Nadim, A., Lipsitz, L. A. "*Dynamics of Cerebral Blood Flow Regulation Explained using a Lumped Parameter Model*", American Journal of Physiology Regulatory, Integrative and Comparative Physiology, Vol. 282, pp. 611–622, 2002.

[Olufsen et al., 2007] Olufsen, M.S., Steele, M.S., Taylor, C.A. "*Fractal network model for simulating abdominal and lower extremity blood flow during resting and exercise conditions*", Computer Methods in Biomechanics and Biomedical Engineering, Vol. 10, pp. 39–51, 2007.

[Olufsen, 1998] Olufsen, M. S. "*Modeling the Arterial System with Reference to an Anesthesia Simulator*", Ph.D. Thesis, 1998.

[Olufsen, 1999] Olufsen, M. S. "*Structured Tree Outflow Condition for Blood in the Larger Systemic Arteries*", American Journal of Physiology - Heart, Vol. 276, pp. 257–268, 1999.

[Pant et al., 2014] Pant, S., Fabrèges, B., Gerbeau, J.F., Vignon-Clementel, I.E. "*A methodological paradigm for patient-specific multi-scale CFD simulations: from clinical measurements to parameter estimates for individual analysis*", International Journal of Numerical Methods in Biomedical Engineering, Vol. 30, pp. 1614–48, 2014.

[Papafaklis et al., 2014] Papafaklis, M.I., Muramatsu, T., Ishibashi, Y., Lakkas, L.S., Nakatani, S., Bourantas, C.V., Ligthart, J., Onuma, Y., Echavarria-Pinto, M., Tsirka, G., Kotsia, A., Nikas, D.N., Mogabgab, O., van Geuns, R.J., Naka, K.K., Fotiadis, D.I., Brilakis, E.S., Garcia-Garcia, H.M., Escaned, J., Zijlstra, F., Michalis, L.K., Serruys, P.W. "*Fast virtual functional assessment of intermediate coronary lesions using routine angiographic data and blood flow simulation in humans: comparison with pressure wire-fractional flow reserve*", EuroIntervention, Vol. 10, pp. 574-583, 2014.

[Perktold et al., 1995] Perktold, K., Rappitsch, G. "*Computer Simulation of Local Blood Flow and Vessel Mechanics in a Compliant Carotid Arterybifurcation Model*", Journal of Biomechanics, Vol. 28, No. 7, pp. 845–856, 1995.

[Phillips et al., 2010] Phillips, E., Fatica, M. "*Implementing the Himeno benchmark with CUDA on GPU clusters*", IEEE Intern. Parallel & Distributed Processing Symposium, Vol. 11, pp. 1-10, 2010.

[Pijls et al., 1996] Pijls, N. H., De Bruyne, B., Peels, K. "*Measurement of Fractional Flow Reserve to Assess the Functional Severity of Coronary-Artery Stenoses*", The New England Journal of Medicine, Vol. 334, pp. 1703–1708, 1996.

[Pijls, 2007] Pijls, N.H. "*Fractional flow reserve after previous myocardial infarction*", European Heart Journal, Vol. 28, pp. 2301-2302, 2007.

[Quarteroni et al., 2001] Quarteroni, A., Ragni, S., Veneziani, A. "*Coupling Between Lumped and Distributed Models for Blood Flow Problems*", Computing and Visualizations in Science, Vol. 4, pp. 111–124, 2001.

[Qureshi et al., 2014] Qureshi, U., Vaughan, G., Sainsbury, C., Johnson, M., Peskin, C., Olufsen, M., Hill, N.A. "*Numerical simulation of blood flow and pressure drop in the pulmonary arterial and venous circulation*", Biomechanics and Modeling in Mechanobiology, Vol. 13, pp. 1137-54, 2014.

[Reed et al., 1987] Reed, D., Adams, L., Patrick, M. "*Stencils and problem partitionings: Their influence on the performance of multiple processor systems*", IEEE Transactions on Computers, Vol. 7, pp. 845-858, 1987.

[Renker et al., 2014] Renker, M., Schoepf, U.J., Wang, R., Meinel, F.G., Rier, J.D., Bayer, R.R., Möllmann, H., Hamm, C.W., Steinberg, D.H., Baumann, S. "*Comparison of diagnostic value of a novel noninvasive coronary computed tomography angiography method versus standard coronary angiography for assessing fractional flow reserve*", American Journal Cardiology, Vol. 114, pp. 1303-1308, 2014.

[Reymond et al., 2011] Reymond, P., Bohraus, Y., Perren, F., Lazeyras, F., Stergiopulos, N. "*Validation of a Patient-Specific One-Dimensional Model of the Systemic Arterial Tree*", American Journal of Physiology - Heart and Circulatory Physiology, Vol. 301, pp. 1173–1182, 2011.

[Rodrigues et al., 2008] Rodrigues, C. I., Stone, J., Hardy, D., Hwu, W. W. "*GPU Acceleration of Cutoff-Based Potential Summation*", Proc. of the ACM Inter. Conf. on Computing Frontiers, Ischia, Italy, May 2008, pp. 1–10 .

[Rossitti et al., 1992] Rossitti, S., Lofgren, J. "*Vascular dimensions of the cerebral arteries follow the principle of minimum work*", Stroke, Vol. 34, pp. 371–377, 1992.

[Ruge et al., 1987] Ruge J., Stüben, K. "*Algebraic multigrid*", Multigrid methods, Vol. 3, pp. 73-130, 1987.

[Ryan, 2002] Ryan, T.J. "*The coronary angiogram and its seminal contributions to cardiovascular medicine over five decades*", Circulation, Vol. 106, pp. 752-756, 2002.

[Sadee et al., 2005] Sadee, W., Dai, Z. "*Pharmacogenetics/genomics and personalized medicine*", Human Molecular Genetics, Vol. 14, pp. R207-R214, 2005.

[Safian et al., 2001] Safian, R.D. "*Renal artery stenosis*", New England Journal of Medicine, Vol. 344, pp. 431-442, 2001.

[Samady et al., 2011] Samady, H., Eshtehardi, P., McDaniel, M.C., Suo, J., Dhawan, S.S., Maynard, C., Timmins, L.H., Quyyumi, A.A., Giddens, D.P. "*Coronary artery wall shear stress is associated with progression and transformation of atherosclerotic plaque and arterial remodeling in patients with coronary artery disease*", Circulation Vol. 124, pp. 779-788, 2011.

[Sankaran et al., 2012] Sankaran, S., Moghadam, M. E., Kahn, A., Tseng, E., Guccione, J., Marsden, A. *Patient-Specific Multiscale Modeling of Blood Flow for Coronary Artery Bypass Graft Surgery*", Annals of Biomedical Engineering, Vol. 40, pp. 2228–2242, 2012.

[Sankaran et al., 2015] Sankaran, S. "*Impact of geometric uncertainty on hemodynamic simulations using machine learning*", Computer Methods in Applied Mechanics and Engineering, Vol. 297, pp. 167-190, 2015.

[Saouti et al., 2012] Saouti, N., Marcus, J.T., Noordegraaf, A.V., Westerhof, N. "*Aortic function quantified: the heart's essential cushion*", Journal of Applied Physiology, Vol. 113, pp. 1285-1291, 2012.

[Segers et al., 2003] Segers, P., Stergiopulos, N., Westerhof, N., Wouters, P., Kolh, P., Verdonck, P. "*Systemic and pulmonary hemodynamics assessed with a lumped-parameter heart-arterial interaction model*", Journal of Engineering Mathematics, Vol. 47, pp. 185-199, 2003.

[Selvin et al., 2004] Selvin, E., Erlinger, T. "*Prevalence of and risk factors for peripheral arterial disease in the United States, results from the National Health and Nutrition Examination*

survey 1999-2000", Circulation, Vol. 110, pp. 738-43, 2004.

[Sen et al., 2012] Sen, S., Escaned, J., Malik, I.S., Mikhail, G.W., Foale, R.A., Mila, R., Tarkin, J., Petraco, R., Broyd, C., Jabbour, R., Sethi, A., Baker, C.S., Bellamy, M., Al-Bustami, M., Hackett, D., Khan, M., Lefroy, D., Parker, K.H., Hughes, A.D., Francis, D.P., Di Mario, C., Mayet, J., Davies, J.E. "*Development and validation of a new adenosine-independent index of stenosis severity from coronary wave–intensity analysis: results of the ADVISE (Adenosine Vasodilator Independent Stenosis Evaluation) study*", Journal of the Americal College Cardiology, Vol. 59, pp. 1392-1402, 2012.

[Sharma et al., 2012] Sharma, P., Itu, L. M., Zheng, X., Kamen, A., Bernhardt, D., Suciu, C., Comaniciu, D., "*A Framework for Personalization of Coronary Flow Computations During Rest and Hyperemia*", Proc. of the 34th Annual Inter. Conf. of the IEEE Engineering in Medicine & Biology Society - EMBC, San Diego, California, USA, Aug. 2012, pp. 6665–6668.

[Shi et al., 2009] Shi, J., Cai, Y., Hou, W., Ma, L., Tan, S., Ho, P.-H., Wang, X. "*GPU friendly fast poisson solver for structured power grid network analysis*", Design Automation Conference, Vol. 13, pp. 178-183, 2009.

[Shimokawabe et al., 2011] Shimokawabe, T., Aoki, T., Takaki, T., Endo, T., Yamanaka, A., Maruyama, N., Nukada, A., Matsuoka, S. "*Peta-scale phase-field simulation for dendritic solidification on the TSUBAME 2.0 supercomputer*", Intern. Conf. for High Performance Computing, Networking, Storage and Analysis, Vol. 9, pp. 13-18, 2011.

[Shojima et al., 2004] Shojima, M., Oshima, M., Takagi, K., Torii, R., Hayakawa, M., Katada, K., Morita, A., Kirino, T. "*Magnitude and Role of Wall Shear Stress on Cerebral Aneurysm: Computational Fluid Dynamic Study of 20 Middle Cerebral Artery Aneurysms*", Stroke, Vol. 35, pp. 2500–2505, 2004.

[Shroff et al., 1985] Shroff, S. G., Janicki, J. S., Weber, K. T. "*Evidence and quantitation of left ventricular systolic resistance*", American Journal of Physiology - Heart and Circulatory Physiology, Vol. 249, pp. H358–H370, 1985.

[Slager et al., 2000] Slager, C. J., Wentzel, J. J., Schuurbiers, J. C., Oomen, J. A., Kloet, J., Krams, R., von Birgelen, C., van der Giessen, W. J., Serruys, P. W., de Feyter, P. J. "*True 3-Dimensional Reconstruction of Coronary Arteries in Patients by Fusion of Angiography and IVUS (ANGUS) and its Quantitative Validation*", Circulation, Vol. 102, pp. 511–516, 2000.

[Slager et al., 2005] Slager, C. J., Wentzel, J. J., Gijsen, F. J., Thury, A., van der Wal, A. C., Schaar, J. A., Serruys, P. W. "*The Role of Shear Stress in the Destabilization of Vulnerable Plaques and Related Therapeutic Implications*", Nature Clinical Practice Cardiovascular Medicine, Vol. 2, pp. 456–464, 2005.

[Spevack et al., 2013] Spevack, D. M., Karl, J., Yedlapati, N., Goldberg, Y., Garcia, M. J. "*Echocardiographic left ventricular end-diastolic pressure volume loop estimate predicts survival in congestive heart failure*", Journal of Cardiac Failure, Vol. 19, pp. 251-259, 2013.

[Spilker et al., 2010] Spilker, R., Taylor, C. A. "*Tuning Multidomain Hemodynamic Simulations to Match Physiological Measurements*", Annals of Biomedical Engineering, Vol. 38, pp. 2635–2648, 2010.

[Steinman et al., 2005] Steinman, D. A., Taylor, C. A. "*Flow Imaging and Computing: Large Artery Hemodynamics*", Annals of Biomedical Engineering, Vol. 33, pp. 1704–1709, 2005.

[Steinman, 2002] Steinman, D. A. "*Image-Based Computational Fluid Dynamics Modeling in Realistic Arterial Geometries*", Annals of Biomedical Engineering, Vol. 30, pp. 483–497, 2002.

[Stergiopulos et al., 1992] Stergiopulos, N., Young, D., Rogge, T. "*Computer Simulation of Arterial Flow with Applications to Arterial and Aortic Stenosis*", Journal of Biomechanics, Vol. 25, pp. 1477–1488, 1992.

[Stergiopulos et al., 1994] Stergiopulos, N., Meister, J. J., Westerhof, N. "*Simple and Accurate Way for Estimating Total and Segmental Arterial Compliance: The Pulse Pressure Method*", Annals of Biomedical Engineering, Vol. 22, pp. 392–397, 1994.

[Stergiopulos et al., 1995] Stergiopulos, N., Meister, J.J., Westerhof, N. "*Evaluation of methods for estimation of total arterial compliance*", American Journal of Physiology - Heart and Circulation Physiology, Vol. 268, pp. H1540–H1548, 1995.

[Stergiopulos et al., 1999] Stergiopulos, N., Segers, P., Westerhof, N. "*Use of pulse pressure method for estimating total arterial compliance in vivo*", American Journal of Physiology - Heart and Circulation Physiology, Vol. 276, pp. H424–H428, 1999.

[Stroia et al., 2015] Stroia, I., Itu, L., Niţă, C, Lazăr, L., Suciu, C. "*GPU Accelerated Geometric Multigrid Method: Comparison with Preconditioned Conjugate Gradient"*, Proc. of the 19th IEEE High Performance Extreme Computing Conference, Waltham, MA, USA, Sept. 15-17, 2015, pp. 1-6.

[Stürmer et al., 2008] Stürmer, M., Köstler, H., Rüde, U. "*A fast full multigrid solver for applications in image processing*", Numerical linear algebra with applications, Vol. 15, pp. 187-200, 2008.

[Subramanian et al., 2005] Subramanian, R. et al. "*Renal fractional flow reserve: a hemodynamic evaluation of moderate renal artery stenoses*", Catheterization and Cardiovascular Interventions, Vol. 64, pp. 480-486, 2005.

[Suga, 1971] Suga, H. "*Theoretical analysis of a left-ventricular pumping model based on the systolic time-varying pressure/volume ratio*", IEEE Transactions on Biomedical Engineering, Vol. 18, pp. 47–55, 1971.

[Tang et al., 2006] Tang, B. T., Cheng, C. P., Draney, M. T., Wilson, N. M., Tsao, P. S., Herfkens, R. J., Taylor, C. A. "*Abdominal Aortic Hemodynamics in Young Healthy Adults at Rest and during Lower Limb Exercise: Quantification using Image Based Computer Modeling*", American Journal of Physiology: Heart and Circulatory Physiology, Vol. 291, pp. 668–676, 2006.

[Tang et al., 2008] Tang, D., Yang, C., Mondal, S., Liu, F., Canton, G., Hatsukami, T. S., Yuan, C. *"A Negative Correlation between Human Carotid Atherosclerotic Plaque Progression and Plaque Wall Stress: In Vivo MRI-based 2d/3d FSI Models*", Journal of Biomechanics, Vol. 41, pp. 727–736, 2008.

[Taylor et al., 1996] Taylor, C. A., Hughes, T. J. R., Zarins, C. K. "*Computational Investigations in Vascular Disease*", Journal of Computational Physics, Vol. 10, pp. 224–232, 1996.

[Taylor et al., 2004] Taylor, C. A., Draney, M. T. "*Experimental and Computational Methods in Cardiovascular Fluid Mechanics*", Annual Review of Fluid Mechanics, Vol. 36, pp. 197–231, 2004.

[Taylor et al., 2013] Taylor, C.A., Fonte, T.A., Min, J.K. "*Computational fluid dynamics applied to cardiac computed tomography for noninvasive quantification of fractional flow reserve: scientific basis*", Journal of the American College of Cardiology, Vol. 61, pp. 2233-2241, 2013.

[Taylor, 1966] Taylor, M.G. "*Wave transmission through an assembly of randomly branching*

elastic tubes", Biophysical Journal, Vol. 6, pp. 697–716, 1966.

[Tøndel et al., 2011] Tøndel, K., Indahl, U.G., Gjuvsland, A.B., Vik, J.O., Hunter, P., Omholt, S.W., Martens, H. "H*ierarchical Cluster-based Partial Least Squares Regression (HC-PLSR) is an efficient tool for metamodelling of nonlinear dynamic models*", BMC Syst Biol, Vol. 5, pp. 90-106, 2011.

[Tonino et al., 2009] Tonino, P. A., De Bruyne, B., Pijls, N. H. "*Fractional Flow Reserve versus Angiography for Guiding Percutaneous Coronary Intervention*", The New England Journal of Medicine, Vol. 360, pp. 213–224, 2009.

[Toth et al., 2014] Toth, G., Hamilos, M., Pyxaras, S., Mangiacapra, F., Nelis, O., De Vroey, F., Di Serafino, L., Muller, O., Van Mieghem, C., Wyffels, E., Heyndrickx, G.R., Bartunek, J., Vanderheyden, M., Barbato, E., Wijns, W., De Bruyne, B. "*Evolving concepts of angiogram: fractional flow reserve discordances in 4000 coronary stenoses*", European Heart Journal, Vol. 35, pp. 2831-2838, 2014.

[Toutouzas et al., 2015] Toutouzas, K. et al. "*Accurate and reproducible reconstruction of coronary arteries and endothelial shear stress calculation using 3D OCT: comparative study to 3D IVUS and 3D QCA*", Atherosclerosis, Vol. 240, pp. 510-9, 2015.

[Tröbs et al., 2016] Tröbs, M. et al. "*Comparison of Fractional Flow Reserve Based on computational fluid dynamics modeling using coronary angiographic vessel morphology versus invasively measured Fractional Flow Reserve*", American Journal of Cardiology, Vol. 117, pp. 29-35, 2016.

[Trottenberg et al., 2000] Trottenberg, U., Oosterlee, C. W., Schuller, A. "*Multigrid*", Academic press, New York, USA, 2000.

[Tu et al., 2014] Tu, S., Barbato, E., Köszegi, Z., Yang, J., Sun, Z., Holm, N.R., Tar, B., Li, Y., Rusinaru, D., Wijns, W., Reiber, J.H. "*Fractional flow reserve calculation from 3-dimensional quantitative coronary angiography and TIMI frame count: a fast computer model to quantify the functional significance of moderately obstructed coronary arteries*", Journal of the American College of Cardiology: Cardiovascular Interventions, Vol. 7, pp. 768-777, 2014.

[Tu et al., 2015] Tu, S., Bourantas, C.V., Nørgaard, B.L., Kassab, G.S., Koo, B.K., Reiber, J.H. "*Image-based assessment of fractional flow reserve*", EuroIntervention, Vol. 11, pp. V50-V54, 2015.

[van Bavel et al., 1992] van Bavel, E., Spaan, J.A.E. "*Branching patterns in the porcine coronary arterial tree: estimation of flow heterogeneity*", Circulation Research, Vol. 71, pp. 1200–1212, 1992.

[van de Hoef et al., 2012] van de Hoef, T.P., Nolte, F., Damman, P., Delewi, R., Bax, M., Chamuleau, S.A., Voskuil, M., Siebes, M., Tijssen, J.G., Spaan, J.A., Piek, J.J., Meuwissen, M. "*Diagnostic accuracy of combined intracoronary pressure and flow velocity information during baseline conditions adenosine-free assessment of functional coronary lesion severity*", Circulation: Cardiovascular Interventions, Vol. 5, pp. 508-514, 2012.

[van de Vosse et al., 2011] van de Vosse, F. N., Stergiopulos, N. "*Pulse Wave Propagation in the Arterial Tree*", Annual Review of Fluid Mechanics, Vol. 43, pp. 467–499, 2011.

[van Slochteren et al., 2012] Van Slochteren, F. J., Grundeman, P. F., Teske, A. J., Bovendeerd, P. H. M. "*Left ventricular PV loop estimation using 3D echo*", Eindhoven University of Technology, Internal report BMTE 07.42, accessible at: http://www.mate.tue.nl/mate/pdfs/8738.pdf.

[Vignon-Clementel et al., 2006] Vignon-Clementel, I., Figueroa, C. A., Jansen, K. E., Taylor, C. A. "*Outflow Boundary Conditions for Three-Dimensional Finite Element Modeling of Blood Flow and Pressure in Arteries*", Comput. Methods Applied Mechanical Engineering, Vol. 195, pp. 3776–3796, 2006.

[Vignon-Clementel et al., 2010] Vignon-Clementel, I., Figueroa, C. A., Jansen, K. E., Taylor, C. A. "*Outflow Boundary Conditions for 3D Simulations of Non-periodic Blood Flow and Pressure Fields in Deformable Arteries*", Computer Methods in Biomechanics and Biomedical Engineering, Vol. 13, No. 5, pp. 1–16, 2010.

[Vizitiu et al., 2014] Vizitiu, A., Itu, L. M., Nita, C., Suciu, C. "*Optimized Three-Dimensional Stencil Computation on Fermi and Kepler GPUs*", 18th IEEE High Performance Extreme Computing Conference, Waltham, MA, USA, Sept 2014.

[Wang et al., 1999] Wang, K. C., Dutton, R. W., Taylor, C. A. "*Improving Geometric Model Construction for Blood Flow Modeling*", Journal of Medical and Biological Engineering, Vol. 18, pp. 33–39, 1999.

[Wang et al., 2015] Wang, R., Renker, M., Schoepf, U.J., Wichmann, J.L., Fuller, S.R., Rier, J.D., Bayer, R.R., Steinberg, D.H., De Cecco, C.N., Baumann, S. "*Diagnostic value of quantitative stenosis predictors with coronary CT angiography compared to invasive fractional flow reserve*", European Journal of Radiology, Vol. 84, pp. 1509-1515, 2015.

[Weitz et al., 1996] Weitz, J.I., Byrne, J., Clagett, G.P. et al. "*Diagnosis and treatment of chronic arterial insufficiency of the lower extremities: A critical review*", Circulation, Vol. 94, pp. 3026-49, 1996.

[Wendt, 2009] Wendt, J. F. "*Computational Fluid Dynamics: An Introduction*", 3rd Ed., Springer, Berlin, Germania, 2009.

[Westerhof et al., 2009] Westerhof, N., Lankhaar, J. W., Westerhof, B. E. "*The Arterial Windkessel*", Journal of Medical and Biological Engineering and Computing, Vol. 47, pp. 131–141, 2009.

[Willemet et al., 2013] Willemet, M., Lacroix, V., Marchandise, E. "*Validation of a 1D patient-specific model of the arterial hemodynamics in bypassed lower-limbs: Simulations against in vivo measurements*", Medical Engineering & Physics. Vol. 35, pp. 1573–1583, 2013.

[Williams et al., 2012] Williams, S., Kalamkar, D. D., Singh, A., Deshpande, A. M., Van Straalen, B., Smelyanskiy, M., Almgren, A., Dubey, P., Shalf, J., Oliker, L. "O*ptimization of geometric multigrid for emerging multi-and manycore processors*", Proc. of the International Conference on High Performance Computing, Networking, Storage and Analysis, Vol. 11, pp. 96, 2012.

[Wilson et al., 1990] Wilson, R. F., Wyche, K., Christensen, B. V., Zimmer, S., Laxson, D. D. "*Effects of Adenosine on Human Coronary Arterial Circulation*", Circulation, Vol. 82, pp. 1595–1606, 1990.

[Wilson et al., 2005] Wilson, N. M., Arko, F. R., Taylor, C. A. "*Predicting Changes in Blood Flow in Patient-Specific Operative Plans for Treating Aorto-Iliac Occlusive Disease*", Computer Aided Surgery, Vol. 10, pp. 257–277, 2005.

[Windecker et al., 2014] Windecker, S., Kolh, P., Alfonso, F., Collet, J.P., Cremer, J., Falk, V., Filippatos, G., Hamm, C., Head, S.J., Jüni, P., Kappetein, A.P., Kastrati, A., Knuuti, J., Landmesser, U., Laufer, G., Neumann, F.J., Richter, D.J., Schauerte, P., Uva, M.S., Stefanini, G.G., Taggart, D.P., Torracca, L., Valgimigli, M., Wijns, W., Witkowski. "*2014 ESC/EACTS*

Guidelines on myocardial revascularization", European Heart Journal, Vol. 46, pp. 517-592, 2014.

[Womersley, 1955(a)] Womersley, J. R. "*Method for the Calculation of Velocity, Rate of Flow and Viscous Drag in Arteries when the Pressure Gradient is Known*", The Journal of Physiology, Vol. 127, pp. 553–563, 1955.

[Xu, 2010] Xu, J. "*Fast poisson-based solvers for linear and nonlinear PDEs*", Proc. of the International Congress of Mathematics, Vol. 4, pp. 2886-2912, 2010.

[Zamir et al., 1992] Zamir, M., Sinclair, P., Wonnacott, T. H. "*Relation Between Diameter and Flow in Major Branches of the Arch of the Aorta*", Journal of Biomechanics, Vol. 25, pp. 1303–1310, 1992.

[Zarins et al., 1987] Zarins, C. K., Zatina M. A., Giddens D. P., Ku D. N., Glagov S. "*Shear Stress Regulation of Artery Lumen Diameter in Experimental Atherogenesis*", Journal of Vascular Surgery, Vol. 5, pp. 413–20, 1987.

[Zaspel et al., 2012] Zaspel, P., Griebel, M. "*Solving Incompressible Two-Phase Flows on Multi-GPU Clusters*", Computers & Fluids, 2012, published online.

[Zhang et al., 2014] Zhang, W. et al. "*Hemodynamic analysis of renal artery stenosis using computational fluid dynamics technology based on unenhanced steady-state free precession magnetic resonance angiography: preliminary results*", International Journal of Cardiovascular Imaging, Vol. 30, pp. 367-375, 2014.

[Zheng et al., 2008] Zheng, Y., Barbu, A., Georgescu, B., Scheuering, M., Comaniciu, D. "*Four-chamber heart modeling and automatic segmentation for 3-D cardiac CT volumes using marginal space learning and steerable features*", IEEE Transactions on Medical Imaging, Vol. 27, pp. 1668-1681, 2008.

[Zheng et al., 2014] Zheng, Y., Comaniciu, D. "*Marginal Space Learning for Medical Image Analysis*", Springer, New York, USA, 2014.

[Zhou et al., 1999] Zhou, Y., Kassab, G.S., Molloi, S. "*On the design of the coronary arterial tree: a generalization of Murray's law*", Physics in Medicine and Biology, Vol. 44, pp. 2929, 1999.

[Zou et al., 2009] Zou, C., Xia, C., Zhao, G. "*Numerical parallel processing based on GPU with cuda architecture*", in Wireless Networks and Information Systems, 2009. WNIS'09. International Conference on, pp. 93-96, 2009.

[Zumbusch, 2013] Zumbusch, G. "*Vectorized higher order finite difference kernels*", Lecture Notes in Computer Science, Vol. 7782, pp. 343-357, 2013.

[***CardioProof, 2017] Cardioproof: http://www.cardioproof.eu/, accessed 2017.

[***CFD Challenge, 2013] ***, CFD challenge: predicting patient-specific hemodynamics at rest and stress through an aortic coarctation, http://www.vascularmodel.org/miccai2013/, accessed 06/10/2014.

[***FDA, 2013] FDA, Paving the Way for Personalized Medicine - FDA's Role in a New Era of Medical Product Development, 2013.

[***NRC, 2011] National Research Council: Committee on a Framework for Developing a New Taxonomy of Disease. (2011). Toward Precision Medicine: Building a Knowledge Network for Biomedical Research and a New Taxonomy of Disease. Washington, DC: The National Academies Press.

[***NVIDIA, 2013] *** "*CUDA, Compute Unified Device Architecture Programming Guide v5.5*", NVIDIA Corporation, 2013.

[***vmtk, 2014] *** "The Vascular Modeling Toolkit", 2014. [Online]. Available: http://www.vmtk.org

[***WHO, 2009] World Health Organization. Global health risks. WHO Library Cataloguing-in-Publication Data: 2009.

[***WHO, 2015] World Health Organization. Global status report on noncommunicable disease 2010. WHO, 2011. Geneva: World Health Organization, 2015.